GRAPHENE NANOSHEETS PRODUCED VIA CONTROLLED DETONATION OF HYDROCARBONS

by

ARJUN NEPAL

M.S., University of Minnesota Duluth, 2011

AN ABSTRACT OF A DISSERTATION

submitted in partial fulfillment of the requirements for the degree

DOCTOR OF PHILOSOPHY

Department of Physics
College of Arts and Sciences

KANSAS STATE UNIVERSITY
Manhattan, Kansas

2015

Abstract

We demonstrated that gram quantities of pristine graphene nanosheets (GNs) can be produced via detonation of a hydrocarbon. This one-step and catalyst-free method is eco-friendly and economical for the production of GNs. The hydrocarbons detonated were C_2H_2, C_2H_4, C_3H_8 and CH_4 in the presence of O_2. The carbon products obtained from the detonation were analyzed by XRD, TEM, XPS and Raman spectroscopy. Depending upon the ratio of O_2 to C_2H_2, the GNs of size up to ~ 250 nm, SSA up to ~ 200 m^2/g and yield up to 70% with 2-3 layers' stack have been obtained so far. N_2O was determined as a good alternative to O_2 as an oxidizer to produce GNs by detonating C_2H_2 with it.

A two-color pyrometer was designed and calibrated to measure the temperature of the detonation of hydrocarbons. The measured detonation temperatures were in between 2700 K and 4300 K. Along with the high detonation temperature, the composition of precursor hydrocarbon was observed to be crucial as well to determine its suitability to detonate with oxidizer to produce GNs. The hydrocarbons C_2H_2 and C_2H_4 were determined as the suitable precursors to produce GNs whereas detonation of C_3H_8 yields mere amorphous carbon soot and CH_4 gives no solid carbon while detonated with O_2. It has been proposed that the hydrocarbons with $C/H \geq 0.5$ are suitable for GNs production by detonation method.

Highly oxidized graphene nanosheets (OGNs) were produced by solution-based oxidation of GNs prepared via a controlled detonation of acetylene at $O_2/C_2H_2=0.8$. The produced OGNs were about 250 nm in size and hydrophilic in nature. The C/O ratio was dramatically reduced from 49:1 in the pristine GNs to about 1:1 in OGNs, as determined by X-ray photoelectron spectroscopy. This C/O in OGNs is the least ever found in all oxidized graphitic materials that have been reported. Thus, the OGNs produced from the detonated GNs with such high degree of oxidation herein yields a novel and promising material for future applications.

GRAPHENE NANOSHEETS PRODUCED VIA CONTROLLED DETONATION OF HYDROCARBONS

by

ARJUN NEPAL

M. S., University of Minnesota Duluth, 2011

A DISSERTATION

submitted in partial fulfillment of the requirements for the degree

DOCTOR OF PHILOSOPHY

Department of Physics
College of Arts and Sciences

KANSAS STATE UNIVERSITY
Manhattan, Kansas

2015

Approved by:

Major Professor
Dr. Christopher M. Sorensen

Copyright

Abstract

We demonstrated that gram quantities of pristine graphene nanosheets (GNs) can be produced via detonation of a hydrocarbon. This one-step and catalyst-free method is eco-friendly and economical for the production of GNs. The hydrocarbons detonated were C_2H_2, C_2H_4, C_3H_8 and CH_4 in the presence of O_2. The carbon products obtained from the detonation were analyzed by XRD, TEM, XPS and Raman spectroscopy. Depending upon the ratio of O_2 to C_2H_2, the GNs of size up to ~ 250 nm, SSA up to ~ 200 m^2/g and yield up to 70% with 2-3 layers' stack have been obtained so far. N_2O was determined as a good alternative to O_2 as an oxidizer to produce GNs by detonating C_2H_2 with it.

A two-color pyrometer was designed and calibrated to measure the temperature of the detonation of hydrocarbons. The measured detonation temperatures were in between 2700 K and 4300 K. Along with the high detonation temperature, the composition of precursor hydrocarbon was observed to be crucial as well to determine its suitability to detonate with oxidizer to produce GNs. The hydrocarbons C_2H_2 and C_2H_4 were determined as the suitable precursors to produce GNs whereas detonation of C_3H_8 yields mere amorphous carbon soot and CH_4 gives no solid carbon while detonated with O_2. It has been proposed that the hydrocarbons with $C/H \geq 0.5$ are suitable for GNs production by detonation method.

Highly oxidized graphene nanosheets (OGNs) were produced by solution-based oxidation of GNs prepared via a controlled detonation of acetylene at $O_2/C_2H_2=0.8$. The produced OGNs were about 250 nm in size and hydrophilic in nature. The C/O ratio was dramatically reduced from 49:1 in the pristine GNs to about 1:1 in OGNs, as determined by X-ray photoelectron spectroscopy. This C/O in OGNs is the least ever found in all oxidized graphitic materials that have been reported. Thus, the OGNs produced from the detonated GNs with such high degree of oxidation herein yields a novel and promising material for future applications.

Table of Contents

List of Figures

List of Tables

Acknowledgements

First of all, I would like to thank my research advisor Professor Christopher M. Sorensen for his guidance, encouragement and supervision during my time in Ph.D. program. His continuous guidance on experimental methods and evaluation of results and analysis I produced has helped me develop the skills of an independent researcher. My sincere gratitude to him for introducing me with many collaborators while working in an interdisciplinary environment required by my research. The training and experience I gained from him will certainly help me be self-guided in my future research career.

I want to thank Dr. Bret N. Flanders for being in my dissertation committee and for letting me use Raman Spectrometer in his lab throughout my Ph.D. career. Most of the interactions, on the measurements and data of my samples, with Dr. Flanders were fruitful. Also, I want to thank Dr. G. Paneru and Dr. P. Thapa, previous group members of Dr. Flanders group, for helpful discussions.

I would like to thank Dr. Amit Chakrabarti, Dr. Jun Li and Dr. Mohammad H. Hosni for being in my dissertation committee. In addition, the suggestions and help provided by Dr. Li in work related to oxidization of graphene nanosheets were valuable.

I thank Prof. K. J. Klabunde for use of his XRD and BET instruments and also thanks to Dr. Daniel L. Boyle for TEM and Dr. David Moore, KU for HRTEM measurement. Thanks to Dr. Leila Maurmann, and Dr. Xiuzhi Sun for helping us to obtain FTIR, and TGA data, respectively. The help I received from Russ Reynolds (Physics Machine Shop), Tim Sobering and his group (Electronic Design Lab) and Peter Nelson were really instrumental to set up tools in my detonation lab at High Bay. Thank you all. I also want to thank all other collaborators, Dr. G. Chiu, J. Xie, Dr. G. P. Singh, N. Ploscariu, S. Klankowski, T. Sung and Dr. K. L. Hohn, for their help and input on the work related to oxidized graphene nanosheets. The help I got from Dr. K. Hohn and J. Xie with XPS of some of my samples and from Dr. Chiu while carrying out the related experiment were really great. My additional thanks goes to Dr. G. P. Singh for helping me with valuable interactions, corrections and comments to most of my research and papers. I am thankful to all other members of Dr. Sorensen's group. Additional thanks to Jessica who actually demonstrated the detonation experiments for me when I joined the group in 2010. I am equally thankful to all members of Condensed Matter Physics at KSU who put their valuable comments and questions on my research presentation during seminars.

I would like to thank department of Physics for providing me with the teaching assistantships to support me financially during most of the time of my Ph.D. Also, I would like to thank to KSU Targeted Excellence and NSF EPSCOR : IIA-1430493 for funding me and my research partially.

A big and special thanks goes to my wife, Kabita, for continued inspiration and support for my studies. My kids, Sama and Samaya, were always nice with Kabita while I was at work. Thanks to both of you. At last, I want to recall and respect the love, support, and wish of my parents for a timely completion of my Ph.D. Thank you both for everything you did for me so far.

Dedication

To my all teachers and family.

Chapter 1 - Introduction

1.1 Overview

Graphene is a one atom thick sheet of carbon atoms packed in honeycomb crystal lattice. After the successful isolation of single layer graphene from graphite in 2004 [1], the interest on graphene research among the various scientific disciplines has been increased to explore its properties and applications. The electrical, thermal, optical and mechanical properties of graphene are so excellent that it has been considered a "wonder material" with promise of numerous potential applications. Several methods of graphene synthesis have been invented as attempts to fulfill its demand for scientific studies and applications. The first purpose of this dissertation is to present a new route of graphene production: controlled detonation of gas-phase hydrocarbons. This method of production of graphene nanosheets (GNs) is single-step, eco-friendly, scalable, and high yielding. Secondly, the theory and calibration of a two-color pyrometer that was made and used to measure the temperature of detonation will be explained. Finally, the highly oxidized graphene nanosheets (OGNs) obtained from the oxidization of detonation produced GNs will be presented.

In this chapter, a brief description of history, properties, applications and methods of synthesis of graphene is presented. The components of the chamber used for detonation will be introduced along with a brief description of the earlier work done with this chamber. All the detonations to prepare the GNs mentioned here were carried out in a 16.6 liter aluminum chamber.

1.2 Carbon nanostructures and graphene

Zero-dimensional (0D) fullerenes, one-dimensional (1D) carbon nanotubes and two-dimensional (2D) graphene are the carbon nanostructures discovered within past 30 years. 2D graphene is considered as a basic building block for graphitic materials of all other dimensionalities (Fig. 1.1). It can be wrapped up into 0D fullerenes, rolled into 1D nanotubes or stacked into 3D graphite [2]. After the discovery of fullerenes in 1985 [3] and carbon nanotubes in 1991 [4], the extensive experimental and theoretical investigations on carbon nanostructures have began in nanoscience and nanotechnology. The existence of 2D graphene was thought to be impossible before its discovery because the earlier theories and experiments had shown that a free-standing 2D materials were thermodynamically unstable [5–7]. This was thought because the melting temperature of thin films decreases with decreasing thickness and the decomposition or segregation of films into islands was observed at thicknesses of dozens of atomic layers [2,7]. Hence, a free-standing 2D graphene sheet was theorized to be unstable relative to the formation of curved carbon structures like soot, nanotubes and fullerenes [1,2]. However, the concept of non-existence of 2D graphene was rebutted when it was demonstrated for the first time, by peeling off the layers of graphite by scotch tape, in 2004 [1]. The work received accolades from the scientific community involved in carbon research and two members, Andre Geim and Konstantin Novoselov, from the group were honored by the Nobel Prize in Physics of 2010 for their discovery. This pioneering work on graphene actually created a sense of accomplishment among those who had interest in carbon nanostructure and motivated a large number of researchers to jump into it bringing a growth in the field. The U.S. patents and patent applications related to carbon nanostructures have reached a total of about 45,000 [8] and there were over 14,000 scientific publications published last year with the keyword ‘graphene’(Web of Knowledge 2014). These numbers reflect that a large number of people are involved in the study of properties, applications and synthesis of graphene at present.

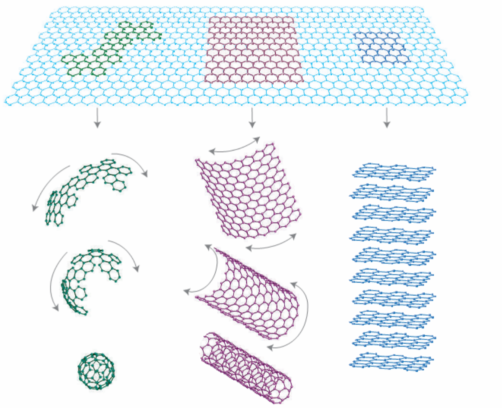

Figure 1.1 Graphene (top) and related structures: multilayer graphite (bottom right), nanotube (bottom center), fullerene (bottom left). Reprinted with the permission of reference [2]. Copyright 2007 Nature Publishing Group.

1.3 Properties of Graphene

Graphene possesses such unique electronic properties that most of the current interest in graphene lies in understanding and utilizing these properties. At room temperature, the electrons travelling through graphene can traverse sub-micrometer distances without being scattered

[2,9,10]. Electrons travelling through graphene loose their effective rest mass and hence mimic the relativistic particles moving through space with speed near to the speed of light [2,9–11]. Consequently, the mobility of the charge carriers in graphene have been observed to be about $2x10^5$ cm^2 V^{-1} s^{-1} which is higher than 1500 cm^2 V^{-1} s^{-1} for Si and 8500 cm^2 V^{-1} s^{-1} for GaAs [10]. Moreover, graphene has charge carrier density of about 10^{13} cm^2 [2,12].

Graphene possesses superior mechanical and thermal properties. A Young's modulus of 1TPa, a third-order elastic stiffness of-2 TPa, and an intrinsic strength of 130 GPa were measured for defect-free graphene and these values are the evidences for graphene as the strongest material ever measured [13]. Also, despite being an atom thick ever known thinnest material, it is impermeable to gases including helium [14]. The room temperature thermal conductivity of graphene, 5300 W m^{-1} K^{-1}, is more than that of single-walled carbon nanotube (3500 $Wm^{-1}K^{-1}$) and diamond (2000 $Wm^{-1}K^{-1}$) [15]. Graphene has also an extremely high surface area with theoretical value of 2630 m^2/g and it is almost transparent, absorbing only 2.3% to white light [16]. Graphene recovers the electronic properties during its bending and unbending and hence has a good 'foldability' [17].

1.4 Potential applications of Graphene

The excellent electronic properties possessed by graphene have led it to be proposed as the material capable of replacing Si in integrated circuits [2]. Graphene is a promising substitute for the costly semiconductors like GaAs and InP that have been used in ultra-high frequency transistors [2,9]. Flexible, bendable and transparent electronic devices have been developed by using graphene sheets [17]. The other applications of graphene in nanoelectronics [18,19], sensors [20], nanocomposites [21,22], batteries [23], supercapacitors and hydrogen storage [2] have been reviewed and discussed in detail elsewhere. The list of the potential applications of graphene is expected to grow more as researchers discover new remarkable properties of this wonder material. In order to explore the properties and potential applications, methods of synthesis of good quality graphene need to be developed. Although this has been a significant challenge, a number of different routes to synthesize graphene have been demonstrated over recent years, as discussed in the following section.

1.5 Methods of Synthesis of Graphene

Methods of synthesis of graphene invented so far are broadly divided into two types: top-down and bottom-up (Fig. 1.2). In top-down methods, the stacked layers in graphite are separated apart. The method designed should be capable of overcoming van der Waals forces between the layers and a relatively weak interlayer bonding energy. The main challenges in this method are: separating the layers without their damage and preventing their re-agglomeration after their separation. Low yield and painstaking multiple steps involved are the main disadvantages of these methods [24].

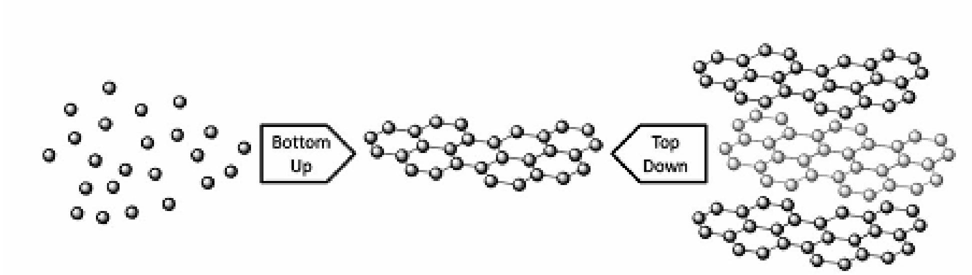

Figure 1.2 Schematic of bottom-up and top-down method of synthesis of graphene. Reprinted with the permission of reference [24]. **Copyright 2012 The Royal Society of Chemistry.**

In bottom-up methods, graphene is synthesized by graphitizing a carbonaceous precursor at high temperature. The graphene produced by this method have more defects than those produced by top-down methods. Below is a quick review of some of the common methods of synthesis of graphene.

1.5.1 Top-Down Methods

Micromechanical Cleavage: A graphite crystal can be exfoliated mechanically to cleave the layers apart. This had been shown by exfoliating highly oriented pyrolytic graphite (HOPG) by a transparent tape in 1990 [25] and later, in 1999, Ruoff's group exfoliated the HOPG by using oxygen plasma etching of lithographically patterned surface [26]. However, both of those works were able to show thin platelets of graphite with several layers and could not demonstrate single layer graphene.

In the first successful demonstration of monolayer graphene [1], as illustrated in Fig. 1.3, a graphite flake kept on a piece of scotch tape (Fig. 1.3a), was cleaved repeatedly by folding and peeling off the tape at the region of edge of the flake on it and the thin flakes attached on the tape (Fig. 1.3b) were transferred onto SiO_2 (285 nm thick) coated Si substrate. Images from an optical microscope of the substrate then showed thick, thin (Fig. 1.3c), few layer and single layer graphene (Fig. 1.3d). The change in the refractive index between SiO_2 and graphene actually facilitated to make the graphene layers visible. Despite the low output of single layer graphene from the "scotch tape" method, the high quality of graphene required for the study of its fundamental properties is still prepared via this method. Also, the method is easy and cheap.

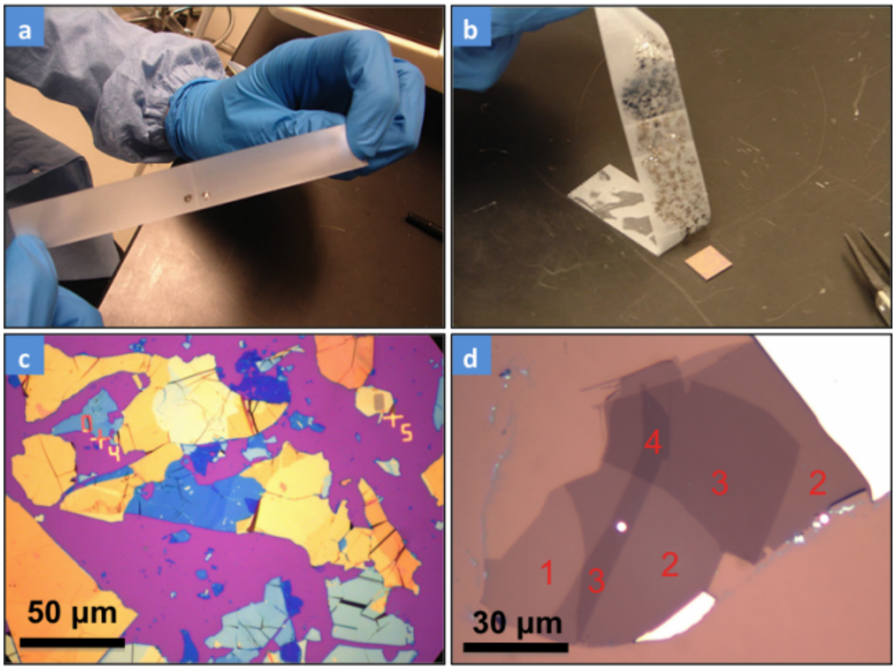

Figure 1.3 (a) Graphite flake cleaved by the scotch tape (b) Tape with many graphite thin flakes, flakes ready to be transformed on to SiO2/Si substrate (c) typical optical image of the thick (gold), thin (blue) flakes transformed on the substrate (pink) and (d) a very nice optical image of flake with identifiable one, two, three and four layers of graphene. Reprinted with the permission of reference [27]. Copyright 2011 Arend van der Zande.

Chemical Exfoliation of Graphite: This method begins with oxidation of graphite by concentrated acids and strong oxidants to prepare graphite oxide. Graphite oxide will then be exfoliated into graphene oxide (GO) and finally GO will be reduced to graphene. Hummers method [28], Brodie method [29] and improved Hummers methods [30,31] have been used widely to oxidize graphite. Graphite oxide, according to the Lerf–Klinowski model [32,33], has a layered structure with hydroxyl and epoxy groups on the basal planes and carboxylic and carbonyl groups at the sheet edges. These oxygen functional groups attached to layers of the graphite oxide make it hydrophilic and thus water molecules can be intercalated into the space between the layers. Graphite oxide can then be easily exfoliated into GO by thermal treatments or sonication in water [34]. Once individual sheets are obtained, they are subjected to chemical or thermal reduction to get reduced graphene oxide (rGO). The method has been suitable to produce a large-scale graphene. However, since the oxygen functional groups cannot be removed completely by reduction process, defects and disorder are present on the sheets. Hence, graphene produced by chemical exfoliation of graphite does not possess quality and properties as good as that of graphene produced via mechanical exfoliation.

Intercalation-aided exfoliation of graphite: Graphite is composed of graphene layers bonded with van der Waals forces, the binding force is, qualitatively, inversely proportional to the distance between graphene layers. Thus, expanding the interlayer distance can reduce their binding energy significantly and is expected to facilitate the exfoliation of graphene layer. The alkali metal graphite intercalated compounds (GIC) can be exfoliated into solvents like water and ethanol by sonication [35]. In such kind of solvent-assisted exfoliation of GIC, the intercalated solvent brings an expansion in the interlayer spacing. Also, the gases that may expel by the interaction of solvent with GIC will push the layers and hence further aid the exfoliation [36]. Thermal expansion of GIC is another way to exfoliate GIC. Heating GIC causes the thermal decomposition of material intercalated into gaseous products and that push the layers apart. Most popular example of such "expanded graphite" is prepared by the exposure of graphite into strong sulfuric acid to make graphite bisulfate which is then exfoliated by rapid heating or microwave radiation [37]. The graphene sheets produced via this method cannot exhibit the intrinsic properties as good as properties of mechanically exfoliated graphene due to the defects present in the form of oxides or hydroxides groups attached on them.

Electrochemical exfoliation: In a typical electrochemical exfoliation method, a graphite rod, sulfuric acid (H_2SO_4) and a platinum rod are used as working electrodes, electrolyte and counter-electrode, respectively (Fig. 1.4). When a positive voltage is applied to the graphite electrode, intercalation of $(SO_4)^{--}$ radicals into the defects and grain boundaries of the graphite takes place, and it starts to expand. This facilitates graphitic films dissociate from the graphite rod and spread into the electrolyte. The films in the electrolyte are vacuum filtered and washed several times with DI water to get rid of residual acid. The powder of the electrochemically exfoliated graphitic flakes is further dispersed into DMF or NMP for stable dispersions of graphene.

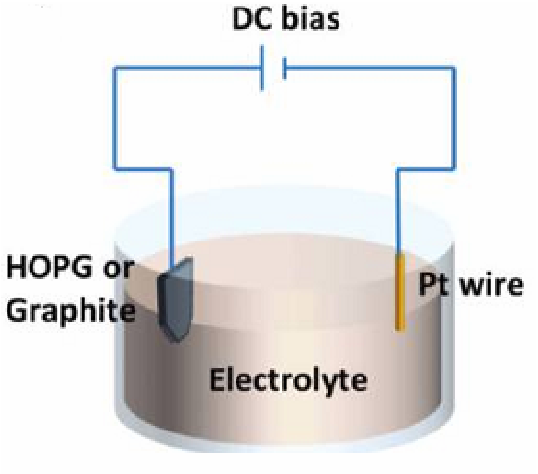

Figure 1.4 Schematic illustration of electrochemical exfoliation of graphite. Reprinted with the permission of reference [38]. Copyright 2011 American Chemical Society.

This method of graphene production has been improved by using (i) surfactant as an electrolyte to overcome the possible agglomeration of graphene sheets [39] and (ii) H_2SO_4-KOH solutions to minimize the high level of oxidation observed while H_2SO_4 alone was used as electrolyte [40]. About 80% of few layer (<5) graphene have been reported recently by sonication of lithium salt intercalated graphite electrode used in electrochemical exfoliation [41,42]. This method is scalable and the quality of graphene produced is better than the quality of those produced via chemical exfoliation but do not meet the standard quality of the graphene produced via mechanical exfoliation.

The other top down methods of graphene production include solvent-based exfoliation of graphite [43,44], discharging the electric arc between two high purity graphite electrodes [45,46,47] , unzipping carbon nanotubes [48–50], etc.

1.5.2 Bottom-Up Methods

Epitaxial growth of graphene on silicon carbide: When silicon carbide (SiC) is heated to the temperatures between 1000°C and 1500°C in ultra-high vacuum (UHV), Si starts to sublimate from the material leaving a carbon-rich surface. A low-energy electron microscopy

(LEEM) study shows the carbon layer formed is graphitic in nature and this observation has suggested that the technique is useful for the synthesis of graphene [51]. Graphene films consisting of three layers were produced by thermal decomposition on 6H- SiC heating to 1250-1450°C in UHV [52]. Graphene with smooth and much larger continuous layers, up to 50 micron in length, was produced by heating SiC in 900 mbar argon environment [53]. Millimeter size few to single-layer graphene was produced by Juang et al. by using a Ni coated SiC [54]. SiC with 200 nm thick coating of Ni on it was heated to 750°C in vacuum and a continuous layer of graphene was segregated on the entire Ni surface while cooled. Epitaxially grown graphene layers on the SiC substrate can also be transferred to an insulator substrate for the study of its application and property [55]. The graphene produced on SiC, an important electronic materials itself, possesses excellent extraordinary electronic properties that offer the possibility of greatly enhanced speed and performance relative to silicon. However, the requirements of high temperature source and maintaining the high vacuum system have been the challenges associated with this method.

Chemical vapor deposition (CVD): In a typical CVD process, solid materials such as particles, thin films, nanotubes or nanowires are deposited on a substrate by the generation of reactive species in the gaseous phase (Fig. 1.5). Reactive species are produced when precursor gases come in contact or pass over the heated substrate. CVD of carbon containing gases have been widely used to grow graphene on metal surfaces.

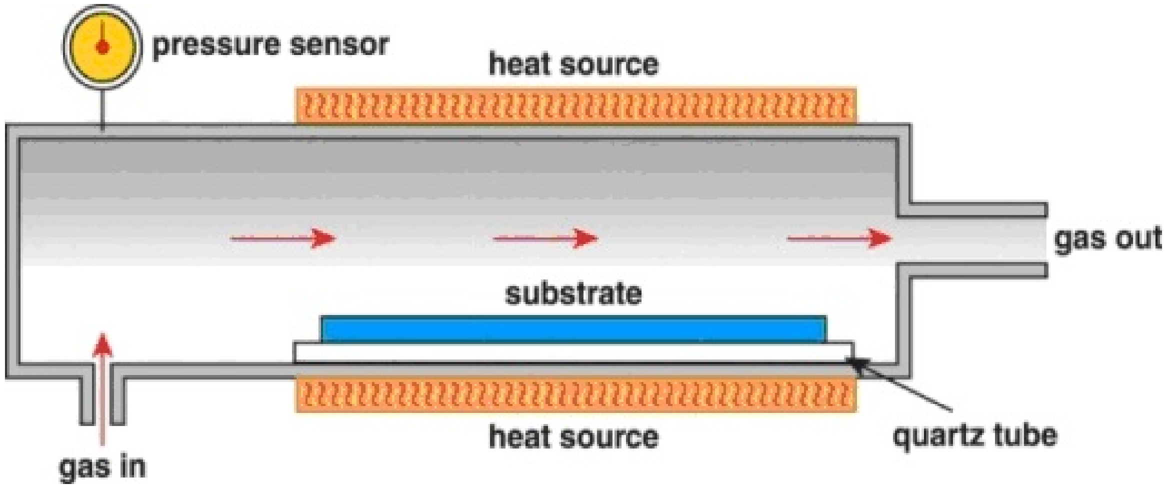

Figure 1.5 Schematic of a typical CVD reactor. Reprinted from the link in reference [56] provided by AZoNano with the permission from Strem Chemicals.

Graphene has been grown on transition metals like Ru [57], Ir [58], Co [59] and Pt [60]. The growth of graphene on relatively low cost polycrystalline Ni [61,62] and Cu [63,64] substrates have been reported recently and this achievement, in turn, has created remarkable interests in optimizing CVD conditions for the large-area synthesis of high quality graphene.

Despite the mobility up to 3650 cm^{2}V^{-1}s^{-1} [17], the single to few layered graphene formed on Ni substrate can span only over a region of few tens of microns and cannot cover the entire substrate. The micron-sized smooth regions of layers are separated from each other by ridges formed due to the difference in the thermal expansion of Ni and graphitic layers [65]. Polycrystalline Cu substrate (Fig. 1.6 a-c), however, has been used to grow monolayer graphene with uniform large area. The roll-to-roll production and wet-chemical doping of predominantly monolayer 30-inch graphene film has been grown by CVD on flexible Cu substrate (Fig. 1.6d) [66]. Recently, the group led by R. S. Ruoff was able to report the carrier mobility up to 30,000 cm^{2}V^{-1}s^{-1} at room temperature for 1-cm single crystal CVD graphene on Cu (Fig. 1.6 e) [67].

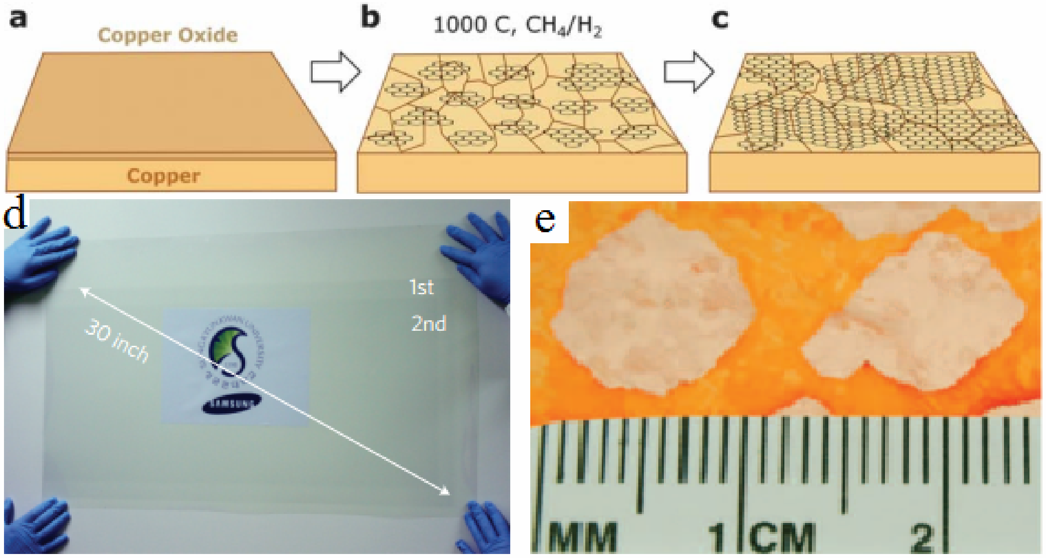

Figure 1.6 (a-c) Schematic illustrations of main steps of growth of graphene on Cu by CVD (a) Cu foil with native oxide, (b) Cu foil exposed to CH_4/H_2 atmosphere at 1000°C leading to the nucleation of graphene islands, (c) enlargement of graphene flakes with the different lattice orientations [68], (d) transparent graphene film on 35 inch PET [66], and (e) optical microscopic image of centimeter-scale graphene domains on Cu [67]. Figures a-c are reprinted from permission of reference 68, copyright 2010 The Royal Society of Chemistry, Fig. d is reprinted from the permission of reference 66, copyright 2010 Macmillan Publishers Ltd and Fig. e is reprinted from the permission of reference 67, copyright 2013 The American Association for the Advancement of Science.

In addition to the requirement of UHV and high temperature source, the challenge associated to the CVD method is that it needs a highly precise and tedious method to transfer the graphene from metal substrate to arbitrary substrate like quartz, SiO_2, etc for device fabrication. The general steps that will be followed to transfer the CVD graphene are: (a) spin-coat the polymer like poly(methyl methacrylate) (PMMA) on CVD graphene [69,70], (b) etch the CVD substrate (Ni or Cu) chemically by $FeCl_3$ [71], and (c) transfer PMMA/graphene on the target substrate and remove PMMA by dissolving into acetone [72].

Besides the CVD growth of graphene by passing hydrocarbons into the furnace, graphene has been produced by heating the solid carbonaceous materials kept on the substrate. Graphene from transition metal mediated graphitization of amorphous carbon [73], nanodiamond [74], polymers [75], and thermal decomposition of inexpensive carbon sources like cookies, chocolate, cockroach legs, plastic and dog feces have already been reported [76].

Other methods: Substrate free production of graphene has advantages that it does not require a specific substrate and no extra effort is needed to transfer the graphene to the working substrate. Also, the process is continuous rather than batch processing because the sample is often collected outside the furnace. So methods of substrate free production are scalable and capable of being commercialized. Earlier attempts to produce graphene nanosheets without a substrate are microwave enhanced CVD of ethanol [77] and thermal decomposition of sodium ethoxide in ethanol [78]. Some of the other methods include flash pyrolysis of solvothermal product of sodium and ethanol[79], igniting magnesium in dry ice[80], calcining aluminum sulfide in carbon monoxide [81], calcining calcium carbonate with magnesium powder [82], etc.

We are in the graphene "gold rush" era. There is much literature available on the synthesis of graphene and the number is ever increasing. So the brief review on the synthesis methods presented here is not a strategic update and may not include all progress, trends and opportunities for making graphene. The purpose of this review is to introduce and establish a unique and new method of graphene synthesis in the crowd of many existing methods. In 2013, our group, led by C. M. Sorensen, pioneered a new route for the production of graphene nanosheets via a controlled detonation of hydrocarbons with oxygen [83]. The detonation chamber, detonation procedure and previous experiments on the detonations of hydrocarbons into this chamber will be introduced in section 1.6.

1.6 Controlled Detonation of Hydrocarbons

All the carbon samples whose characteristics are mentioned in this dissertation were made by detonating hydrocarbons with oxidizers in a 16.6 liter aluminum chamber with a 37.1 cm height and a 23.9 cm internal diameter. The temperature and pressure of the detonations were determined by using a two-color pyrometer and pressure probe, respectively (Fig. 1.7).

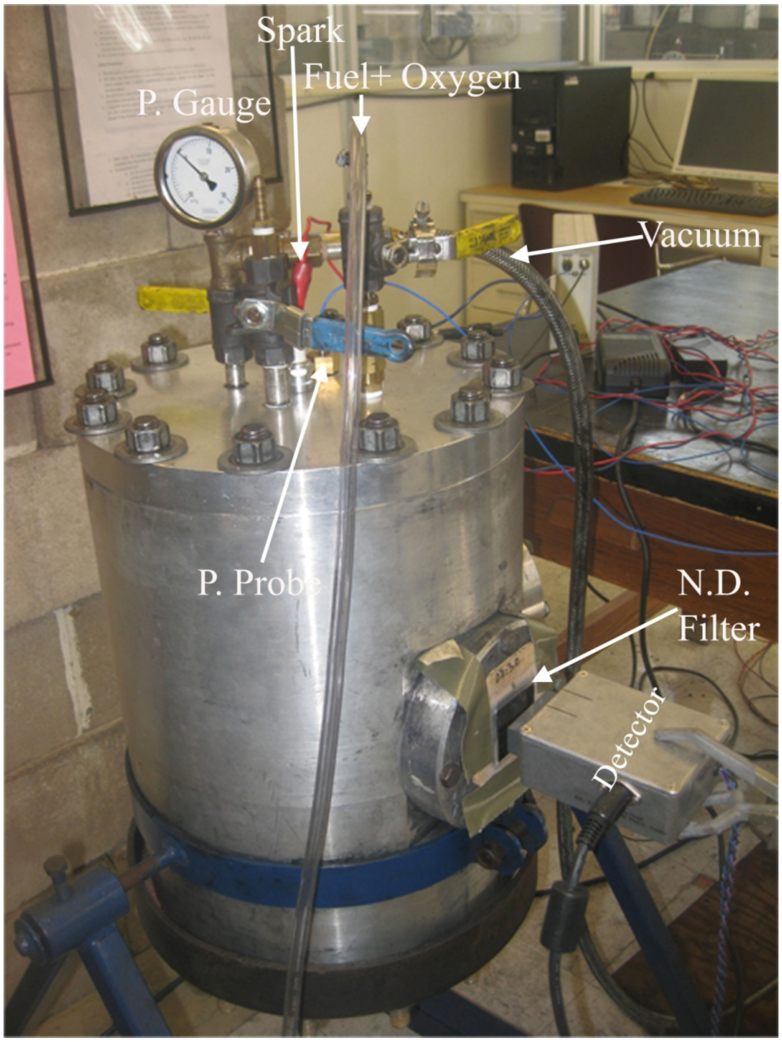

Figure 1.7 The 16.6 liter detonation chamber with pressure gauge, automotive spark plug, inlet to inject fuel and oxygen, outlet for vacuuming, optical detector that detects the light from detonation flash passing through the neutral density (N.D.) filter and pressure (P) probe.

For a typical detonation, the chamber is evacuated with a vacuum pump, and it is filled up to 1 atmosphere pressure with hydrocarbon and oxygen to a desired ratio. An electric spark is given into the chamber by tesla coil or spark generator ignition system connected to a power supply. The chamber then cools and the carbon formed inside will be collected for characterization. The peak detonation temperature is determined by the ratio of the intensity of the green and red light, emanating from the detonation, detected by the optical detector. A pressure probe measures the peak detonation pressure in the chamber. Characterizations of detonation carbon formed by detonating acetylene (C_2H_2) and ethylene (C_2H_4), propane (C_3H_8) and methane (CH_4) with oxygen (O_2) and nitrous oxide (N_2O) will be presented in this dissertation.

Earlier to the work described in this dissertation, Sorensen's group had done extensive work to understand the formation mechanism of solid carbons by hydrocarbon detonation and determined some of their physical properties. During the detonation, the hydrocarbon is first converted into nanoparticle carbon aerosols which in turn quickly aggregate and then finally forms a gel, known as a Carbon Aerosol Gel (CAG) [84]. Gaseous hydrocarbons detonated were CH_4, C_3H_8, C_2H_4 and C_2H_2. Also, the CAG formed by the detonation of liquid hydrocarbons butane (C_4H_{10}), pentane (C_5H_{12}), hexane (C_6H_{14}) and isooctane (C_8H_{18}) were studied. CAG of density 2.5-5.0 mg/cc, specific surface area 200-350 m^2/g and primary particle size ≤ 50 nm were reported [84,85].

1.7 Overview of Chapters

In chapter 2, a brief description of the tools that were used to characterize the carbon samples will be presented. Also, the theory of two-color pyrometer, its design and calibration is explained in chapter 2.

Chapter 3 will be about the synthesis of graphene nanosheets via controlled detonation of C_2H_2 with O_2. This chapter is mostly adapted from the paper " Arjun Nepal, Gajendra P Singh, Bret N Flanders and C M Sorensen, "One-step synthesis of graphene via catalyst-free gas-phase hydrocarbon detonation, 2013 Nanotechnology 24 245602 doi:10.1088/0957-4484/24/24/245602".

A series of experiments, to detonate various hydrocarbons, were carried out to produce carbon and characterize them. Also, detonation of C_2H_2 was carried out in N_2O atmosphere instead of O_2 to understand the role of oxidizer on the quality of carbon produced. Chapter 4 describes the role of hydrocarbon precursor and oxidizer in the synthesis of graphene via detonations.

Chapter 5 will describe the oxidized graphene nanosheets produced by oxidizing the pristine graphene nanosheets obtained by detonating C_2H_2 with O_2. This chapter will be adapted from the paper "A. Nepal, G. Chiu, J. Xie, G. P. Singh, N. Ploscariu, S. Klankowski, T. Sung, J. Li, B. N. Flanders, K. L. Hohn, and C. M. Sorensen, Highly Oxidized Graphene Nanosheets via the Oxidization of Detonation Carbon, 2015 Applied Physics A, doi: 10.1007/s00339-015-9213-1".

Chapter 6 will be the summary of the dissertation and future work that can be done to move along to improve the quality of detonation produced graphene nanosheets and explore their applications.

1.8 References

1. K. S. Novoselov, A. K. Geim, S. V. Morozov, D. Jiang, Y. Zhang, S. V. Dubonos, I. V. Grigorieva, and A. A. Firsov, Science **306**, 666 (2004).
2. A. K. Geim and K. S. Novoselov, Nat. Mater. **6**, 183 (2007).
3. H. W. Kroto, J. R. Heath, S. C. O'Brien, R. F. Curl, and R. E. Smalley, Nature **318**, 162 (1985).
4. S. Iijima, Nature **354**, 56 (1991).
5. N. D. Mermin, Phys. Rev. **176**, 250 (1968).
6. J. A. Venables, G. D. T. Spiller, and M. Hanbucken, Rep. Prog. Phys. **47**, 399 (1984).
7. J. W. Evans, P. A. Thiel, and M. C. Bartelt, Surf. Sci. Rep. **61**, 1 (2006).
8. E. P. Randviir, D. A. C. Brownson, and C. E. Banks, Mater. Today **17**, 426 (2014).
9. A. K. Geim, Science **324**, 1530 (2009).
10. R. F. Service, Science **324**, 875 (2009).
11. K. S. Novoselov, A. K. Geim, S. V. Morozov, D. Jiang, M. I. Katsnelson, I. V. Grigorieva, S. V. Dubonos, and A. A. Firsov, Nature **438**, 197 (2005).
12. A. M. Dato, Substrate-Free Gas-Phase Synthesis of Graphene, UNIVERSITY OF CALIFORNIA, BERKELEY, 2009.

13. C. Lee, X. Wei, J. W. Kysar, and J. Hone, Science **321**, 385 (2008).

14. J. S. Bunch, S. S. Verbridge, J. S. Alden, A. M. van der Zande, J. M. Parpia, H. G. Craighead, and P. L. McEuen, Nano Lett. **8**, 2458 (2008).

15. A. A. Balandin, S. Ghosh, W. Bao, I. Calizo, D. Teweldebrhan, F. Miao, and C. N. Lau, Nano Lett. **8**, 902 (2008).

16. R. R. Nair, P. Blake, A. N. Grigorenko, K. S. Novoselov, T. J. Booth, T. Stauber, N. M. R. Peres, and A. K. Geim, Science **320**, 1308 (2008).

17. K. S. Kim, Y. Zhao, H. Jang, S. Y. Lee, J. M. Kim, K. S. Kim, J.-H. Ahn, P. Kim, J.-Y. Choi, and B. H. Hong, Nature **457**, 706 (2009).

18. Y.-M. Lin, K. A. Jenkins, A. Valdes-Garcia, J. P. Small, D. B. Farmer, and P. Avouris, Nano Lett. **9**, 422 (2009).

19. F. Schedin, A. K. Geim, S. V. Morozov, E. W. Hill, P. Blake, M. I. Katsnelson, and K. S. Novoselov, Nat. Mater. **6**, 652 (2007).

20. Y. Liu, X. Dong, and P. Chen, Chem. Soc. Rev. **41**, 2283 (2012).

21. S. Stankovich, D. A. Dikin, G. H. B. Dommett, K. M. Kohlhaas, E. J. Zimney, E. A. Stach, R. D. Piner, S. T. Nguyen, and R. S. Ruoff, Nature **442**, 282 (2006).

22. S. Watcharotone, D. A. Dikin, S. Stankovich, R. Piner, I. Jung, G. H. B. Dommett, G. Evmenenko, S.-E. Wu, S.-F. Chen, C.-P. Liu, S. T. Nguyen, and R. S. Ruoff, Nano Lett. **7**, 1888 (2007).

23. T. Takamura, K. Endo, L. Fu, Y. Wu, K. J. Lee, and T. Matsumoto, Electrochimica Acta **53**, 1055 (2007).

24. R. S. Edwards and K. S. Coleman, Nanoscale **5**, 38 (2012).

25. K. Seibert, G. C. Cho, W. Kütt, H. Kurz, D. H. Reitze, J. I. Dadap, H. Ahn, M. C. Downer, and A. M. Malvezzi, Phys. Rev. B **42**, 2842 (1990).

26. X. Lu, H. Huang, N. Nemchuk, and R. S. Ruoff, Appl. Phys. Lett. **75**, 193 (1999).

27. A. van der Zande, THE STRUCTURE AND MECHANICS OF ATOMICALLY-THIN GRAPHENE MEMBRANES, Cornell University, 2011.

28. W. S. Hummers and R. E. Offeman, J. Am. Chem. Soc. **80**, 1339 (1958).

29. B. C. Brodie, Philos. Trans. R. Soc. Lond. **149**, 249 (1859).

30. D. C. Marcano, D. V. Kosynkin, J. M. Berlin, A. Sinitskii, Z. Sun, A. Slesarev, L. B. Alemany, W. Lu, and J. M. Tour, ACS Nano **4**, 4806 (2010).

31. S. Lee, J. Oh, R. S. Ruoff, and S. Park, Carbon **50**, 1442 (2012).

32. A. Lerf, H. He, M. Forster, and J. Klinowski, J. Phys. Chem. B **102**, 4477 (1998).

33. H. He, J. Klinowski, M. Forster, and A. Lerf, Chem. Phys. Lett. **287**, 53 (1998).

34. D. R. Dreyer, S. Park, C. W. Bielawski, and R. S. Ruoff, Chem. Soc. Rev. **39**, 228 (2009).

35. L. M. Viculis, J. J. Mack, O. M. Mayer, H. T. Hahn, and R. B. Kaner, J. Mater. Chem. **15**, 974 (2005).

36. X. Li, G. Zhang, X. Bai, X. Sun, X. Wang, E. Wang, and H. Dai, Nat. Nanotechnol. **3**, 538 (2008).

37. T. Wei, Z. Fan, G. Luo, C. Zheng, and D. Xie, Carbon **47**, 337 (2009).

38. C.-Y. Su, A.-Y. Lu, Y. Xu, F.-R. Chen, A. N. Khlobystov, and L.-J. Li, ACS Nano **5**, 2332 (2011).

39. G. Wang, B. Wang, J. Park, Y. Wang, B. Sun, and J. Yao, Carbon **47**, 3242 (2009).

40. H. Huang, Y. Xia, X. Tao, J. Du, J. Fang, Y. Gan, and W. Zhang, J. Mater. Chem. **22**, 10452 (2012).

41. J. Wang, K. K. Manga, Q. Bao, and K. P. Loh, J. Am. Chem. Soc. **133**, 8888 (2011).

42. K. S. Suslick and G. J. Price, Annu. Rev. Mater. Sci. **29**, 295 (1999).

43. Y. Hernandez, V. Nicolosi, M. Lotya, F. M. Blighe, Z. Sun, S. De, I. T. McGovern, B. Holland, M. Byrne, Y. K. Gun'Ko, J. J. Boland, P. Niraj, G. Duesberg, S. Krishnamurthy, R. Goodhue, J. Hutchison, V. Scardaci, A. C. Ferrari, and J. N. Coleman, Nat. Nanotechnol. **3**, 563 (2008).

44. P. Blake, P. D. Brimicombe, R. R. Nair, T. J. Booth, D. Jiang, F. Schedin, L. A. Ponomarenko, S. V. Morozov, H. F. Gleeson, E. W. Hill, A. K. Geim, and K. S. Novoselov, Nano Lett. **8**, 1704 (2008).

45. S. Farhat and C. D. Scott, J. Nanosci. Nanotechnol. **6**, 1189 (2006).

46. K. S. Subrahmanyam, L. S. Panchakarla, A. Govindaraj, and C. N. R. Rao, J. Phys. Chem. C **113**, 4257 (2009).

47. H. Z. Yani Chen, Chem. Phys. Lett. **538**, 72 (2012).

48. L. Jiao, L. Zhang, X. Wang, G. Diankov, and H. Dai, Nature **458**, 877 (2009).

49. D. V. Kosynkin, A. L. Higginbotham, A. Sinitskii, J. R. Lomeda, A. Dimiev, B. K. Price, and J. M. Tour, Nature **458**, 872 (2009).

50. P. Kumar, L. S. Panchakarla, and C. N. R. Rao, Nanoscale **3**, 2127 (2011).

51. J. Hass, W. A. de Heer, and E. H. Conrad, J. Phys. Condens. Matter **20**, 323202 (2008).

52. C. Berger, Z. Song, T. Li, X. Li, A. Y. Ogbazghi, R. Feng, Z. Dai, A. N. Marchenkov, E. H. Conrad, P. N. First, and W. A. de Heer, J. Phys. Chem. B **108**, 19912 (2004).

53. K. V. Emtsev, A. Bostwick, K. Horn, J. Jobst, G. L. Kellogg, L. Ley, J. L. McChesney, T. Ohta, S. A. Reshanov, J. Röhrl, E. Rotenberg, A. K. Schmid, D. Waldmann, H. B. Weber, and T. Seyller, Nat. Mater. **8**, 203 (2009).

54. Z.-Y. Juang, C.-Y. Wu, C.-W. Lo, W.-Y. Chen, C.-F. Huang, J.-C. Hwang, F.-R. Chen, K.-C. Leou, and C.-H. Tsai, Carbon **47**, 2026 (2009).

55. S. Unarunotai, Y. Murata, C. E. Chialvo, H. Kim, S. MacLaren, N. Mason, I. Petrov, and J. A. Rogers, Appl. Phys. Lett. **95**, 202101 (2009).

56. http://www.azonano.com/article.aspx?ArticleID=3430.

57. P. W. Sutter, J.-I. Flege, and E. A. Sutter, Nat. Mater. **7**, 406 (2008).

58. J. Coraux, A. T. N'Diaye, C. Busse, and T. Michely, Nano Lett. **8**, 565 (2008).

59. S. M. Wang, Y. H. Pei, X. Wang, H. Wang, Q. N. Meng, H. W. Tian, X. L. Zheng, W. T. Zheng, and Y. C. Liu, J. Phys. Appl. Phys. **43**, 455402 (2010).

60. T. Gao, S. Xie, Y. Gao, M. Liu, Y. Chen, Y. Zhang, and Z. Liu, ACS Nano **5**, 9194 (2011).

61. A. Reina, X. Jia, J. Ho, D. Nezich, H. Son, V. Bulovic, M. S. Dresselhaus, and J. Kong, Nano Lett. **9**, 30 (2009).

62. L. Gomez De Arco, Y. Zhang, C. W. Schlenker, K. Ryu, M. E. Thompson, and C. Zhou, ACS Nano **4**, 2865 (2010).

63. D. Wei, Y. Liu, Y. Wang, H. Zhang, L. Huang, and G. Yu, Nano Lett. **9**, 1752 (2009).

64. X. Li, W. Cai, J. An, S. Kim, J. Nah, D. Yang, R. Piner, A. Velamakanni, I. Jung, E. Tutuc, S. K. Banerjee, L. Colombo, and R. S. Ruoff, Science **324**, 1312 (2009).

65. A. N. Obraztsov, E. A. Obraztsova, A. V. Tyurnina, and A. A. Zolotukhin, Carbon **45**, 2017 (2007).

66. S. Bae, H. Kim, Y. Lee, X. Xu, J.-S. Park, Y. Zheng, J. Balakrishnan, T. Lei, H. Ri Kim, Y. I. Song, Y.-J. Kim, K. S. Kim, B. Özyilmaz, J.-H. Ahn, B. H. Hong, and S. Iijima, Nat. Nanotechnol. **5**, 574 (2010).

67. Y. Hao, M. S. Bharathi, L. Wang, Y. Liu, H. Chen, S. Nie, X. Wang, H. Chou, C. Tan, B. Fallahazad, H. Ramanarayan, C. W. Magnuson, E. Tutuc, B. I. Yakobson, K. F. McCarty, Y.-W. Zhang, P. Kim, J. Hone, L. Colombo, and R. S. Ruoff, Science **342**, 720 (2013).

68. C. Mattevi, H. Kim, and M. Chhowalla, J. Mater. Chem. **21**, 3324 (2011).

69. Y.-C. Lin, C. Jin, J.-C. Lee, S.-F. Jen, K. Suenaga, and P.-W. Chiu, ACS Nano **5**, 2362 (2011).

70. A. Pirkle, J. Chan, A. Venugopal, D. Hinojos, C. W. Magnuson, S. McDonnell, L. Colombo, E. M. Vogel, R. S. Ruoff, and R. M. Wallace, Appl. Phys. Lett. **99**, 122108 (2011).

71. R. S. Edwards and K. S. Coleman, Acc. Chem. Res. **46**, 23 (2013).

72. Y. Zhang, L. Zhang, and C. Zhou, Acc. Chem. Res. **46**, 2329 (2013).

73. M. Zheng, K. Takei, B. Hsia, H. Fang, X. Zhang, N. Ferralis, H. Ko, Y.-L. Chueh, Y. Zhang, R. Maboudian, and A. Javey, Appl. Phys. Lett. **96**, 063110 (2010).

74. J. M. García, R. He, M. P. Jiang, P. Kim, L. N. Pfeiffer, and A. Pinczuk, Carbon **49**, 1006 (2011).

75. Z. Sun, Z. Yan, J. Yao, E. Beitler, Y. Zhu, and J. M. Tour, Nature **468**, 549 (2010).

76. G. Ruan, Z. Sun, Z. Peng, and J. M. Tour, ACS Nano **5**, 7601 (2011).

77. A. Dato, V. Radmilovic, Z. Lee, J. Phillips, and M. Frenklach, Nano Lett. **8**, 2012 (2008).

78. C. R. Herron, K. S. Coleman, R. S. Edwards, and B. G. Mendis, J. Mater. Chem. **21**, 3378 (2011).

79. M. Choucair, P. Thordarson, and J. A. Stride, Nat. Nanotechnol. **4**, 30 (2009).

80. A. Chakrabarti, J. Lu, J. C. Skrabutenas, T. Xu, Z. Xiao, J. A. Maguire, and N. S. Hosmane, J. Mater. Chem. **21**, 9491 (2011).

81. C.-D. Kim, B.-K. Min, and W.-S. Jung, Carbon **47**, 1610 (2009).

82. J. Zhao, Y. Guo, Z. Li, Q. Guo, J. Shi, L. Wang, and J. Fan, Carbon **50**, 4939 (2012).

83. A. Nepal, G. P. Singh, B. N. Flanders, and C. M. Sorensen, Nanotechnology **24**, 245602 (2013).

84. R. Dhaubhadel, C. S. Gerving, A. Chakrabarti, and C. M. Sorensen, Aerosol Sci. Technol. **41**, 804 (2007).

85. R. Dhaubhadel, An Experimental Study of Dense Aerosol Aggregations (BiblioBazaar, 2012).

Chapter 2 - Experimental Procedures

2.1 Overview

All of the detonation experiments related to the work mentioned in this dissertation were carried out in a 16.6 liter aluminum detonation chamber following the method explained in Chapter 1. At the start of this work, summer 2010, the initial aim was to reproduce carbon aerosol gel (CAG) by following the procedure adopted by previous members of Sorensen's group and to investigate more properties of this new material. Characterizations of CAG by x-ray diffraction (XRD) and Raman spectroscopy (RS) followed by a careful comparison of the corresponding spectra with those available in literature have revealed that the microstructure of CAG resembled to that of graphene nanosheets. These startling observations, then, led us to set up a legitimate hypothesis that the detonation created *in situ* temperature is so high that it satisfies the condition required to produce graphene. Then a two-color pyrometer and a dynamic pressure sensor were added to the chamber to measure the detonation temperature and pressure, respectively. In the first part of Chapter 2, a description of theory, calibration and performance of a two-color pyrometer is given along with the introduction of the pressure sensor we used. We will give brief introduction to the characterization tools that we have used to characterize the GNs and OGNs at the end of this chapter.

2.2 Two-Color Pyrometer

2.2.1 Theory

The temperature of detonation of hydrocarbons, we hypothesize, is very high and hence the surface temperature of the detonation produced material is assumed to be higher than the gold point (1064.43°C). A radiation thermometer or pyrometer is suitable to measure the surface temperatures above gold point [1]. A pyrometer is based on the Planck law for black body radiation, and it is given as

$$q_{b\lambda}(T) = \frac{2hc^2}{\lambda^5}\frac{1}{e^{\frac{hc}{\lambda kT}} - 1}$$

where, $q_{b\lambda}(T)$ is spectral emissive power of the black body, and it is function of wavelength λ and temperature T of the body, k is the Boltzmann constant, h is the Planck's constant and c is the speed of light in vacuum. For simplicity, the following constants are redefined in the above equation.

$C_1 = 2hc^2$ and $C_2 = \frac{hc}{k}$

Now the equation for Planck's law becomes,

$$q_{b\lambda}(T) = \frac{C_1}{\lambda^5} \frac{1}{e^{\frac{C_2}{\lambda T}} - 1} \qquad (1)$$

Figure 2.1 shows a plot of q versus λ in Eq. (1) for T= 3000 K and 5000 K.

If we know the emissive power at any known wavelength, say 515 nm (green) or 680 nm (red), of the radiation emanating from the hot surface, the temperature of the corresponding surface can be determined. This concept is used to make a pyrometer. The mathematical steps, based mainly on reference [1], presented below show how the temperature of a hot surface will be determined by using this concept.

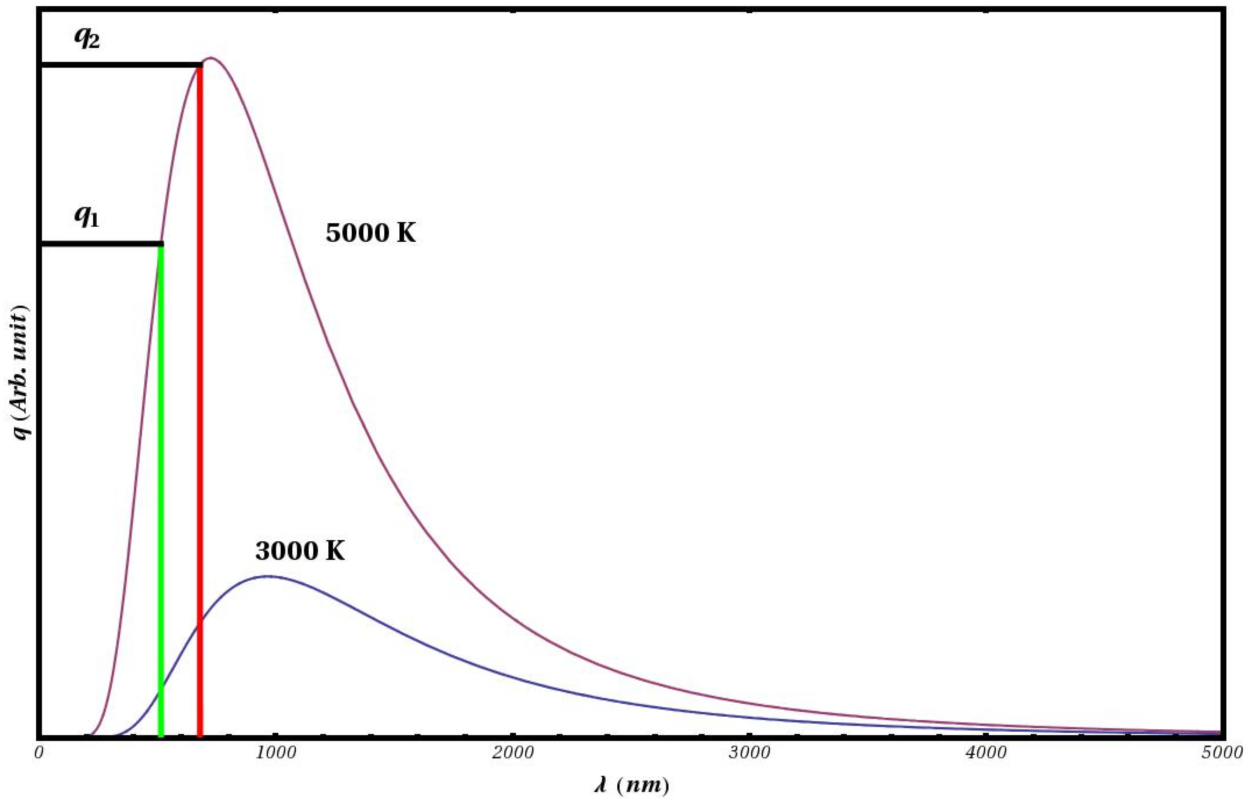

Figure 2.1 Planck's law of black body radiation for T= 3000 K and 5000 K

For small wavelengths, $e^{\frac{C_2}{\lambda T}} \gg 1$, so '-1' in the denominator of Eq. (1) can be dropped for simplicity.

$$q_{b\lambda}(T) = \frac{C_1}{\lambda^5}\frac{1}{e^{\frac{C_2}{\lambda T}}} \qquad (2)$$

This is called Wien's approximation to Planck's law, and it is considered as the theory of the pyrometer.

In addition to the simplicity in calculations, the errors in the calculation of temperature, committed by using Wien's approximation are minimal[1]. For example, the maximum error that comes due to this approximation at 6000 K is only about 1.3% for radiation of a wavelength of 550 nm as shown in Fig. 2.2.

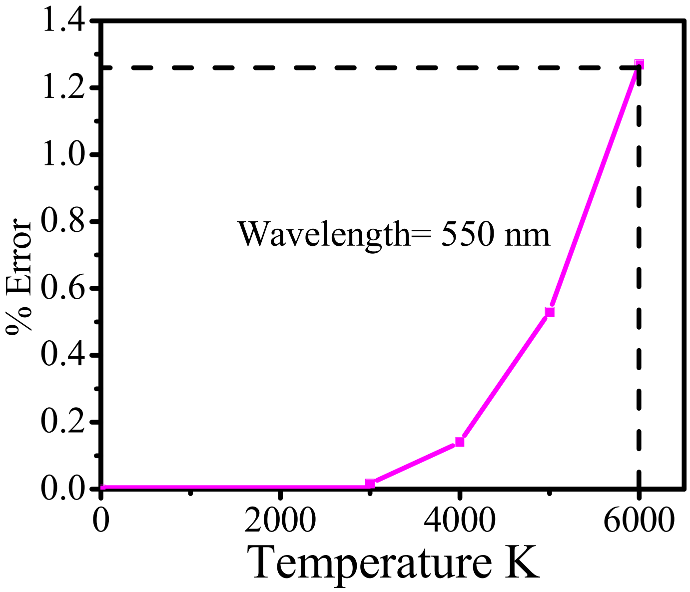

Figure 2.2 Error due to Wien's approximation

For a design of the pyrometer, it is necessary to define brightness temperature, which is the temperature of true black body at which it has the same emissive power equal to that of actual body surface at a particular wavelength [1].

$$q_{a\lambda}(T_a) = q_{b\lambda}(T_b) \qquad (3)$$

Where T_a is the temperature of the actual surface and the T_b is the brightness temperature.

When the body is not a black body, like a burning carbon aerosol, the term emissivity, e_λ, is used. e_λ actually tells how close is the radiation from a body to that from a true black body. e_λ <1 for real object, and e_λ =1 for a perfect black body. So, it is obvious that $T_a > T_b$ because of the emissivity of the actual surface.

From Eqs. (2) and (3), we can write,

$$e_\lambda \frac{C_1}{\lambda^5} \exp\left(-\frac{C_2}{\lambda T_a}\right) = \frac{C_1}{\lambda^5} \exp\left(-\frac{C_2}{\lambda T_b}\right) \qquad (4)$$

This gives, $e_\lambda \exp\left(-\frac{C_2}{\lambda T_a}\right) = \exp\left(-\frac{C_2}{\lambda T_b}\right)$

$$e_\lambda = \exp[\mathrm{C}_2/\lambda\left(-\frac{1}{T_b} + \frac{1}{T_a}\right)]$$

$$\frac{1}{T_a} - \frac{1}{T_b} = \frac{\lambda}{\mathrm{C}_2} \ln(e_\lambda) \qquad (5)$$

This is the ideal pyrometer equation.

The basis for a two-color pyrometer is that the ratio of emissive power of the actual surface at two very close wavelengths λ_1 and λ_2 should be the same as the corresponding ratio for the black body. Moreover, the emissivity of the surface at the chosen wavelengths needs to be equal or very close to each other [1].

$$\frac{q_{a\lambda_1}(T_a)}{q_{a\lambda_2}(T_a)} = \frac{q_{b\lambda_1}(T_b)}{q_{b\lambda_2}(T_b)} \qquad (6)$$

From Eqs. (2) and (6),

$$\frac{e_{\lambda_1}}{e_{\lambda_2}} \exp\,[\left(-\frac{1}{\lambda_1} + \frac{1}{\lambda_2}\right) \frac{\mathrm{C}_2}{T_a} = \exp\,[\left(-\frac{1}{\lambda_1} + \frac{1}{\lambda_2}\right) \frac{\mathrm{C}_2}{T_b}$$

$$\exp\,[\left(-\frac{1}{\lambda_1} + \frac{1}{\lambda_2}\right) \mathrm{C}_2 \left(\frac{1}{\mathrm{T_a}} - \frac{1}{\mathrm{T_b}}\right)] = \frac{e_{\lambda_2}}{e_{\lambda_1}}$$

$$\frac{1}{T_a} = \frac{\ln\left(\frac{e_{\lambda_2}}{e_{\lambda_1}}\right)}{C_2\left(-\frac{1}{\lambda_1} + \frac{1}{\lambda_2}\right)} + \frac{1}{T_b} \qquad (7)$$

In Eq. (7), the term $\frac{1}{T_b}$ in the right side can be eliminated as follows.

The emissive powers of black body at temperature T_b at wavelengths $\lambda_1$and λ_2 are given by Wien's approximation:

For λ_1, $q_{b\lambda_1}(T_b) = \frac{C_1}{\lambda_1{}^5}\exp\left(-\frac{C_2}{\lambda_1 T_b}\right)$

For λ_2, $q_{b\lambda_2}(T_b) = \frac{C_1}{\lambda_2{}^5}\exp\left(-\frac{C_2}{\lambda_2 T_b}\right)$

Now,

$$\frac{q_{b\lambda_1}(T_b)}{q_{b\lambda_2}(T_b)} = \left(\frac{\lambda_2}{\lambda_1}\right)^5 \exp\left[\frac{C_2}{T_b}\left(\frac{1}{\lambda_2}-\frac{1}{\lambda_1}\right)\right] \qquad (8)$$

From the condition for two-color (or ratio) pyrometer mentioned in equation (6), using Eq. (8),

$$\frac{q_{a\lambda_1}(T_a)}{q_{a\lambda_2}(T_a)} = \left(\frac{\lambda_2}{\lambda_1}\right)^5 \exp\left[\frac{C_2}{T_b}\left(\frac{1}{\lambda_2}-\frac{1}{\lambda_1}\right)\right]$$

$$\frac{1}{T_b} = \frac{\ln\left[\frac{q_{a\lambda_1}(T_a)}{q_{a\lambda_2}(T_a)}\left(\frac{\lambda_1}{\lambda_2}\right)^5\right]}{C_2\left(\frac{1}{\lambda_2}-\frac{1}{\lambda_1}\right)} \qquad (9)$$

Substituting Eq. (9) in Eq. (7),

$$\frac{1}{T_a} = \frac{\ln\left(\frac{e_{\lambda 2}}{e_{\lambda 1}}\right)}{C_2\left(\frac{1}{\lambda_2}-\frac{1}{\lambda_1}\right)} + \frac{\ln\left[\frac{q_{a\lambda_1}(T_a)}{q_{a\lambda_2}(T_a)}\left(\frac{\lambda_1}{\lambda_2}\right)^5\right]}{C_2\left(\frac{1}{\lambda_2}-\frac{1}{\lambda_1}\right)}$$

$$\frac{1}{T_a} = \frac{\ln\left[\frac{q_{a\lambda_1}(T_a)}{q_{a\lambda_2}(T_a)}\left(\frac{\lambda_1}{\lambda_2}\right)^5\frac{e_{\lambda 2}}{e_{\lambda 1}}\right]}{C_2\left(\frac{1}{\lambda_2}-\frac{1}{\lambda_1}\right)}$$

$$T_a = \frac{C_2\left(\frac{1}{\lambda_2}-\frac{1}{\lambda_1}\right)}{\ln\left[\frac{q_{a\lambda_1}(T_a)}{q_{a\lambda_2}(T_a)}\left(\frac{\lambda_1}{\lambda_2}\right)^5\frac{e_{\lambda 2}}{e_{\lambda 1}}\right]} \qquad (10)$$

Equation (10) is the equation that is used as the principle to build a two-color pyrometer in the detonation lab.

2.2.2 Design and Working Equation

Figure 2.3 shows the schematic of the detonation chamber with the two-color pyrometer (detector) and dynamic pressure sensor. The optical detector consists of two band-pass filters centered at wavelengths λ_1= 515 nm (Edmund Optics, item number : 65-638) in green color and λ_2= 680 nm (Edmund Optics, item number: 67-770) in red color in the figure. The detonation flash of light emergent from the quartz window of the chamber passes through the reflective neutral density filter (ND filter, Optical Density= 3.0, provided by Edmund Optics, item number: 46-126) and falls on these band-pass filters. The green and red light emerged through these filters is then incident on the corresponding photodiodes. The electronic signal, proportional to the power of incident light, from the photodiodes will be acquired by data acquisition system (Model: NI USB-6210, National Instrument) and displayed on the computer in volts.

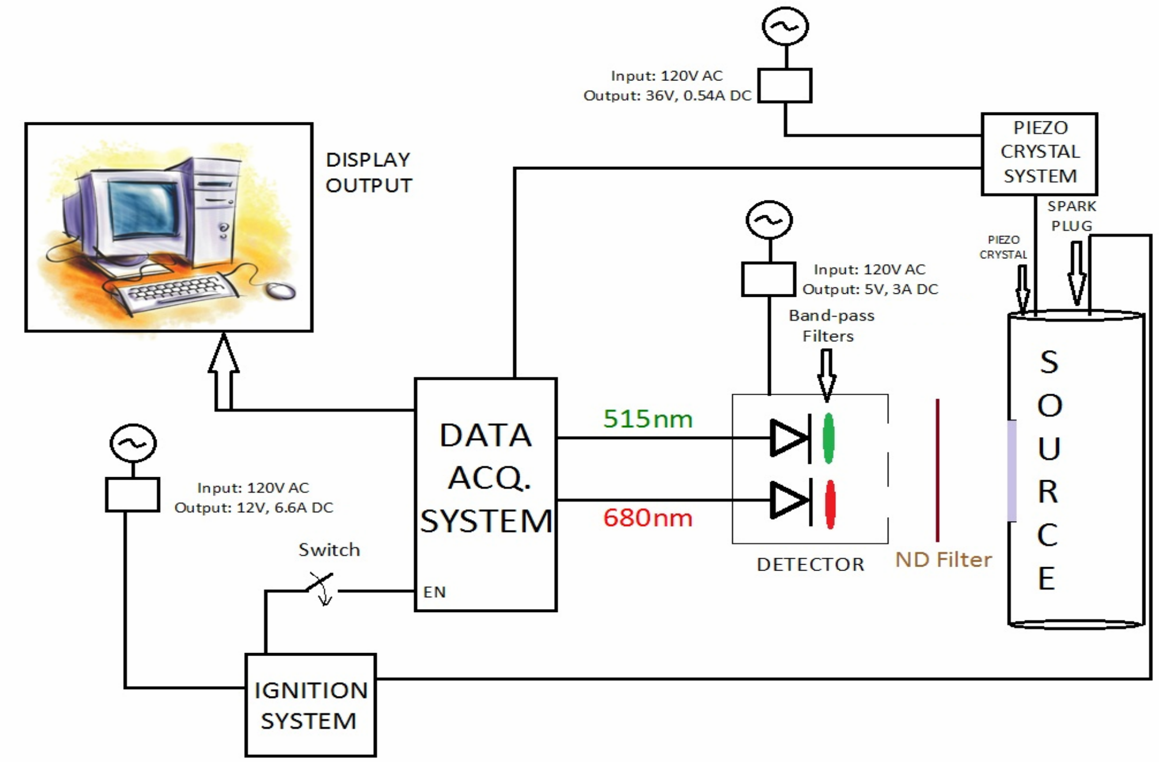

Figure 2.3 The schematic of the detonation chamber with the two-color pyrometer (detector) and dynamic pressure sensor.

The ratio of the peak value of the displayed signals in volts is basically the measured experimental ratio, R_{ex}, and it is equivalent to:

$$R_{ex} = \frac{Power\ of signal\ of\ \lambda_1}{Power\ of\ signal\ of\ \lambda_2} \qquad (11)$$

This value of R_{ex} will be compared with the assumed true ratio, $R_{true} = \frac{q_{a\lambda_1}(T_a)}{q_{a\lambda_2}(T_a)}$ of emissive powers appeared in the denominator of equation (10) to get a calibration constant C from the relation,

$$\boldsymbol{R_{true} = C\ R_{ex}}$$

Choosing the following numbers for constants,

$$C_2 = \frac{hc}{k} = \frac{6.6 * 10^{-34}\ JS * 3 * 10^8 m/s}{1.38 * 10^{-23}\ \mathrm{m^2 kg\ s^2\ K^{-1}}} = 0.0144m\mathrm{K}$$

$$\lambda_1 = 5.15 * 10^{-7}\mathrm{m}$$

$$\lambda_2 = 6.80 * 10^{-7}\mathrm{m}$$

we get equation (10) as,

$$\boldsymbol{T_a = \frac{-6784.7}{\ln\left[C * \ R_{ex} \ * \ 0.2492\right]}} \qquad (12)$$

This is the working equation that is used to determine the temperature of a typical detonation in the lab.

2.2.3 Calibration and Performance

A two-color pyrometer is usually calibrated by measuring radiation from a black body cavity furnace or melting tungsten filament. We did not use both of these standard calibrating tools, and instead we used an unconventional, cheapest and most abundant calibration tool- the sunlight. We have used the standard terrestrial solar radiation spectrum, Fig. 2.4, published by the American Society for Testing and Materials (ASTM) to calibrate the pyrometer we made. Legitimacy of this choice lies in the claim made by ASTM that the spectra are representative of average conditions in the 48 contiguous states of the United States of the places of a turbidity of 0.27 and a tilt of 37° facing the sun and a ground albedo of 0.2 [2]. Thus, the true ratio of the emissive power at 515 nm (green line) to that at 680 nm (red line) from Fig. 2.4 was $R_{true} = 1.2$.

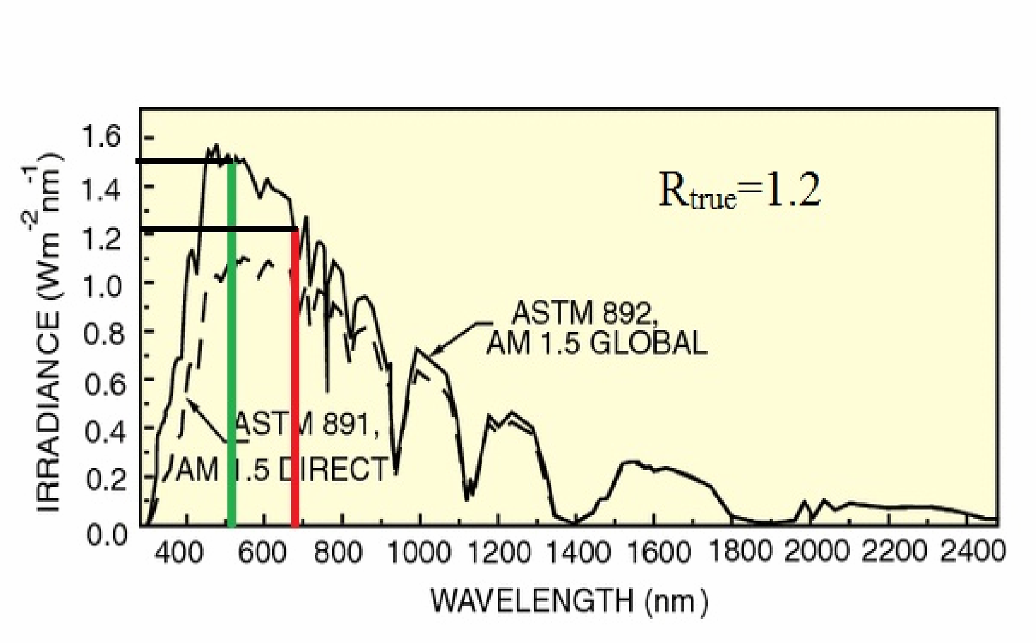

Figure 2.4 Standard spectra for AM 1.5. The direct spectrum is from ASTM E891 and global spectrum is from ASTM E892 [2]

To measure the experimental ratio of the emissive powers, a diffuser was illuminated by the sunlight by placing it on the ground outside the detonation lab in a sunny day as shown in Fig. 2.5.

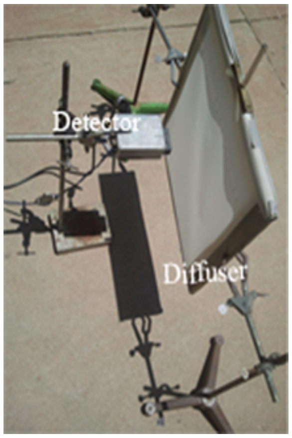

Figure 2.5 Experimental setup for the measurement of sunlight at ~ 12:00 noon. The detector is pointing into the region of diffuser illuminated by the light. The dark patches on the ground are the shadow of detector and diffuser itself and clamps used to hold it. The dark region on the upper part of the diffuser is the shadow of the frame holding it from that side.

The measurement of the diffused sunlight through the pyrometer has shown almost the same experimental ratio of emissive powers, R_{ex}= 0.33, in morning, afternoon and evening sunlight measured for about 4 weeks. Figure 2.6 shows the representative data.

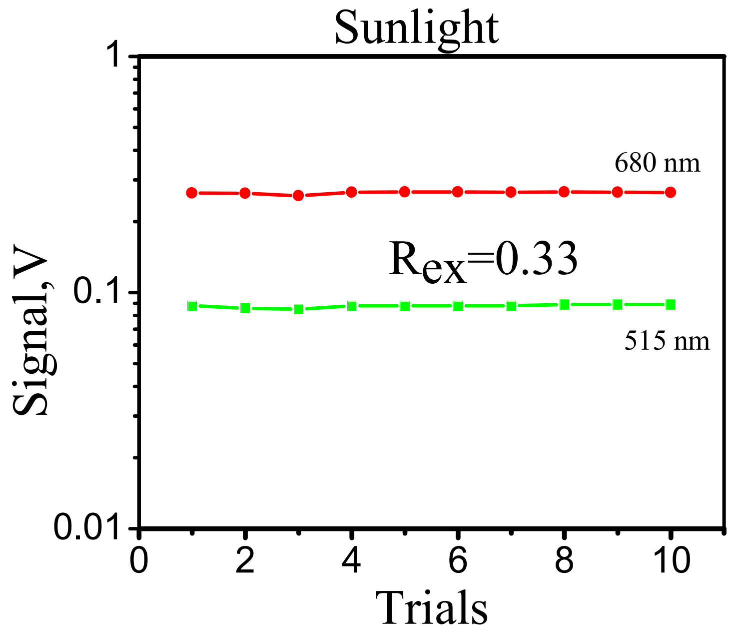

Figure 2.6 Measurement of sunlight with two-color pyrometer.

With R_{true} = 1.2 from Fig. 2.4 and R_{ex} = 0.33 from Fig. 2.6 plugged into $\boldsymbol{R_{true} = C\ R_{ex}}$, the calculated calibration constant was found to be *C=3.6.* As a test of this calibration tool, the temperature of the sun was determined by substituting *C* and R_{ex} in Eq. (12) and found to be T_a= 5600 K ±200 K. This is a very reasonable value for the temperature of sun's surface and hence the choice of standard solar spectrum as a calibration tool seems okay.

The two-color pyrometer calibrated from the sunlight was also tested by measuring the radiation of uniform intensity coming off the tungsten filament lamps. Figure 2.7 shows the experimental set up to measure the lamp light. The diffuser was illuminated by light from three 100 watts tungsten filament lamps kept in series. The lamps in series were used to create a region of uniform intensity of light, which in turn, makes sure that both filters on the detector are acquiring the same intensity of lamp light. The detector was pointed to the diffuser from the other side (Fig. 2.7).

Figure 2.7 Experimental setup for the measurement of radiation from the filament lamp by the two color pyrometer

The measured experimental ratio for lamp light was R_{ex}= 0.13 as shown in Fig. 2.8(a). The calibration constants calculated from this R_{ex} and four probable temperatures of filament lamps were plotted against the corresponding temperatures and kept along with the same graph for sunlight for comparison as shown in Fig. 2.8(b). The intersection point of the two lines is at T_a=3200 K±200 K (Fig. 2.8b), and it corresponds to the temperature of the tungsten filament lamp. This value of temperature is a reasonable value relative to that quoted value of temperature of a glowing filament of tungsten lamp.

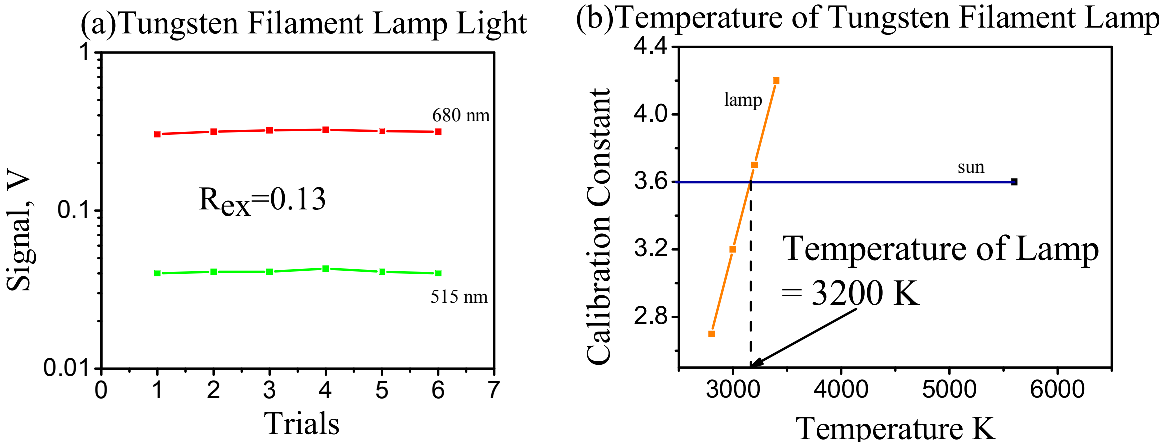

Figure 2.8 (a) Measurement of radiation from the filament lamp by the two color pyrometer and (b) determination of temperature of the lamp using the calibration constant from the measurement of sunlight.

The measured temperature of the sun and the filament lamp were precise enough to validate the choice of the standard solar spectrum as a calibration tool. The calibrated pyrometer was then used to measure the detonation temperatures. The signal intensity detected by the pyrometer from light of wavelengths 515 nm and 680 nm coming off from a typical detonation and the corresponding peak detonation temperature calculated from Eq. (12) are shown in Fig. 2.9.

Figure 2.9 presents the signal of light intensity versus time after the ignition system is turned on acquired through pyrometer during the detonation which is completed in 40 ms. When the detonation light flash is higher than the background light, the intensity of the both signals recorded by pyrometer follow almost the same pattern of the variation with time, and it continues for about 15 ms (see from 20 ms to 35 ms in Fig. 2.9). The peak detonation temperature corresponds to the temperature calculated where the intensity of the signals are maximum, and it is around 3900 ± 200 K at 26 ms for the case shown in Fig. 2.9. Temperatures lower than ca. 2000 K are supposed impossible be measured accurately with the present pyrometer design because the signals from a detonation with low peak detonation temperature are very weak and prone to be influenced more from the background signal/noises. Nevertheless, it is apparent that the rapid cooling from the peak temperature occurs in ca.6 ms [3]

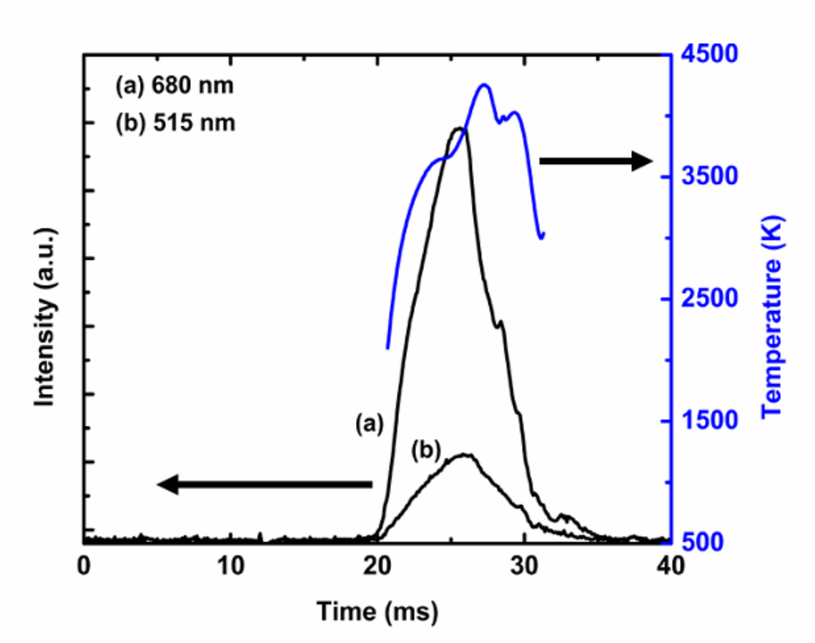

Figure 2.9 Signals of intensity of light versus time for a typical detonation acquired by the pyrometer system and the corresponding temperature after the ignition system is turned on [3]

As an additional independent cross-check of the correctness of the measured temperatures from the two-color pyrometer, the measured temperatures of detonations of mixture of acetylene (mole percentage from 50% to 95%) and oxygen were compared with those reported by the other groups in previous work. Figure 2.10 shows the temperatures of detonations determined by three different groups including us.

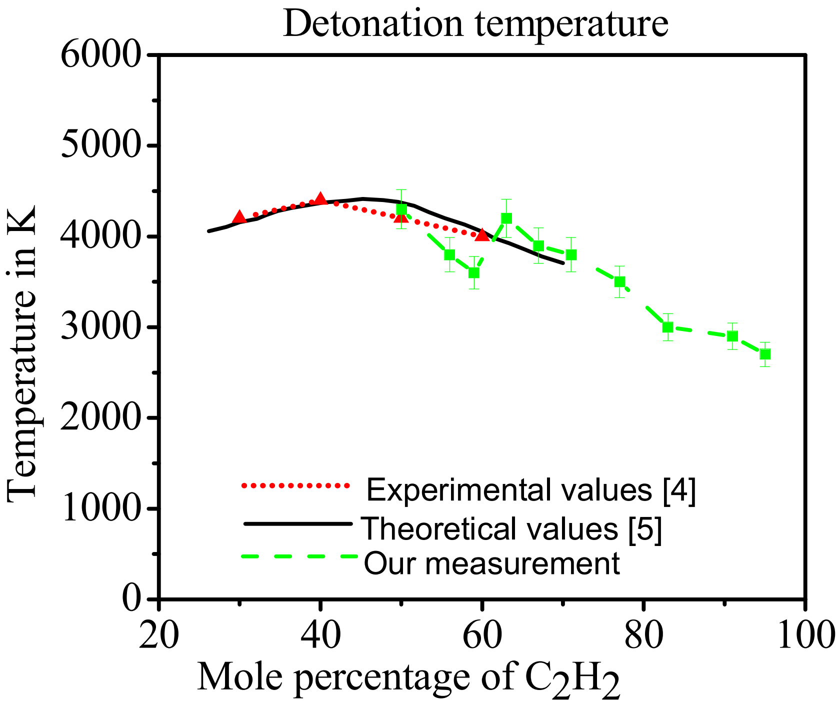

Figure 2.10 Comparison of temperature of detonation of acetylene and oxygen mixture measured by the two-color pyrometer with that determined by earlier works [4,5] reproduced from the permission of reference [6], copyright 1970 American Chemical Society.

The measured temperature of detonation, qualitatively, increases from ca. 2700 K (for 95% mole percentage of C_2H_2) to ca. 4300 K (for 50% mole percentage of C_2H_2). These temperatures are almost consistent with those measured by earlier groups as shown in Fig. 2.10. So, we rely on the measurements of this pyrometer. Temperatures of all the detonations of hydrocarbon and oxygen mixture were determined by using this pyrometer.

2.3 Dynamic Pressure Sensor

The measurement of detonation pressure was carried out by piezo-electric pressure transducer (PCB Piezotronics Inc., Model: 113B22) with signal conditioner (PCB Piezotronics Inc., Model: 482A21) installed in the lid of the detonation chamber as shown in the figure 2.3.

During a typical detonation, the pressure rises rapidly, reaches a maximum for an instant and then decreases exponentially, as shown in Fig. 2.11. The maximum pressure rise, called the peak detonation pressure, is the one that we will report as the detonation pressure. In the detonation presented in Fig. 2.11, for example, the peak detonation pressure is 13.6 atmospheres.

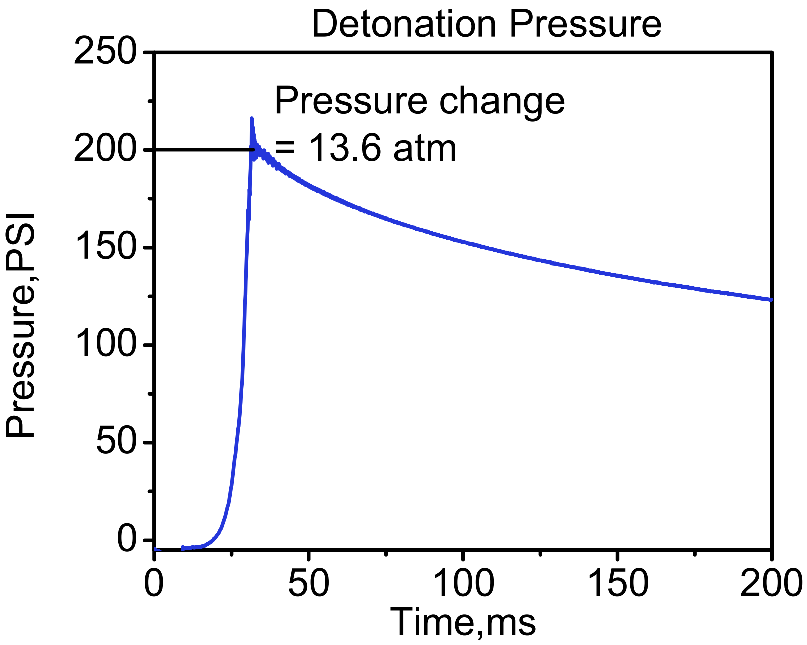

Figure 2.11 Signal corresponding to the pressure developed during a typical detonation, observed peak detonation pressure is 13.6 ±1.5 atm.

2.4 Characterization Tools

Graphene and graphene oxide samples are generally characterized by spectroscopic and microscopic studies. We have used powder X-ray Diffraction (XRD) spectroscopy to determine the purity and interlayer spacing of graphene nanosheets (GNs) and highly oxidized graphene nanosheets (OGNs). Raman spectroscopy (RS) was used to determine the number of layers and the defects contained in GNs and OGNs. Elemental analysis of GNs and OGNs was carried out by Fourier transform infrared (FT-IR) spectroscopy and X-ray photoelectron spectroscopy (XPS). Transmission electron microscopy (TEM) and high resolution transmission electron microscopy (HRTEM) were used to determine the layer morphology, sheet-size and number of layers in GNs and OGNs. Single phase or surface homogeneity was characterized by scanning electron microscopy (SEM). The thermal stability of GNs and OGNs was observed via thermogravimetric analysis (TGA). The specific surface area (SSA) of GNs was measured Brunauer–Emmett–Teller (BET). The details on the company and model numbers of these tools will be explained in the experimental sections of the corresponding chapters later.

2.5 References

1. S.P. Venkateshan, Mechanical Measurements, Athena Academic and Wiley, Second Edition, 2015.
2. http://www.newport.com/Introduction-to-Solar-Radiation/411919/1033/content.aspx
3. A. Nepal, G. P. Singh, B. N. Flanders, and C. M. Sorensen, Nanotechnology **24**, 245602 (2013).
4. R. I. Soloukhin, Combust. Flame **10**, 51 (1966).
5. G. B. Kistiakowsky, H. T. Knight, and M. E. Malin, J. Chem. Phys. **20**, 884 (1952).
6. A. Williams and D. B. Smith, Chem. Rev., 70 (2), 267(1970)

Chapter 3 - One-step Synthesis of Graphene via Catalyst-free Gas-phase Hydrocarbon Detonation

(Published in 2013 Nanotechnology, 24, 245602)

Abstract: A one-step, gas-phase, catalyst-free detonation of hydrocarbon (C_2H_2) method was developed to produce gram quantities of pristine graphene nanosheets (GNs). The detonation of C_2H_2 was carried out in the presence of O_2. The molar ratios of O_2/C_2H_2 were 0.4, 0.5, 0.6, 0.7, and 0.8. The obtained GNs were analyzed by XRD, TEM, XPS and Raman spectroscopy. The GNs are crystalline with (002) peak centered at 26.05° (d = 0.341 nm). TEM shows that the GNs are stacked in two to three layers and sometimes single layers. An increase in the size of GNs (35-250 nm) along with reduction in defects (Raman I_D/I_G~ 1.33- 0.28) and specific surface area (187 to 23 m^2g^{-1}) was found with increasing O_2 content. The high temperature of the detonation, ca. 4000 K, is proposed as the cause of graphene production rather than normal soot. The method allows for the control of the number of layers, shape and size of the graphene nanosheets. The process can be scaled up for industrial production.

3.1 Introduction

Graphene is a two dimensional monolayer of sp^2 bonded carbon atoms in a hexagonal crystal structure. It has been drawing considerable interest because of its unique physical properties including excellent mechanical strength, high intrinsic carrier mobility at room temperature, and electrical and thermal conductivity comparable to the in-plane value of graphite [1–3]. These properties open gateways for the potential applications of graphene in technological areas such as nanoelectronics [4,5], sensors [6] , nanocomposites [7,8], batteries [9], supercapacitors, and hydrogen storage [10]. Pioneering work for the production of graphene was first done by the micromechanical cleavage of highly ordered pyrolytic graphite (HOPG) [10,11]. However, the low yield makes it unsustainable for large scale use. Numerous methods for preparation of graphene nanosheets have since been developed including chemical vapor deposition (CVD) [12,13], ultrasonication-assisted exfoliation of graphene oxide (GO) from graphite oxide in water [14], epitaxial growth on an electrically insulating surface [15], solution-based chemical reduction of GO [16], rapid thermal exfoliation of expanded graphite into graphene[17], high temperature heating of polymer on metal/insulator surface [18], and gas-phase plasma synthesis [19]. Notably, the CVD method has been used in a roll-to-roll production of 30-inch monolayer graphene films [20].

For the production of large quantities of graphene, the modified Hummer's method for the production of GO through chemical exfoliation of graphite to graphite oxide and then graphite oxide to GO has gained much attention due to low-cost and higher yield in comparison to other methods [21–24]. However, this method is not ideal because the GO produced suffers from some important drawbacks such as poor electrical conductivity due to the presence of epoxide, carboxyl, and hydroxyl groups on the graphene sheets [2]. Further, the reduction of GO to graphene needs insalubrious chemical reductants such as hydrazine or sodium borohydride, and high temperature heating in order to recover the graphitic structure [25]. Moreover, the reduction process cannot completely remove the many structural defects introduced by the oxidation process. A few environmentally friendly processes are available to reduce GO to graphene either by chemical or electrochemical methods, but these give low yield [26]. Thus despite the usefulness of previous graphene synthetic methods, none appear economical, eco-friendly, kilogram scale production of the material.

Here we report a novel, cost-effective and eco-friendly, one-step method that involves controlled gas-phase hydrocarbon (C_2H_2) detonation with oxygen (O_2) for the production of graphene nanosheets. Our process has several advantages such as simplicity, high productivity, economic viability, and short synthesis time (minute).This method is catalyst-free and does not generate any toxic by-products during synthesis as generated in solution phase methods [20–24].

3.2 Experimental Details

Graphene nanosheets (GNs) in the form of a powder were prepared from the catalyst-free controlled detonation of C_2H_2 gas in the presence of O_2 in a 16.6 liter cylindrical aluminum chamber. The pre-detonation molar ratios of O_2/C_2H_2 were 0.4, 0.5, 0.6, 0.7, and 0.8. For each ratio, the initial chamber pressure was 1 atmosphere. The gases had purities of 98.0 % for C_2H_2 and 99.0 % for O_2. In a typical batch, the detonation of C_2H_2 with O_2 was carried out by a controlled power supply through a spark generator ignition system. During the detonation, the hydrocarbon was first converted into free carbon atoms or ions which condensed into a nanoparticle carbon aerosols which in turn quickly aggregated and then finally formed a gel, known as a Carbon Aerosol Gel (CAG) [27]. After the denotation, the chamber was allowed to cool to 300 K. The fluffy black CAG powder was collected from the chamber (inset Fig. 3.7); we will henceforth call this material "detonation carbon". The material was homogeneous and subsequent characterization confirmed that it was one phase. The detonation pressure and temperature were measured with a data acquisition system. The same process was followed for all molar ratios. Table 3.1 shows the peak temperature and the pressure observed during detonation for different O_2:C_2H_2 molar ratios.

Table 3.1 The molar ratio O_2/C_2H_2, peak detonation temperature (T_d) and pressure (P_d) for preparation of GNs.

Molar ratio O_2/C_2H_2	T_d (K) (± 200 K)	P_d (atm) (± 1.5 atm.)
0.4	3800	13.4
0.5	3900	13.1
0.6	4200	13.8
0.7	3600	14.3
0.8	3800	14.3

These high pressures and temperatures (ca. 4000 K), which are a consequence of the exothermic detonation of the hydrocarbon and oxygen, last for about 15 milliseconds during the detonation, after which the system rapidly cools. The phase, layered structure, and the chemical compositions of detonation carbon was analyzed by XRD, TEM, Raman spectroscopy and X-ray Photoelectron spectroscopy.

3.3 Characterizations

X-ray diffraction was carried out using a Bruker D8 Advance X-ray diffractometer, Germany, with nickel filter Cu Kα radiation as the X-ray source to determine phase purity and degree of crystallization. The morphology and the size of the samples were determined with a FEI Company Nova NanoSEM 430 field emission scanning electron microscope, FESEM, at 3.5 kV and low vacuum with a TLD detector and Philips CM-100 transmission electron microscope

(TEM) with an accelerating voltage of 100 kV. For TEM measurement, the samples were prepared by inserting Cu grids in the detonation carbon powder without using any solvent. The high resolution TEM images and SAED patterns were recorded by using FEI Tecnai F20 XT Field Emission Transmission Electron Microscope with an accelerating voltage of 200 kV. BET measurements were carried out using a Nova 1000 series surface area analyzer, Quantachrome instrument. Diffuse reflectance FTIR spectra were recorded via a Cary 630 FTIR spectrophotometer, Agilent Technology, USA over a range 500-4000 cm^{-1}. The X-ray photoelectron spectroscopy (XPS) of a Perkin-Elmer PHI 5400 spectrometer with Al $K\alpha$ X-ray source (1486.6 eV) was used to obtain the chemical compositions of the samples. The spectrometer was calibrated using Au $4f_{7/2}$ at 84.0 eV and Cu $2p_{3/2}$ at 932.7 eV. The base pressure of the analysis chamber was below 10^{-9} mbar. The room temperature Raman spectra were obtained on pellets of 10 mm diameter and 2 mm thick (as shown in the inset of Fig. 3.10) with an iHR550 Raman spectrophotometer, Horiba Jobin Yvon with a HeNe laser (632.8 nm) as the excitation source.

3.4 Results and Discussions

The X-ray diffraction (XRD) patterns of the detonation carbon obtained at O_2/C_2H_2 of 0.4, 0.5, 0.6, 0.7, and 0.8 and graphite flakes (GF, obtained from Alfa Aesar for comparison) are depicted in Fig. 3.1. Fig. 3.1(a) shows seven well defined diffraction peaks that are characteristic of graphite with the most intense (002) peak centered at 26.6° (enlarged in the inset), while the (002) peak of the detonation carbon is centered at 26.05° [Fig. 3.1(b)-(f)] to imply an interplanar spacing (d) of 0.341 nm, which is larger than $d = 0.335$ nm of GF. The determined $d = 0.341$ nm for the detonation carbon is in good agreement with the XRD pattern reported for pristine GNs synthesized by other methods [28,29]. Hence, the detonation carbon resembles the graphitic (graphene) structure. In addition, the reduction in full width at half maxima (FWHM) of the (002) peak with increasing O_2/C_2H_2 ratio indicates an increased size of the crystallite and, thus, more crystalline order.

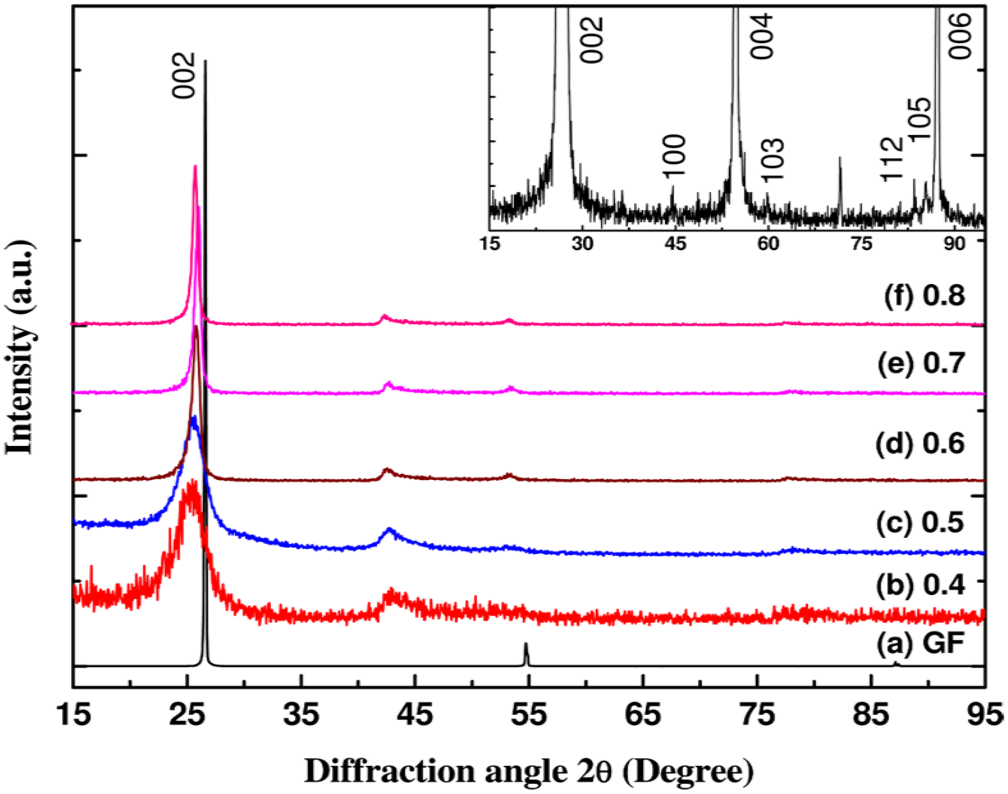

Figure 3.1 XRD patterns of (a) graphite flakes (GF), and (b through f) the detonation carbon graphene nanosheets (GNs) prepared by detonation with different O_2/C_2H_2 molar ratios. The magnified spectrum of (a) is shown in the inset.

Figure 3.2 (a-e) shows TEM images of the detonation carbon powder obtained at different O_2/C_2H_2 gas ratios. All images reveal that the layers in detonation carbon are transparent, crumpled, folded, and randomly stacked on each other. They show a laminar morphology with crumpling consistent with the structure of pristine two-dimensional graphene prepared by other methods [28–30]. This crumpling is intrinsic to graphene sheets because a thermodynamically unstable two-dimensional sheet undergoes microscopic crumpling via bending or buckling to get thermodynamically stable three-dimensional structures in localized regions [31]. In Fig. 3.2 (a, b), the detonation carbon prepared with O_2/C_2H_2 = 0.4 and 0.5, respectively, show transparent ramified fractal aggregates of GNs. These aggregates have dense regions about 35-55 nm size connected by thin, continuous, twisted, ribbon-like structures. This implies that the detonation carbon consists of GNs interlaced with one another. With increasing ratios from 0.6 to 0.8, the GNs show a distinct feature of nearly spherical shape with an increased size of about 225-250 nm [Fig. 3.2(c-e)]. The O_2/C_2H_2 ratio dependence of GNs size observed in

TEM images is consistent with the (002) peak widths in the XRD spectra [Fig. 3.1(b)-(f)]. Thus, the detonation carbon appears to be composed of GNs and will hereafter be referred to as such as well. Moreover, in the samples of lower O_2/C_2H_2, the randomly oriented GNs [Fig. 3.2(a-b)] exhibit many thin layers entangled with each other with overlapped edges, while more ordered stacking of GNs in mostly two to three layers is observed for the samples of higher O_2/C_2H_2 as seen in Fig. 3.2(c-e). The HRTEM image of the edge of the GNs in Fig. 3.2(f) shows the layer structure more closely.

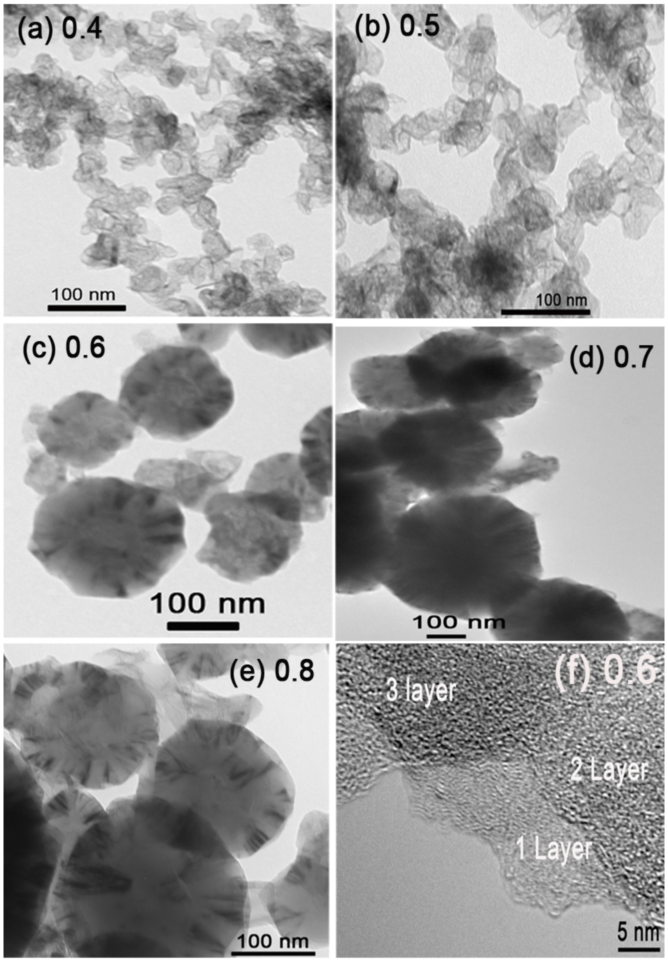

Figure 3.2 TEM images of GNs prepared by detonation of different molar ratios of O_2/C_2H_2 (a-e). (f) HRTEM image of GNs at 0.6 shows well the number of layers.

The HRTEM images of GNs (O_2/C_2H_2 = 0.6) shown in Fig. 3.2 (f) was further magnified as depicted in Fig. 3.3 to measure the distance between lattice fringe on a sheet of GNs.

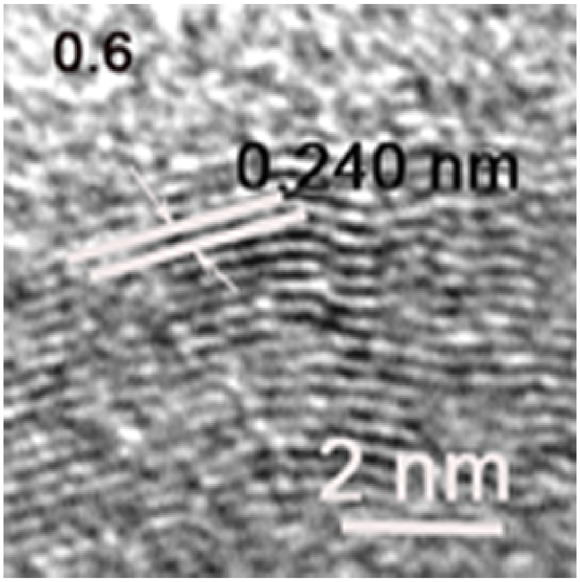

Figure 3.3 Measured distance between two consecutive lattice fringes on a GNs (O_2/C_2H_2 = 0.6) observed by HRTEM

Figure 3.3 shows the lattice fringes spacing of 0.240 nm which is in good agreement with the in-plane lattice constant of 0.246 nm for graphite [32].

High magnification TEM images and the SAED patterns of the GNs of selected regions are shown in Fig. 3.4.

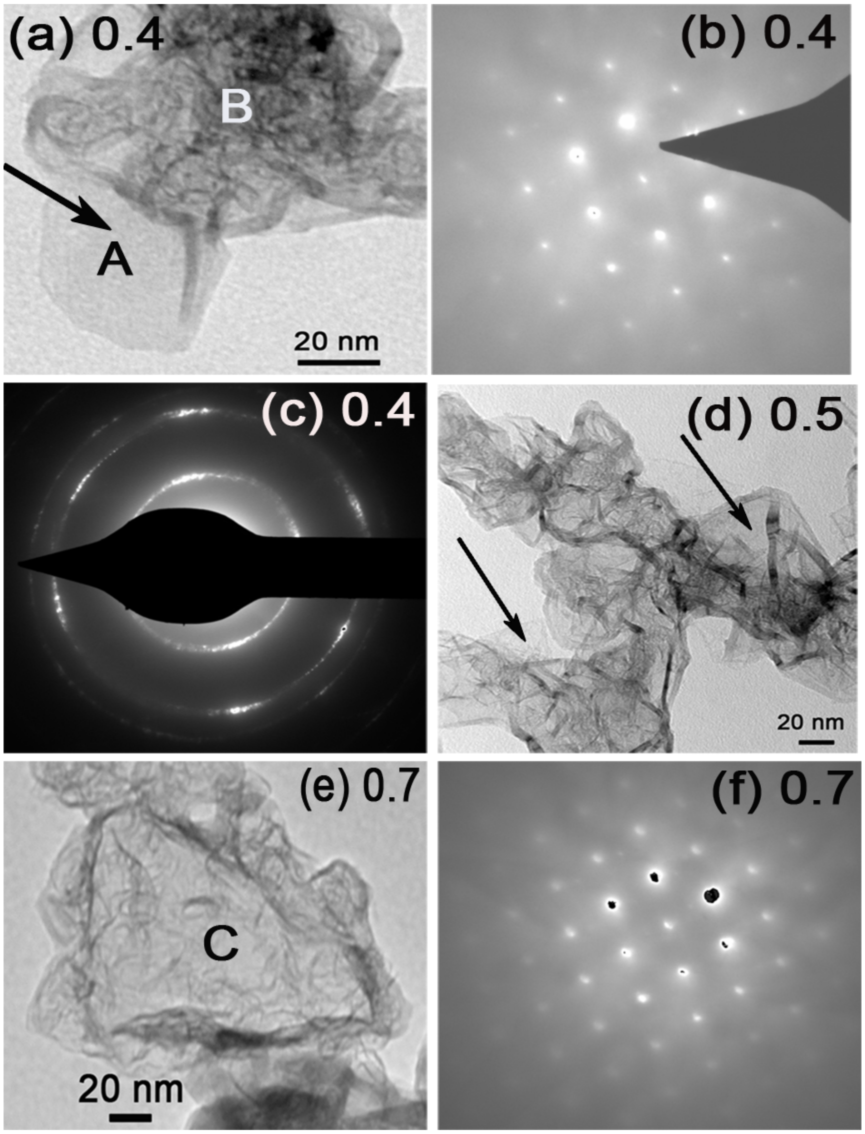

Figure 3.4 High magnification TEM images and SAED patterns of GNs prepared by detonation of different molar ratios of O_2/C_2H_2 (a-f). The SAED patterns of regions marked with 'A', 'B', and 'C' are shown in (b), (c) and (f), respectively. Arrows indicate the monolayer GNs

The transparent and featureless regions, indicated by arrows in Fig. 3.4 (a and d), are likely to be monolayer graphene which tends to scroll at the edges. The SAED patterns in Fig. 3.4(b, c and f) confirm the crystalline structure of the GNs. The diffraction patterns of the region marked with 'A' and 'C' in Fig. 3.4(a and e) show six-fold symmetry {see Fig. 3(b and f)} similar to monolayer graphene, whereas the region marked with 'B' in Fig. 3.4(a) shows misaligned diffraction spots in tiny arc shapes representing randomized six-fold symmetry as shown in Fig. 3.4(c). The misaligned spots could probably be due to crumpled local regions in GNs.

The surface homogeneity and one-phase morphology of GNs was further confirmed by FESEM image on one of the samples (0.8 O2/C2H2) shown in Fig. 3.5.

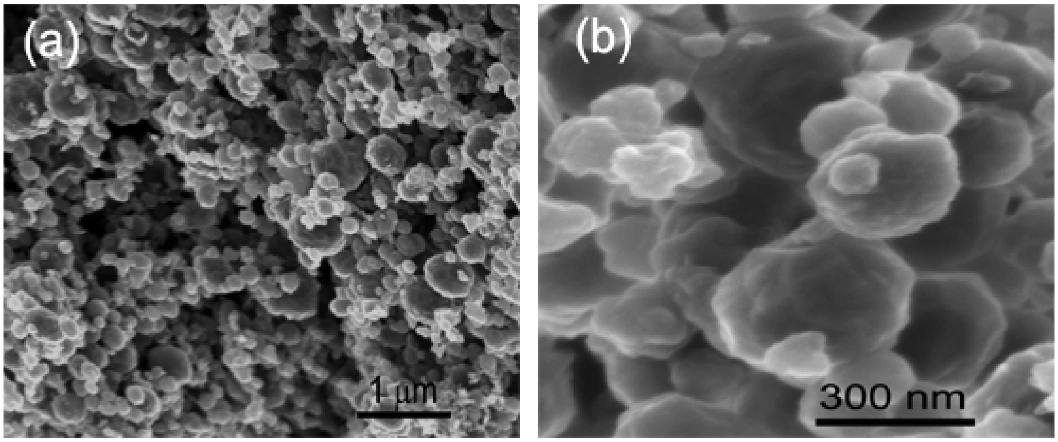

Figure 3.5 (a) FESEM image of GNs powder prepared by detonation of O_2/C_2H_2 of 0.8 and (b) magnified image of (a).

The FESEM image (Fig. 3.5) shows one-phase morphology formed by the agglomeration of roughly spherical GNs of size~ 250 nm. The morphology and size of GNs determined by FESEM here are consistent with the TEM image of GNs (3.2e).

The Brunauer-Emmett-Teller (BET) specific surface area (SSA) of the GNs measured from N_2 adsorption desorption isotherms at 77 K is shown in Fig. 3.6. The isotherms exhibit type-II pattern and type H3 hysteresis loop. The adsorption hysteresis suggests that the isotherm is a pseudo type-II pattern due to multi-layer adsorption in materials having slit-like pores or aggregates of platy particles [33]. In graphene, adsorption occurs on the surface of the graphene sheets, but due to their few layered structure, slit-like open pores exist. These open pores are responsible for the hysteresis loop observed in graphene materials [34].

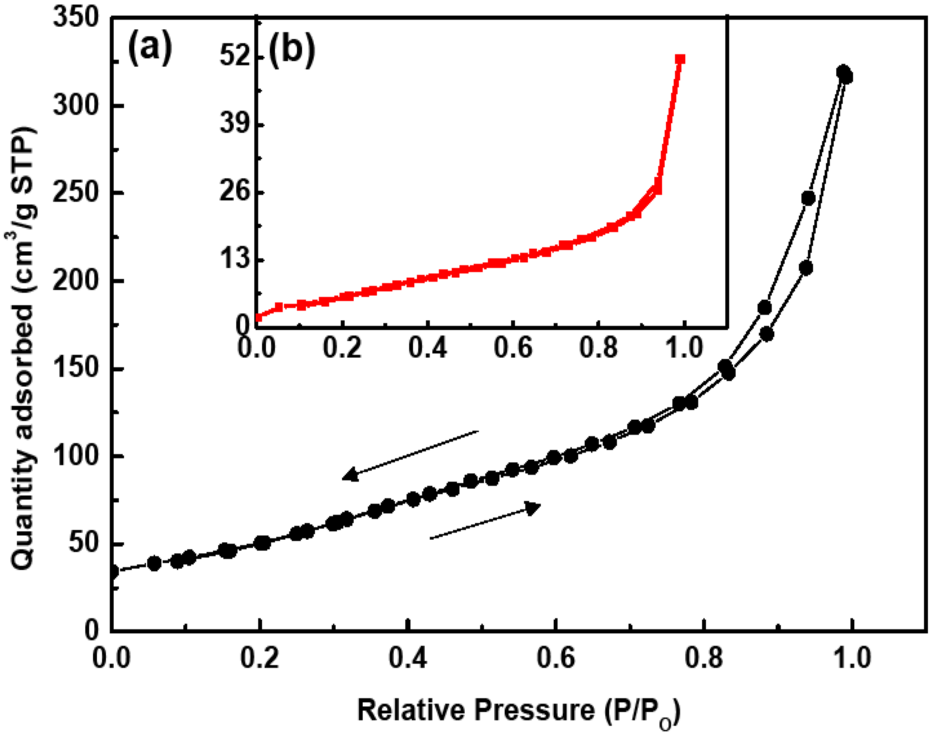

Figure 3.6 Nitrogen adsorption desorption isotherm of GNs prepared by detonation of O_2/C_2H_2 of (a) 0.4 and (b) 0.8.

From the linear region of the graph and using the BET equation, it is found that the SSA lies in between 23 to 187 m^2 g^{-1} (Fig. 3.7), which is significantly lower than the theoretical SSA of 2630 m^2 g^{-1} for individual isolated graphene sheets [35]. However, the SSA of the detonation carbon prepared at 0.4 = O_2/C_2H_2 is close to the previously reported SSA-value of 184 m^2 g^{-1} for GNs [36]. A significant finding is that the yield per detonation of the GNs is high, in the range of 38% to 66% as shown in Fig. 3.7. It is found that the mass of the GNs is decreased as the amount of O_2 is increased in the gaseous mixture.

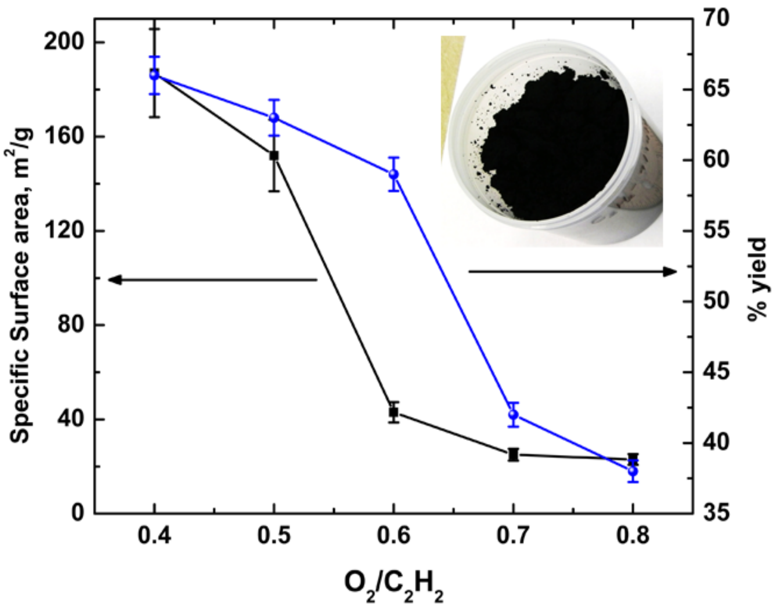

Figure 3.7 The specific surface area and yield of GNs powder. Lines are guides to the eye. Inset shows the bulk quantity ~ 7.4 g graphene powder collected after a detonation

The Drifts-FTIR measurement was performed to explore the surface functional groups present on GNs produced by detonation. Figure 3.8 displays the Drifts-FTIR spectra of detonation carbon prepared with different O_2/C_2H_2 ratio. As the production method involves C_2H_2 and O_2, one might expect some carboxyl or epoxy groups and hydrogen attached to the surface of GNs. However, the spectra (Fig. 3.8) do not show any features of functional group attached to the surface of the detonation carbon GNs, suggesting its pristine nature.

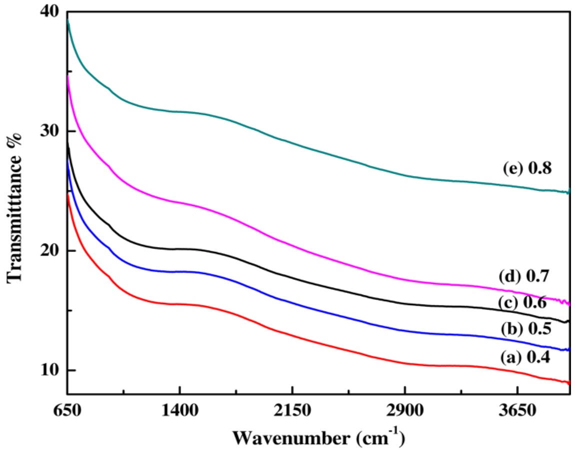

Figure 3.8 DRIFTS-FTIR spectra of GNs prepared by detonation of different molar ratios of O_2/C_2H_2

The chemical composition of GNs is further explored by X-ray Photoelectron Spectroscopy (XPS). The XPS spectra of graphene GNs obtained after detonation of O_2/C_2H_2 of 0.4 and 0.8 are presented in Fig 3.9.

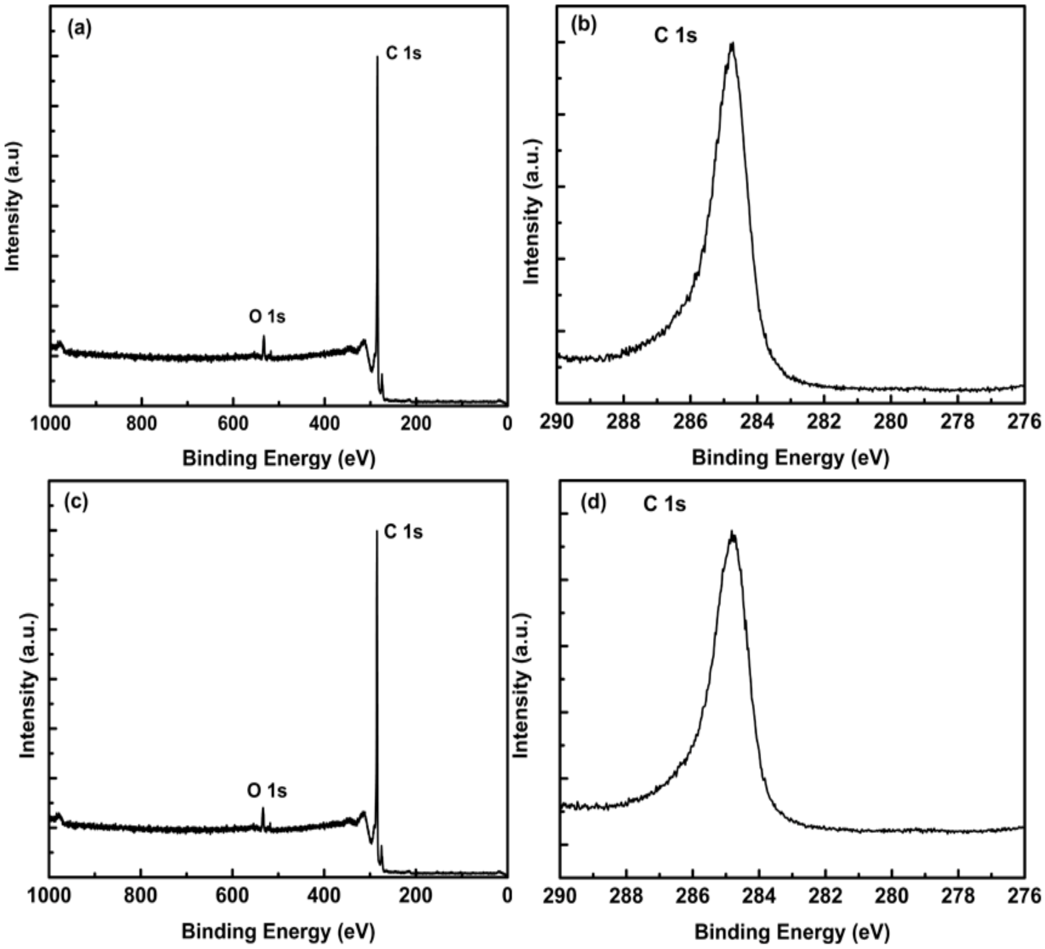

Figure 3.9 XPS spectra of graphene powder prepared after detonation of O_2/C_2H_2 of 0.4 (a) survey and (b) C 1s and O_2/C_2H_2 of 0.8 (a) survey and (b) C 1s.

The survey XPS spectrum in Fig 3.9(a, c) indicate that the graphene is very pure because the actual ratio of C to O is about 49:1. Since XPS measures the composition on the sample surface, the presence of trace oxygen in the survey spectrum can be influenced by the moisture absorption on the surface from the atmosphere [37–39]. However, the enlarged view of the C 1s spectrum presented in Fig. 3.9(b, d) show a single peak around 284.8 eV, which is associated with graphitic carbon. Moreover, the asymmetry in the peak is due to structural disorder at the edges of the *sp*^{2} network in graphene where the plane of carbon and any carbon fragments could be interacting by the surface oxygen attached during the transfer of the sample to the XPS instrument. No additional signals are observed to imply that no other functional groups are attached with the C-C system of GNs. This is consistent with the FTIR data mentioned above. These results confirm the one-phase, pristine nature of the GNs produced here.

The structure and quality of the detonation carbon GNs were analyzed by using Raman spectroscopy. Figure 3.10 shows the Raman spectra of GF and the detonation carbon GNs measured at an excitation wavelength of 632.8 nm under ambient conditions. Figure 3.10 (a) presents characteristic G- and 2D-bands of GF at 1584 and 2690 cm^{-1}, respectively, and the absence of defect (D) band indicates that GF are almost defect free. The sharp G-band at 1584 cm^{-1} corresponds to an optical E_{2g} phonon at the Brillouin Zone center of all sp^2 hybridized carbons, while the 2D-band at 2690 cm^{-1} corresponds to overtones of the D-band. This band is present even in absence of defects because it is the sum of two phonons with opposite momentum [40,41]. It is the most prominent feature for graphene in the Raman spectrum, and its position and shape can be used to distinguish between single-layer, double-layer and few-layer graphene with AB interlayer stacking [30,40].

As shown in Fig. 3. 10(b-f), the Raman spectra of the detonation carbon GNs show two new bands at 1328 and 1610 cm^{-1} along with G- and 2D-bands at 1580 and 2650 cm^{-1} .

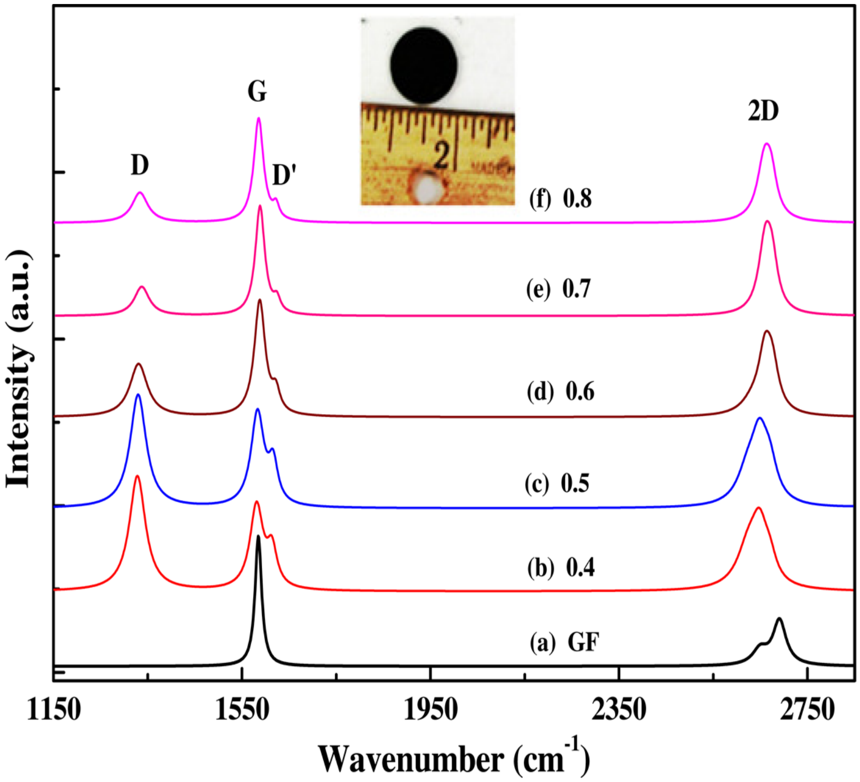

Figure 3.10 Raman spectra of GF and pristine GNs prepared by detonation of different molar ratios of O_2/C_2H_2. The inset shows the pellet form of GNs powder for Raman measurement.

The band at 1328 cm^{-1} is assigned to the D-band, which is due to an intervalley double resonance (DR) Raman process from the transverse optical modes of K-point phonons of A_{1g} symmetry in a structural defect or partially disordered structures of the sp^2 domains in GNs [40,41]. The peak at 1610 cm^{-1} is called the D′-band that occurs via an intravalley DR process in the presence of defects. Furthermore, the relative intensity of D-and G-bands is a convenient way to estimate the extent of defects and the size of in-plane sp^2 domain in the GNs [31,42]. An obvious observation is that the intensity of the D-band decreases with increasing O_2 content. The intensity ratio of the D- and G-bands (I_D/I_G) in GNs decreases from 1.33 to 0.28 for 0.4 to 0.8 O_2/C_2H_2 ratio. This indicates that partial sp^2 domains are restored at different levels, and the graphitic degree of GNs is also improved accordingly due to the reduction effect and self-repairing of the graphene layer at high O_2 content [29]. The shape of the 2D-band is O_2 content dependent as shown in Fig. 3.11.

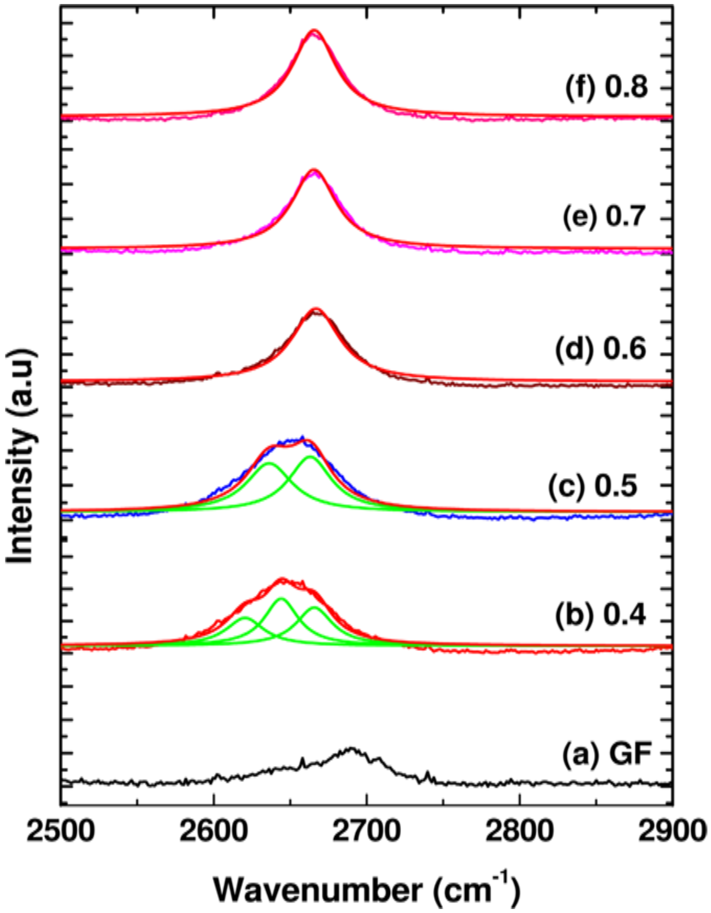

Figure 3.11 Expanded view of 2D band in Raman spectra of GF and pristine GNs prepared by detonation of different molar ratio of O_2/C_2H_2

At 0.4 O_2/C_2H_2, the 2D-band is broad to imply many layers of GNs, as is also evident from TEM images in Fig. 3.2 (a). The width gradually decreases from 65 to 43 cm^{-1} (Fig. 3.11) with increasing O_2 content, becoming sharpest for 0.8 O_2/C_2H_2. This evolution of sharpness of the 2D-band implies the transformation of GNs from many layers to two to three layers with increasing O_2 content (the width of the 2D band for monolayer graphene is 24 cm^{-1}) [43]. Hence, it can be concluded that O_2 plays a vital role for GNs quality in this particular process.

The question remains why graphene is created in this detonation process instead of normal carbonaceous soot. The mechanism of graphene production is undoubtedly as difficult to describe as the mechanism of soot formation in flames, a description which remains incomplete [44]. However, an important clue to a description might lie in Table 3.1 which shows the peak temperatures and pressures observed during detonation for the different molar ratios of O_2/C_2H_2

used. No functionality with molar ratio is observed beyond the estimated errors of the measurements. These temperatures and pressures are consistent with each other under the assumption of no change in the total moles of gas in the chamber from before detonation, at ca. 300 K and 1 atm, to the peak temperature. The peak detonation temperature of about 4000 K is roughly twice the combustion temperature of sooting hydrocarbon/air diffusion flames including C_2H_2 [45]. The "normal" soot produced in such flames consists of roughly spherical monomers (primary particles) with diameters in the range of 20 to 50 nm joined together into fractal aggregates [46,47]. The composition of these monomers is typically mostly carbon with a carbon/hydrogen ratio of $C/H \approx 8$, and the carbon is nearly amorphous being composed of many small graphitic planes [45]. In strong contrast detonation carbon is pure carbon with graphene morphology and characteristics; it is graphene. Based on our temperature measurements we propose that the key difference is the temperature. This hypothesis is supported by the observations of Choi and coworkers [48]. They used a burner arrangement in which C_2H_2 co-flowed with an annular oxyhydrogen flame. This flame produced normal soot. The flame was irradiated with a many watt CO_2 laser. Sharply above a laser power threshold the flame stopped producing normal soot and instead produced "shell-shape carbon nanoparticles" composed of graphenic-like curved layers wrapped together. Concomitant with this threshold, the flame temperature jumped from 2100 K to 3000 K. Although these observations are unexplained, their similarity to our detonation process in temperature and resulting morphologies supports our hypothesis that the high temperatures (>3000 K) during detonation is the fundamental cause of the graphenic nature of the carbon produced. Given these observations, we further hypothesize that high temperature, such as 4000 K, completely decomposes the hydrocarbon precursor to yield carbon atoms or ions which then rapidly combine after the high temperature phase to form graphene. This is very different than the current view of normal soot formation in a flame which describes soot formation as a chemical process involving molecular polymerization up a chain of polyaromatic hydrocarbons followed by dehydrogenation to soot [44]. Finally, if this hypothesis is true, detonation of other hydrocarbons should yield graphene materials as well; a proposition we will soon pursue.

3.5 Conclusions

In summary, a simple, quick, one-step, eco-friendly, high-yield method for the gram scale production of graphene nanosheets has been developed. The method involves the controlled detonation of C_2H_2 in presence of O_2. The high temperature of the detonation, ca. 4000 K, is proposed as the cause of graphene production rather than normal soot. This method is green and does not result in contamination of the graphene product. Simple modification of our lab-scale apparatus could produce 300 grams/hour. Thus, with scale up, this method can produce graphene nanosheets in the large quantities required for industrial application.

3.6 References

1. M. I. Katsnelson, Mater. Today 10, 20 (2007).

2. R. Ruoff, Nat. Nanotechnol. 3, 10 (2008).

3. A. K. Geim, Science 324, 1530 (2009).

4. Y.-M. Lin, K. A. Jenkins, A. Valdes-Garcia, J. P. Small, D. B. Farmer, and P. Avouris, Nano Lett. 9, 422 (2009).

5. F. Schedin, A. K. Geim, S. V. Morozov, E. W. Hill, P. Blake, M. I. Katsnelson, and K. S. Novoselov, Nat. Mater. 6, 652 (2007).

6. N. Mohanty and V. Berry, Nano Lett. 8, 4469 (2008).

7. S. Stankovich, D. A. Dikin, G. H. B. Dommett, K. M. Kohlhaas, E. J. Zimney, E. A. Stach, R. D. Piner, S. T. Nguyen, and R. S. Ruoff, Nature 442, 282 (2006).

8. S. Watcharotone, D. A. Dikin, S. Stankovich, R. Piner, I. Jung, G. H. B. Dommett, G. Evmenenko, S.-E. Wu, S.-F. Chen, C.-P. Liu, S. T. Nguyen, and R. S. Ruoff, Nano Lett. 7, 1888 (2007).

9. T. Takamura, K. Endo, L. Fu, Y. Wu, K. J. Lee, and T. Matsumoto, Electrochimica Acta 53, 1055 (2007).

10. A. K. Geim and K. S. Novoselov, Nat. Mater. 6, 183 (2007).

11. K. S. Novoselov, D. Jiang, F. Schedin, T. J. Booth, V. V. Khotkevich, S. V. Morozov, and A. K. Geim, Proc. Natl. Acad. Sci. U. S. A. 102, 10451 (2005).

12. A. Charrier, A. Coati, T. Argunova, F. Thibaudau, Y. Garreau, R. Pinchaux, I. Forbeaux, J.-M. Debever, M. Sauvage-Simkin, and J.-M. Themlin, J. Appl. Phys. 92, 2479 (2002).

13. C. Berger, Z. Song, X. Li, X. Wu, N. Brown, C. Naud, D. Mayou, T. Li, J. Hass, A. N. Marchenkov, E. H. Conrad, P. N. First, and W. A. de Heer, Science 312, 1191 (2006).

14. Y. Hernandez, V. Nicolosi, M. Lotya, F. M. Blighe, Z. Sun, S. De, I. T. McGovern, B. Holland, M. Byrne, Y. K. Gun'Ko, J. J. Boland, P. Niraj, G. Duesberg, S. Krishnamurthy, R. Goodhue, J. Hutchison, V. Scardaci, A. C. Ferrari, and J. N. Coleman, Nat. Nanotechnol. 3, 563 (2008).

15. G. M. Rutter, J. N. Crain, N. P. Guisinger, T. Li, P. N. First, and J. A. Stroscio, Science 317, 219 (2007).

16. C. Zhu, S. Guo, Y. Fang, and S. Dong, ACS Nano 4, 2429 (2010).

17. G. Chen, W. Weng, D. Wu, and C. Wu, Eur. Polym. J. 39, 2329 (2003).

18. G. Chen, C. Wu, W. Weng, D. Wu, and W. Yan, Polymer 44, 1781 (2003).

19. A. Dato, V. Radmilovic, Z. Lee, J. Phillips, and M. Frenklach, Nano Lett. 8, 2012 (2008).

20. S. Bae, H. Kim, Y. Lee, X. Xu, J.-S. Park, Y. Zheng, J. Balakrishnan, T. Lei, H. Ri Kim, Y. I. Song, Y.-J. Kim, K. S. Kim, B. Özyilmaz, J.-H. Ahn, B. H. Hong, and S. Iijima, Nat. Nanotechnol. 5, 574 (2010).

21. S. Park and R. S. Ruoff, Nat. Nanotechnol. 4, 217 (2009).

22. S. Park, J. An, I. Jung, R. D. Piner, S. J. An, X. Li, A. Velamakanni, and R. S. Ruoff, Nano Lett. 9, 1593 (2009).

23. C. Gómez-Navarro, R. T. Weitz, A. M. Bittner, M. Scolari, A. Mews, M. Burghard, and K. Kern, Nano Lett. 9, 2206 (2009).

24. A. A. Green and M. C. Hersam, Nano Lett. 9, 4031 (2009).

25. S. Stankovich, D. A. Dikin, R. D. Piner, K. A. Kohlhaas, A. Kleinhammes, Y. Jia, Y. Wu, S. T. Nguyen, and R. S. Ruoff, Carbon 45, 1558 (2007).

26. H.-L. Guo, X.-F. Wang, Q.-Y. Qian, F.-B. Wang, and X.-H. Xia, ACS Nano 3, 2653 (2009).

27. R. Dhaubhadel, C. S. Gerving, A. Chakrabarti, and C. M. Sorensen, Aerosol Sci. Technol. 41, 804 (2007).

28. G. Wang, J. Yang, J. Park, X. Gou, B. Wang, H. Liu, and J. Yao, J. Phys. Chem. C 112, 8192 (2008).

29. Z.-H. Sheng, L. Shao, J.-J. Chen, W.-J. Bao, F.-B. Wang, and X.-H. Xia, ACS Nano 5, 4350 (2011).

30. A. Kaniyoor and S. Ramaprabhu, J. Appl. Phys. 109, 124308 (2011).

31. J. C. Meyer, A. K. Geim, M. I. Katsnelson, K. S. Novoselov, T. J. Booth, and S. Roth, Nature 446, 60 (2007).

32. Y. Baskin and L. Meyer, Phys. Rev. 100, 544 (1955).

33. K. S. W. Sing, J. Porous Mater. 2, 5 (1995).

34. W. Lv, D.-M. Tang, Y.-B. He, C.-H. You, Z.-Q. Shi, X.-C. Chen, C.-M. Chen, P.-X. Hou, C. Liu, and Q.-H. Yang, ACS Nano 3, 3730 (2009).

35. M. D. Stoller, S. Park, Y. Zhu, J. An, and R. S. Ruoff, Nano Lett. 8, 3498 (2008).

36. D. Pan, S. Wang, B. Zhao, M. Wu, H. Zhang, Y. Wang, and Z. Jiao, Chem. Mater. 21, 3136 (2009).

37. M. Choucair, P. Thordarson, and J. A. Stride, Nat. Nanotechnol. 4, 30 (2009).

38. S. C. Tsang, V. Caps, I. Paraskevas, D. Chadwick, and D. Thompsett, Angew. Chem. Int. Ed. 43, 5645 (2004).

39. H. C. Schniepp, J.-L. Li, M. J. McAllister, H. Sai, M. Herrera-Alonso, D. H. Adamson, R. K. Prud'homme, R. Car, D. A. Saville, and I. A. Aksay, J. Phys. Chem. B 110, 8535 (2006).

40. A. C. Ferrari, J. C. Meyer, V. Scardaci, C. Casiraghi, M. Lazzeri, F. Mauri, S. Piscanec, D. Jiang, K. S. Novoselov, S. Roth, and A. K. Geim, Phys. Rev. Lett. 97, 187401 (2006).

41. D. C. Elias, R. R. Nair, T. M. G. Mohiuddin, S. V. Morozov, P. Blake, M. P. Halsall, A. C. Ferrari, D. W. Boukhvalov, M. I. Katsnelson, A. K. Geim, and K. S. Novoselov, Science 323, 610 (2009).

42. Z. Luo, T. Yu, K. Kim, Z. Ni, Y. You, S. Lim, Z. Shen, S. Wang, and J. Lin, ACS Nano 3, 1781 (2009).

43. L. M. Malard, M. A. Pimenta, G. Dresselhaus, and M. S. Dresselhaus, Phys. Rep. 473, 51 (2009).

44. M. Frenklach, Phys. Chem. Chem. Phys. 4, 2028 (2002).

45.A.G. Gaydon and H. G. Wolfhard Flames: Therir Structure, Radiation and Temperature 4th edn (London:Chapman and Hall) (1979)

46. R. Dhaubhadel, F. Pierce, A. Chakrabarti, and C. M. Sorensen, Phys. Rev. E 73, 011404 (2006).

47. C. M. Sorensen and G. D. Feke, Aerosol Sci. Technol. 25, 328 (1996).

48. M. Choi, I. S. Altman, Y.-J. Kim, P. V. Pikhitsa, S. Lee, G.-S. Park, T. Jeong, and J.-B. Yoo, Adv. Mater. 16, 1721 (2004).

Chapter 4 - Synthesis of Graphene Nanosheets via Controlled Hydrocarbon Detonation: Role of Oxidizer and Hydrocarbon

4.1 Introduction

Two dimensional single layers of graphene (SLG) possess unique electrical, mechanical and thermal properties. These properties, when exploited fully, will lead to applications of graphene in nanoelectronics [1,2], batteries [3], supercapacitors [4], sensors [5,6], hydrogen storage [7], photovoltaics [8] and composite materials [9,10]. However, there has been a real challenge to produce large quantities of SLG, mainly because the layers aggregate quickly due to π-π stacking and van der Waals attraction between the layers. Numerous graphene synthesis techniques like mechanical exfoliation of graphite [11] chemical exfoliation of graphite [12], chemical vapor deposition [13,14], epitaxial growth of graphene on substrates [15] and detonation of hydrocarbon [16] have been attempted.

Most of the methods of graphene synthesis reported so far suffer from one or the other disadvantages like low yield, high cost, long time of synthesis and unhealthy byproducts. However, the hydrocarbon detonation technique to produce graphene is a catalyst-free, one step, high yielding, eco-friendly, cheap, and scalable method of graphene production. Also, because the detonation provides energy, the method does not require an energy source. As of now, detonation of only one hydrocarbon, C_2H_2, with oxygen, O_2 to produce graphene nanosheets with few to multilayer stacks have been reported [16]. Thus, it is worthwhile to explore other hydrocarbons and oxidizers that can be used to produce graphene. In this work, we report the effect of the change of oxidizer from O_2 to nitrous oxide (N_2O) on the graphene nanosheets' quality and characteristics of carbon produced by the detonation of ethylene (C_2H_4), propane (C_3H_8) and methane (CH_4) to determine their viability as precursor hydrocarbons to produce GNs by the detonation technique.

4.2 Experiments

4.2.1 Synthesis of Detonation Carbon

Carbon samples were prepared by detonating hydrocarbons with oxidizers in a 16.6 liter aluminum chamber. For each detonation, the initial pressure of mixture of hydrocarbon and oxidizer filled into the chamber was 1 atmosphere. A typical detonation was carried out by a controlled power supply through a spark generator ignition system. The peak detonation temperature and pressure were measured by a two-color pyrometer and a pressure probe installed into the chamber. The details of the experimental set up is mentioned in reference [16]. C_2H_2 (98.0% purity) was detonated with N_2O (99.0% purity) at $C_2H_2/N_2O = 0.8$, 1.0 and 1.2 to see whether a change in oxidizer, from O_2 to N_2O, brings any change in the quality of GNs produced. C_2H_2 (98.0% purity), C_2H_4 (99.5 % purity), C_3H_8 (99.0 % purity) and CH_4 (98.0% purity) were detonated with O_2 near their upper explosion limit (UEL) to produce carbon products. The samples were characterized by XRD, TEM, FTIR and Raman spectroscopy.

4.2.2 Characterization of the samples

X-ray diffraction was carried out using a Bruker D8 Advance X-ray diffractometer, Germany, with nickel filter Cu Kα radiation as the X-ray source to determine phase purity and degree of crystallization. The morphology and the size of the samples were determined by Philips CM-100 transmission electron microscope (TEM) with an accelerating voltage of 100 kV. For TEM measurement, the samples were prepared by inserting Cu grids in the detonation carbon powder without using any solvent. Diffuse reflectance FTIR spectra were recorded via a Cary 630 FTIR spectrophotometer, Agilent Technology, USA. The room temperature Raman spectra were obtained on pellets of 10 mm diameter and 2 mm thick with an iHR550 Raman spectrophotometer, Horiba Jobin Yvon with a HeNe laser (632.8 nm) as the excitation source.

4.3 Results and Discussions

4.3.1 Effect of changing oxidizer from O_2 to N_2O

C_2H_2 was detonated with N_2O to see whether changing the oxidizer from O_2 to N_2O changes the graphene quality. The molar ratios, $N_2O/C_2H_2 =$ 0.8, 1, and 1.2 were chosen for detonation. The peak detonation temperature, pressure, yields, and specific surface area (SSA) of the carbon products is given in the Table 4.1.

Table 4.1 Detonation temperature, pressure, yield and SSA of C formed by the detonation of acetylene with nitrous oxide at N2O/C2H2~0.8, 1, and 1.2

Molar Ratio N_2O/ C_2H_2	Detonation Temperature T, K ± 200 K	Detonation pressure P, atm ± 1.5 atm	% Yield	S.S. Area, m^2/g
0.8	3500	12.1	63%	190
1	3400	13.0	54%	124
1.2	3500	13.6	43%	71

For detonations of C_2H_2 with N_2O in ratios shown in the Table 4.1, the detonation temperature and pressure are approximately 3500 K and 13 atmospheres, respectively. However, the average temperature of detonation has been decreased by ~ 500 K in relation to detonation of C_2H_2 with O_2 as reported earlier [16]. This decrease in peak detonation temperature appears to be due to the change in the oxidizer from O_2 to N_2O. The yield and SSA of the carbon produced decreases with increasing nitrous oxide content. These trends are consistent with those observed for O_2/C_2H_2 detonations [16]. The carbon products from the detonation of C_2H_2 with N_2O were characterized by XRD, Raman Spectroscopy, TEM and FTIR. The observations are shown in Fig. 4.1

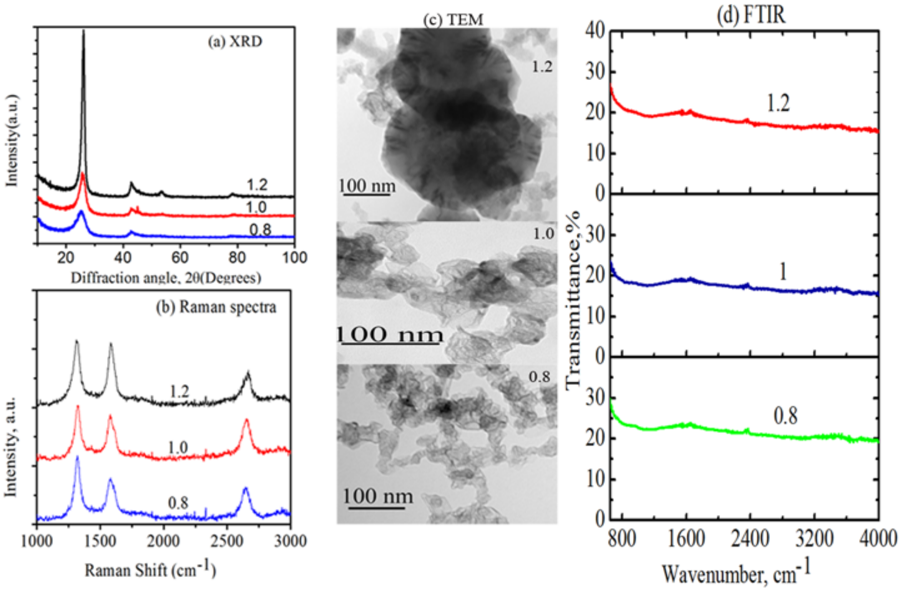

Figure 4.1 Characterization of carbon from detonating at N_2O/C_2H_2~ 0.8, 1.0 and 1.2 (a) XRD, (b)Raman Spectra (c) TEM and (d) FTIR

The x-ray diffraction (XRD) patterns of the carbon obtained by detonating acetylene with nitrous oxide at ratios N_2O/C_2H_2~ 0.8, 1.0 and 1.2 are shown in Fig. 4.1a. The most intense (002) peak is centered at 2θ ~26.2° and the interplanar distance (d) determined from this is 0.340 nm. This (d) value is more than that for graphite (d= 0.335 nm) [16] and is in good agreement with the reported value of d for graphene nanosheets (GNs) synthesized by other methods [17,18]. Therefore, the detonation of C_2H_2 with N_2O gives GNs as well as the detonation of the same with O_2. Also, the decreasing full width at half maxima (FWHM) of (002) peak with increasing N_2O/C_2H_2 ratio indicates increased crystallite size and improved crystalline order. This effect of increasing ratio of oxidizer to precursor hydrocarbon on the quality of GNs crystal structure is similar to that observed in GNs produced by detonating the same hydrocarbon with O_2 [16].

Figure 4.1(b) represents the Raman spectra of carbon obtained by detonation at N_2O/C_2H_2 ~ 0.8, 1.0 and 1.2. The most prominent peaks are at 1325 cm^{-1}, 1585 cm^{-1} and 2668 cm^{-1} corresponding to D, G, and 2D-bands. The positions of these peaks are consistent with those for GNs reported in previous work [16,19,20]. The D-band is indicative of defects/disorders and the G-band represents in-plane vibration of sp^2 hybridized carbon atoms in GNs [21]. The 2D-band is the second order of the D-band, sometimes referred to as an overtone of the D-band. Since the 2D- band is the sum of two phonons with opposite momentum, it can be present even if the sample is defect-free [19]. Figure 1(b) shows that the ratio of the intensity of D-band to the intensity of G-band, I_D/I_G, decreases from 1.50 for N_2O/C_2H_2~0.8 to 1.01 for N_2O/C_2H_2~ 1.2. This decreasing I_D/I_G with increasing oxidizer content indicates that sp^2 domains are restored and the graphitic degree of GNs is also improved accordingly due to the reduction effect and self-repairing of the graphene layer at high N_2O content [16,22]. Moreover, FWHM of 2D-band decreases from 55 cm^{-1} for N_2O/C_2H_2~ 0.8 to 43 cm^{-1} for N_2O/C_2H_2~ 1.2 which, in turn, indicates that mostly multilayer GNs at N_2O/C_2H_2~ 0.8 content has been transformed into 2-3 layer stacks for N_2O/C_2H_2~ 1.2. Hence, the content of N_2O plays an important role for the quality of GNs produced in detonation. A similar effect of oxidizer was observed while oxygen was used in the detonation [16].

The layer morphology of GNs produced is depicted by TEM images in Fig. 4.1(c). The thin layered GNs interlace into dense patches forming multilayer graphene in the lower N_2O content while the stacking of GNs is more organized with 2-3 layers in a nearly circular patch in case of $N_2O/C_2H_2\sim 1.2$. This improved stacking order of GNs in higher N_2O content is consistent with the results obtained from Raman spectra. The size of GNs varies from ~50 nm for $N_2O/C_2H_2\sim 0.8$ to ~250 nm for $N_2O/C_2H_2\sim 1.2$ and this is consistent with the increasing crystallite size of GNs observed in XRD.

The Drifts-FTIR was used to determine the functional groups attached on the GNs. Figure 1(d) presents the Drifts-FTIR spectra of GNs produced by detonation at $N_2O/C_2H_2\sim 0.8$, 1, and 1.2. Since all spectra in Fig. 4.1(d) are almost featureless, it can be concluded that no functional groups are attached on the surface of GNs and hence they are pristine in nature.

In conclusion, the peak *in situ* temperature during the detonations of C_2H_2 with N_2O was ~3500 K, and it is well above the proposed threshold temperature (~3000 K) to produce shell-shaped carbon nanoparticles comprised of graphenic-like curved layers by a "laser-burn" on C_2H_2 flames [23]. Thus, the detonation temperature > 3000 K, despite the change in oxidizer from O_2 to N_2O, might be the reason of formation of pristine GNs instead of normal carbon soot. The two important effects of increasing the N_2O content are increasing GNs lateral size and decreasing defects in crystal structure of GNs. These effects are similar to the ones observed while increasing the O_2 content during the detonation of C_2H_2 to produce GNs. The maximum size (~ 250 nm) and SSA (~ 190 m^2/g) of GNs produced are very close to those of GNs produced by detonating C_2H_2 with O_2. Therefore, N_2O can be considered as an oxidizer alternative to O_2 while producing the GNs from hydrocarbon detonation method with out deteriorating the quality of the product.

4.3.2 Role of Hydrocarbons-composition

Gas phase hydrocarbon detonation with oxygen will mainly yield carbon (C), carbon dioxide (CO_2), carbon monoxide (CO), and water (H_2O). Here we want to characterize and compare the carbon formed from the detonation of some aliphatic hydrocarbons: acetylene (H-C≡C-H), ethylene ($H_2C{=}CH_2$), propane ($H_3C\text{-}CH_2\text{-}CH_3$), and methane ($CH_4$) which have triple, double, single, and no bond between carbon-carbon atoms, respectively. Each of the hydrocarbons have unique upper explosion limit (UEL) and lower explosion limits (LEL) in an oxygen environment (Table 4.2). Despite the different UEL and LEL for each hydrocarbon, C produced by the detonations at hydrocarbon rich conditions, near UEL, were characterized to maintain the consistency in the condition of formation and to assure that there is C formed in the detonation. Table 4.2 presents the ratio of oxygen to hydrocarbon chosen for experiment, detonation temperature, pressure and yield in percentage.

Table 4.2 Upper explosion limit (UEL), lower explosion limit (LEL) of hydrocarbons in oxygen environment, ratio of oxygen to hydrocarbon used for detonation, detonation temperature, T_D , detonation pressure, P_D, % yield of carbon from the detonation.

Hydrocarbon	LEL in O_2 %	UEL in O_2 %	Detonated ratio, $\frac{O_2}{hydrocarbon}$	T_D, K ± 200 K	P_D, atm. ± 1.5 atm	% yield of carbon
H-C≡C-H	11	100	0.3 (~77 % fuel)	3500	11.3	71%
H_2C=CH_2	12	73	1.0 (~50 % fuel)	3700	13.0	25%
H_3C-CH_2-CH_3	9	33	2.0 (~ 33 % fuel)	3700	11.6	11%
CH_4	20	46	1.5(40% fuel) 1.2 (45% fuel)	- -	- -	0 0

The temperatures and pressures of detonations presented in Table 2 are $T_D \geq 3500$ K and $P_D \geq 11.3$ atmospheres, respectively. The detonation *in situ* environment is thus very hot. On the other hand, the diversity in the hydrocarbons listed in Table 2 lies in the carbon-carbon bonding (from none to triple) and their molar ratio used to detonate in O_2 environment. So, it is obvious that they do not produce the same quantity of carbon during detonation mentioned in the Table 4.2, and it is hard to determine the best hydrocarbon in terms of the yields. However, a qualitative observation is that the yield of carbon from a detonation carried out in a hydrocarbon rich environment is higher (71% yield for O_2/C_2H_2 = 77% if acetylene is detonated with O_2) than that from a detonation carried out in lower concentration of hydrocarbon (11% yield from detonation of O_2/C_3H_8 = 33% for C_3H_8 with O_2). Also, detonation of CH_4 with oxygen even near the UEL (O_2/CH_4 = 40% and 45%) could not yield carbon. Since the inside of the chamber was wet after these detonations, we can conclude that the detonation of CH_4 may yield gaseous products (CO or/and CO_2) and water but no solid carbon. The carbon products formed in the detonations of the rest of the hydrocarbons will be characterized by TEM and Raman spectroscopy to explore the layer morphology and microstructure to determine whether they are graphene or amorphous normal carbon soot.

The layer morphology and microstructure of carbon formed by detonating hydrocarbons with O_2 is given in corresponding TEM images and Raman spectrum in Fig. 4.2.

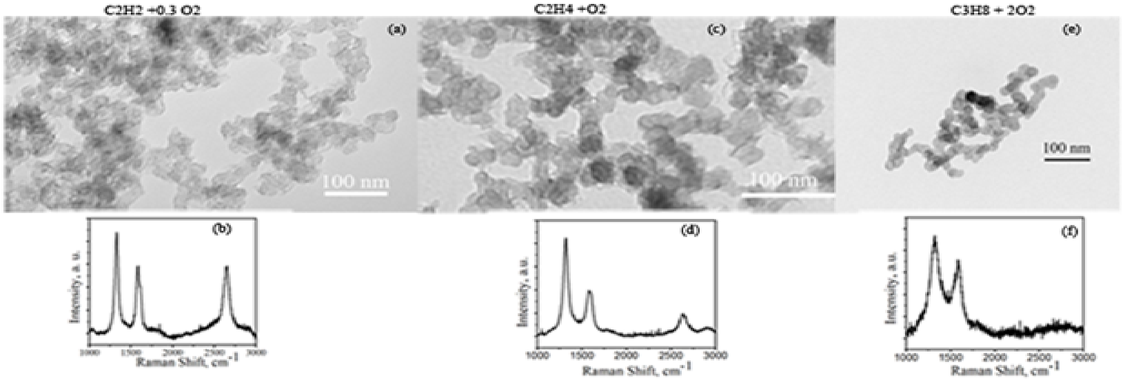

Figure 4.2 TEM image and Raman spectrum of carbon formed by detonation of O_2/C_2H_2 =0.3 (a) and (b), O_2/C_2H_4 =1.0 (c) and (d), and O_2/C_3H_8 =2.0 (e) and (f), respectively

The carbon samples formed by detonating C_2H_2 and C_2H_4, Fig. 4.2(a) and (c), consist of transparent ramified fractal aggregates of GNs. The aggregates have dense/dark regions of 35-55 nm size connected by thin, continuous, twisted and folded ribbon-like structures. Thus, these samples contain overlapped and entangled layers interlaced with one another to form the dense regions. This continuous layer morphology of carbons observed in TEM images confirms that their basic structural units are in the form of 2D sheets as for GNs. On the other hand, the TEM of carbon from detonation of C_3H_8, Fig.4. 2(e), shows aggregation of spheroid particles (size 20-30 nm) with random orientation and lacks layer morphology. So, these randomly oriented spheroid basic structural units in TEM show that the carbon formed from detonating C_3H_8 is more likely to be amorphous carbon rather than GNs.

The D-band at ~1330 cm^{-1}, the G-band at ~1580 cm^{-1} and 2D-band at~ 2660 cm^{-1} in a carbon sample are fingerprints to recognize GNs as discussed in earlier section. Moreover, the D- and G-band will be distinct in GNs. The carbon soot is considered as highly disordered graphitic structures and the D- and G- bands in the Raman spectrum generally appear as broad and overlapping peaks. Also, the normal carbon soot will have a very broad 2D-band [23,24]. The D- ,G- and 2D-bands in the Raman spectra of carbons from detonation of C_2H_2 and C_2H_4, Fig. 4.

2(b) and (d), indicate that they are GNs. The D- and G- peaks are distinct as well. However, for the carbon from C_3H_8, Fig. 4.2(f), the D-and G-peaks are overlapped and broader; the 2D- band is broad, and resembles to the carbon soot. These inferences from the Raman spectra are consistent with the TEM images of corresponding carbon samples. Therefore, the products from detonation of C_2H_2 and C_2H_4 are GNs whereas that from detonation of C_3H_8 is graphitic amorphous carbon soot.

In summary, we observed that the detonation of C_2H_2 and C_2H_4 yield GNs whereas C_3H_8 detonation yields carbon soot. Now the question comes across that why the detonation of C_3H_8 , despite the detonation temperature > 3000 K, does not yield graphene and, instead, disordered graphitic carbon soot. The answer might be in the fact that the properties of the carbonaceous compounds formed by the pyrolysis of the organic materials depend not only on the temperature, but also, to some extent, on the nature of the starting material [25]. The "non-graphitizing" carbons are those which cannot be graphitized while heated even up to >3000 K. This class of carbons has a strong system of cross-linking uniting the crystallites and hence these crystallites are randomly oriented in a rigid and finely porous mass. The small graphitic planes in such crystallites do not grow even if they are heated up beyond 3000 K [25]. The cross-linking between the crystallites of "graphitizing carbons", on the other hand, is weak and do not hinder the growth of the crystallite while heated. This class of carbon materials shows graphitic layer structure when heated up to 3000 K [25].

The detonation process first produces carbon aerosols into the chamber. These non-coalescing carbon particles start forming the carbon aerosol gels (CAG) shortly after the detonation [26]. The results above imply that the mechanism of crystallite growth in CAG in the high *in situ* detonation temperature depends on the precursor hydrocarbon as well. CAG formed during C_3H_8 detonation is likely to be non-graphitizing carbon and remains disordered graphitic carbon soot even at temperatures > 3000 K. The CAG produced by the detonation of C_2H_2 and C_2H_4, on the other hand, are graphitizing carbon and grow into GNs at higher temperatures. We are going to characterize these samples with other more precise tools before coming to a concrete statement on the relation between C/H of the hydrocarbons and degree of graphitization. However, from our observations so far, we speculate that the hydrocarbons with $C/H \geq 0.5$ may produce graphene whereas hydrocarbons with $C/H \leq 0.375$ will produce either normal carbon soot or no solid carbon while detonated with oxygen.

4.4 Conclusion

The hydrocarbon detonation technique for the production of GNs was tested by changing the oxidizer from O_2 to N_2O to detonate C_2H_2. N_2O was confirmed as an alternative to O_2 as an oxidizer to produce GNs from C_2H_2. The quality of GNs produced was almost the same with the both oxidizers when detonated with C_2H_2. We also find that C_2H_2 and C_2H_4 can be used to produce GNs whereas C_3H_8 and CH_4 are not suitable to be used to produce GNs from the detonation technique.

4.5 References

1. Y.-M. Lin, K. A. Jenkins, A. Valdes-Garcia, J. P. Small, D. B. Farmer, and P. Avouris, Nano Lett. **9**, 422 (2009).

2. F. Schedin, A. K. Geim, S. V. Morozov, E. W. Hill, P. Blake, M. I. Katsnelson, and K. S. Novoselov, Nat. Mater. **6**, 652 (2007).

3. T. Takamura, K. Endo, L. Fu, Y. Wu, K. J. Lee, and T. Matsumoto, Electrochimica Acta **53**, 1055 (2007).

4. Y. Zhu, S. Murali, M. D. Stoller, K. J. Ganesh, W. Cai, P. J. Ferreira, A. Pirkle, R. M. Wallace, K. A. Cychosz, M. Thommes, D. Su, E. A. Stach, and R. S. Ruoff, Science **332**, 1537 (2011).

5. M. Pumera, A. Ambrosi, A. Bonanni, E. L. K. Chng, and H. L. Poh, TrAC Trends Anal. Chem. **29**, 954 (2010).

6. M. Zhou, Y. Zhai, and S. Dong, Anal. Chem. **81**, 5603 (2009).

7. A. K. Geim and K. S. Novoselov, Nat. Mater. **6**, 183 (2007).

8. L. Gomez De Arco, Y. Zhang, C. W. Schlenker, K. Ryu, M. E. Thompson, and C. Zhou, ACS Nano **4**, 2865 (2010).

9. S. Stankovich, D. A. Dikin, G. H. B. Dommett, K. M. Kohlhaas, E. J. Zimney, E. A. Stach, R. D. Piner, S. T. Nguyen, and R. S. Ruoff, Nature **442**, 282 (2006).

10. S. Watcharotone, D. A. Dikin, S. Stankovich, R. Piner, I. Jung, G. H. B. Dommett, G. Evmenenko, S.-E. Wu, S.-F. Chen, C.-P. Liu, S. T. Nguyen, and R. S. Ruoff, Nano Lett. **7**, 1888 (2007).

11. K. S. Novoselov, A. K. Geim, S. V. Morozov, D. Jiang, Y. Zhang, S. V. Dubonos, I. V. Grigorieva, and A. A. Firsov, Science **306**, 666 (2004).

12. S. Stankovich, D. A. Dikin, R. D. Piner, K. A. Kohlhaas, A. Kleinhammes, Y. Jia, Y. Wu, S. T. Nguyen, and R. S. Ruoff, Carbon **45**, 1558 (2007).

13. A. Charrier, A. Coati, T. Argunova, F. Thibaudau, Y. Garreau, R. Pinchaux, I. Forbeaux, J.-M. Debever, M. Sauvage-Simkin, and J.-M. Themlin, J. Appl. Phys. **92**, 2479 (2002).

14. C. Berger, Z. Song, X. Li, X. Wu, N. Brown, C. Naud, D. Mayou, T. Li, J. Hass, A. N. Marchenkov, E. H. Conrad, P. N. First, and W. A. de Heer, Science **312**, 1191 (2006).

15. G. M. Rutter, J. N. Crain, N. P. Guisinger, T. Li, P. N. First, and J. A. Stroscio, Science **317**, 219 (2007).

16. A. Nepal, G. P. Singh, B. N. Flanders, and C. M. Sorensen, Nanotechnology **24**, 245602 (2013).

17. G. Wang, J. Yang, J. Park, X. Gou, B. Wang, H. Liu, and J. Yao, J. Phys. Chem. C **112**, 8192 (2008).

18. Z.-H. Sheng, L. Shao, J.-J. Chen, W.-J. Bao, F.-B. Wang, and X.-H. Xia, ACS Nano **5**, 4350 (2011).

19. A. C. Ferrari, J. C. Meyer, V. Scardaci, C. Casiraghi, M. Lazzeri, F. Mauri, S. Piscanec, D. Jiang, K. S. Novoselov, S. Roth, and A. K. Geim, Phys. Rev. Lett. **97**, 187401 (2006).

20. D. C. Elias, R. R. Nair, T. M. G. Mohiuddin, S. V. Morozov, P. Blake, M. P. Halsall, A. C. Ferrari, D. W. Boukhvalov, M. I. Katsnelson, A. K. Geim, and K. S. Novoselov, Science **323**, 610 (2009).

21. F. Tuinstra and J. L. Koenig, J. Chem. Phys. **53**, 1126 (1970).

22. Z.-H. Sheng, L. Shao, J.-J. Chen, W.-J. Bao, F.-B. Wang, and X.-H. Xia, ACS Nano **5**, 4350 (2011).

23. M. Choi, I. S. Altman, Y.-J. Kim, P. V. Pikhitsa, S. Lee, G.-S. Park, T. Jeong, and J.-B. Yoo, Adv. Mater. **16**, 1721 (2004).

24. A. Sadezky, H. Muckenhuber, H. Grothe, R. Niessner, and U. Pöschl, Carbon **43**, 1731 (2005).

25. R. E. Franklin, Proc. R. Soc. Lond. Math. Phys. Eng. Sci. **209**, 196 (1951).

26. R. Dhaubhadel, C. S. Gerving, A. Chakrabarti, and C. M. Sorensen, Aerosol Sci. Technol. **41**, 804 (2007).

Chapter 5 - Highly Oxidized Graphene Nanosheets via the Oxidization of Detonation Carbon

Published in 2015 Applied Physics A, 120, 543–549

Abstract: A unique approach was developed to produce highly oxygenated graphene nanosheets (OGNs) by solution-based oxidation of the pristine graphene nanosheets (GNs) prepared via a controlled detonation of acetylene with oxygen. The produced OGNs are about 250 nm in size and are hydrophilic in nature. The C/O ratio was dramatically reduced from 49:1 in the pristine GNs to about 1:1 in OGNs, as determined by X-ray photoelectron spectroscopy. This C/O in OGNs is the least ever found in all oxidized graphitic materials that have been reported. Thus, the OGNs produced from the detonated GNs with such high degree of oxidation herein yields a novel and promising material for future applications.

5.1 Introduction

Already considered one of the most pivotal materials of this century, single layer graphene (SLG) is a one atom thick sheet of sp^2-bonded carbon atoms packed in honeycomb crystal lattice. It possesses superior physical properties like excellent electrical and thermal conductivity, optical transparency and mechanical strength [1–6]. New research is looking to employ these properties in areas such as nanoelectronics [7,8], sensors [9], nanocomposite [10,11], batteries [12], supercapacitors and hydrogen storage [13]. However, the complete exploitation of the proposed properties of SLG via promising applications has been a challenge since current large scale production methods are not simple and economical. The largest issue lies in the irreversible agglomeration and restacking of graphene sheets via π - π interactions and van der Waals forces, forming multilayer graphite if sheet separation is not maintained [14,15].

Processable graphene, chemically functionalized or surface modified graphene which can be well dispersed in solvents, is thought as a remedy to this problem. Chemically functionalized graphene can be easily processed by solvent assisted techniques like spin-coating, layer-by-layer assembly and filtration. A suitable chemical functional group attached on the graphene sheet can prevent the agglomeration of single layer graphene during its reduction in the solvent phase helping to maintain the inherent properties of SLG [16]. Graphite oxide prepared by oxidization of natural graphite has often been used as a starting material to prepare processable graphene. Graphite oxide contains highly oxygenated and hydrophilic layers which can be readily exfoliated in water to yield stable dispersions consisting mostly of single-layer sheets, i.e. graphene oxide [10,17–20]. This dispersion capability facilitates a very feasible setting to carry out solution phase techniques used to convert the graphene oxide back to graphene by chemical reduction [14,18].and processing graphene oxides into films and paper-like materials [18,19,21–23]. Therefore, the preparation of aqueous dispersion of graphene oxide is an important first step for the further applications of graphene by solution-phase surface manipulation.

Recently, we have demonstrated a unique method to produce the powder form of pristine graphene nanosheets (GNs) by a controlled detonation of acetylene (C_2H_2) with oxygen (O_2) [24]. This method is attractive due to the low cost and scalability. However, the GNs prepared by this new route are hydrophobic in nature and are not easy to be mixed with other chemicals and binders. This is a current challenge seen throughout the field of application of pristine GNs. Current research has shown that the application of pristine graphene in field effect transistors is not effective due to the absence of a band gap [25]. Hence, in order to further explore the landscape of the potential applications, functionalization of detonation produced pristine GNs is needed.

Here we report on the formation of highly oxidized graphene nanosheets (OGNs) by oxidizing the pristine GNs prepared via a controlled detonation of acetylene with oxygen using a unique wet chemical approach which changed the C/O ratio of GNs from 49:1 to 1:1 for OGNs. Further, the OGNs dispersed in water were stable for several months.

5.2 Experimental Procedures

5.2.1 Preparation of GNs

Powder GNs were prepared from the catalyst-free, controlled detonation of C_2H_2 gas in the presence of O_2 in a 16.6 liter cylindrical aluminum chamber. For this study, GNs were prepared from a detonation with the pre-detonation molar ratio of $O_2/C_2H_2 = 0.8$. For each detonation, the initial chamber pressure was 1 atmosphere. The gases had purities of 98.0 % for C_2H_2 and 99.0 % for O_2. The detonation of C_2H_2 with O_2 was carried out by a controlled power supply through a spark generator ignition system. The GN formed under a typical peak detonation condition of temperature ~4000 K and a peak pressure of 13.5 atmospheres. They were collected from the chamber approximately 10 minutes after detonation. For a detailed explanation of the experimental setup and mechanism of formation of GNs refer to [24].

5.2.2 Preparation of OGNs from GNs

The pristine GNs produced by the detonation technique described above was oxidized by using a method designed for an improved oxidization of graphite flakes as described in literature [26]. In this work, a typical 9/1 ratio of concentrated H_2SO_4/H_3PO_4 (270:30 mL) was added into a mixture 2g of GNs and 6g of $KMnO_4$ and stirred the mixture overnight at a temperature ~ 50° C. The mixture was then cooled to room temperature and then the suspension was diluted with water (300 mL) and 30% H_2O_2 (5 mL) in ice bath. The mixture then was centrifuged (7000 rpm for 30 minutes) and the supernatant was decanted away. The thick sludge at the bottom of the vial was diluted with water and again centrifuged. This intensive washing was repeated for about 7-10 times to remove any dissolved impurities. The sludge was then dried at room temperature and known as oxygenated graphene nanosheets (OGNs). During oxidation, no distinct color change was observed unlike the production of graphite oxides from the oxidation of graphite (which becomes bright yellow after diluting with H_2O_2). Instead, the suspension was dark black from start to end of the process. This might be because of the very small size (~250 nm) of the starting material, GNs.

5.2.3 Characterizations

X-ray diffraction was carried out using a Bruker D8 Advance X-ray diffractometer, Germany, with nickel filter Cu Kα radiation as the X-ray source to determine phase purity and degree of crystallization. Thermogravimetric analysis (TGA) of GNs and OGNs were carried out with a Perkin Elmer Pyris1 TGA (Norwalk, CT) to determine the decomposition characteristics of the samples. About 5 mg of each sample was placed in the pan and heated from 50°C to 600°C at a heating rate of 20°C/min under a nitrogen atmosphere. The layer and the size of the powder graphene samples were determined with a Philips CM-100 transmission electron microscope (TEM) with an accelerating voltage of 100 kV. For TEM measurement, the samples were prepared by inserting Cu grids in the GNs powder without using any solvent and by drying the Cu grids with OGNs dispersion casted on. Samples for atomic force microscopy (AFM) studies on samples of GNs and OGNs were prepared from their dispersions in ethanol at concentration 0.01 mg/ml for each. GNs and OGNs in ethanol at this concentration were dispersed and exfoliated by sonicating for 2 hours in an ultrasonic water bath (Branson 2510). The dispersions were then centrifuged for 15 minutes at 1000 rpm to let the heavier and un-exfoliated flakes settle. The supernatant was transferred into a petri dish. A silicon substrate was immersed into the supernatant and incubated for 2 minutes at room temperature. The substrates were then rinsed by immersing briefly into DI water. After rinsing, these substrates with expected thin layers of GNs and OGNs were dried using nitrogen flow and used for AFM imaging. Topographical images of GNs and OGNs were acquired in air, at room temperature, using contact mode AFM (Bruker USA, Innova). The AFM scanner was calibrated using a TGZ1 silicon grating (NT-MDT, USA). MLCT-E cantilevers (Bruker, USA) with nominal spring constants of 0.1 N/m were used with set point contact forces of 1 nN or less. The topographical images were flattened by subtracting the background and then re-plotted using a second order equation incorporated in the Gwyddion analysis software [27]. Diffuse reflectance FTIR spectra were recorded via a Cary 630 FTIR spectrophotometer, Agilent Technology, USA over a range 500-4000 cm^{-1}. X-ray photoelectron spectroscopy (XPS) spectra were collected on a Perkin-Elmer PHI 5400 spectrometer with an Al Kα X-ray source (1486.6 eV) operating at 240 W (12 kV and 20 mA). The spectrometer was calibrated using Au $4f_{7/2}$ at 84.0 eV and Cu $2p_{3/2}$ at 932.7 eV. The base pressure of the analysis chamber was below 10^{-9} mbar. Data analysis was performed using the CasaXPS software package. The room temperature Raman spectra of GNs were obtained on pellets with 10 mm diameter and 2 mm thick and on the dry patch of dispersion of OGNs casted on microscope slide with an iHR550 Raman spectrophotometer, Horiba Jobin Yvon with a HeNe laser (632.8 nm) as the excitation source.

5.3 Results and Discussions

Figure 5.1 shows the digital photographs of GNs powder synthesized from the controlled detonation of acetylene with oxygen, the same dispersed in water, and the OGNs dispersed in water with concentrations 1mg/ml, 0.1mg/ml and 0.01mg/ml.

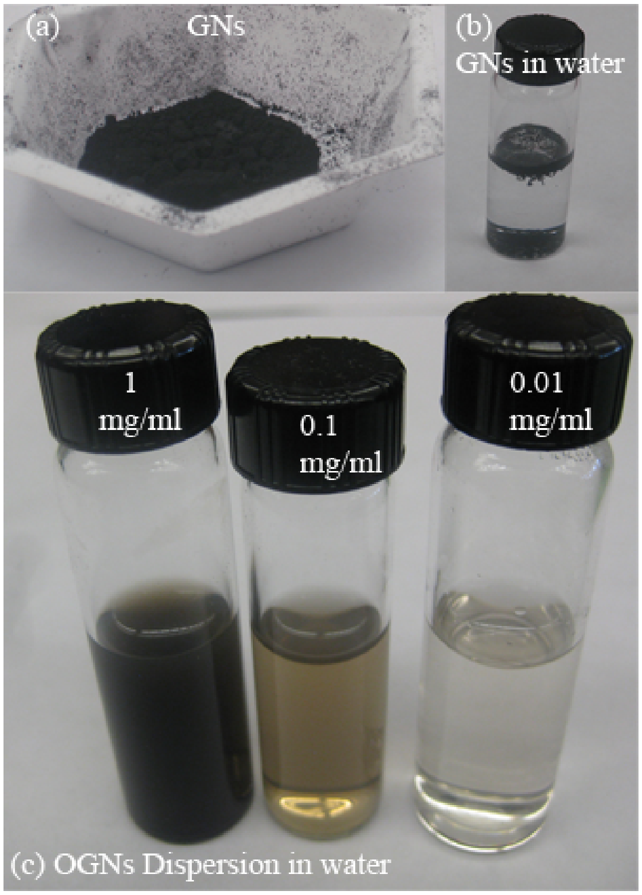

Figure 5.1 Images of (a) GNs powder, (b) GNs in water and (c) dispersion of OGNs in water with concentration as marked.

Detonation produced GNs (Fig. 5.1a) is a dark, fluffy and light powder. The photographs of dispersions were taken after eleven weeks from the day of a 0.5 hour sonication of the GNs and OGNs in water in order to see the stability of the samples' dispersion in water. It can be seen in Fig. 5.1(b) that the GNs are not dispersible in water and a small fraction of the GNs used floats on the surface of water whereas a larger fraction of GNs has settled to the bottom of the vial. OGNs, in contrast to GNs, are dispersible in water as seen in the photograph (Fig. 5.1c). The color change of the OGNs dispersion, dark black (1 mg/ml) to brown (0.1 mg/ml) to almost clear (0.01 mg/ml) is due to the suspended OGNs sheets with varying concentration. The dispersion shows that the hydrophobic GNs have been transformed to highly hydrophilic OGNs using this approach.

The size of the GNs and OGNs sheets are shown in Fig. 5.2.

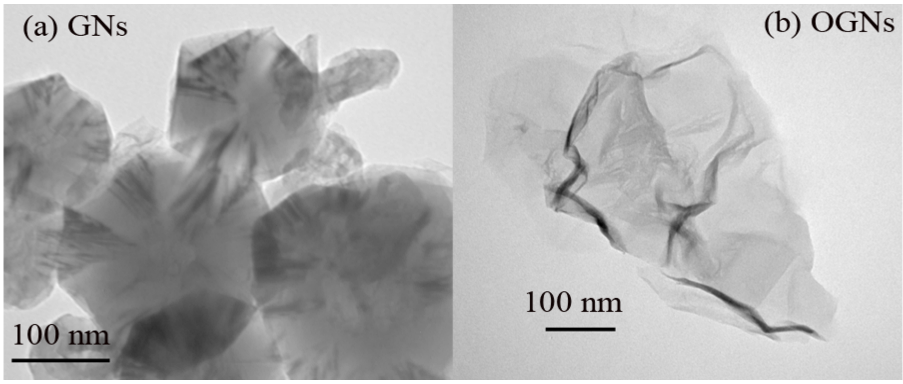

Figure 5.2 TEM images of (a) GNs prepared by detonation at O_2/C_2H_2 = 0.8 molar ratio [24] and (b) OGNs.

The GNs are stacked in two to three layers forming the aggregates of nearly circular sheets of size about 225-250 nm [24] as shown in Fig. 5.2(a). Interesting features were observed after the oxidization of these GNs. The stacked GNs transformed into transparent single layer OGNs with wrinkled ridges (Fig. 5.2b). The lateral size of the OGNs sheets do not seem to be uniform due to the folding at the edges. However, it can be concluded that the layer morphology of the GNs has been preserved even in OGNs sheets.

The XRD spectra of the GNs prepared by the detonation of C_2H_2 at O_2/C_2H_2 = 0.8 molar ratio and that of OGNs prepared from these GNs is shown in Fig. 5.3.

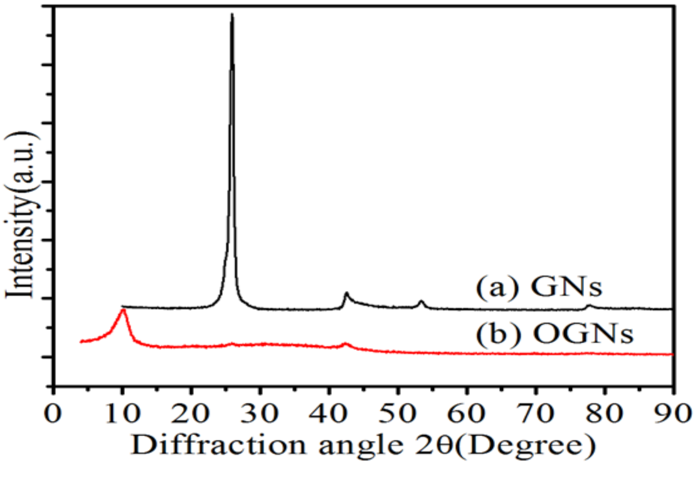

Figure 5.3 XRD patterns of (a) GNs prepared by detonation at O_2/C_2H_2 = 0.8 molar ratio [24] and (b) OGNs prepared from GNs

In Fig. 5.3 (a), the most intense and narrow peak on the spectrum of GNs is at 2θ ~ 26.05° corresponding to the (002) planes of stacked graphene layers in GNs [24] whereas that of OGNs is at 2θ ~ 10.15° as shown in Fig. 5.3(b). The nearly featureless region at 2θ ~ 26.05° on the spectrum of OGNs relative to that of GNs indicates that almost all GNs have been oxidized. These XRD spectra indicate that the interplanar spacing (d) of ~0.341 nm for GNs has been shifted to 0.879 nm for OGNs. This increment in the interplanar spacing in OGNs is due to the expansion of the layer planes caused by the accommodation of various oxygen species and water molecules while oxidizing GNs [16,23,28].

The size and thickness of the GNs and OGNs flakes were assessed from the AFM profile lines as well. The thinnest flake of GNs analyzed and measured was a bi-layer structure shown in Fig. 5.4(a).

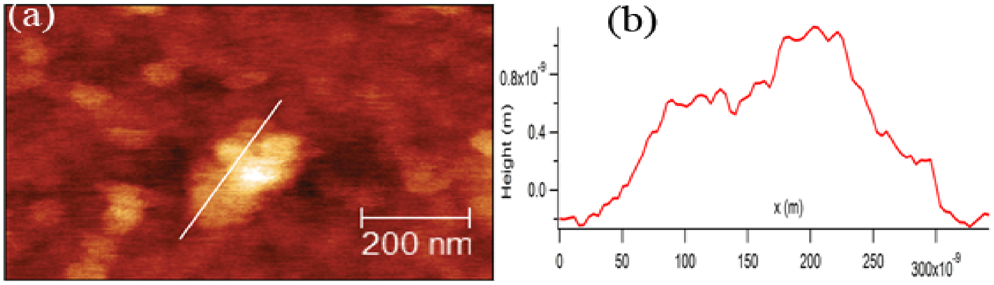

Figure 5.4 (a) AFM image of a 0.9 x 0.6 μm GNs flake (b) Profile line across the flake in panel (a). The measured approximate lateral length of the flake was 250 nm. Measured initial step was 0.9 nm high and the second step was at a height of 0. 36 nm from the first.

The first step in the profile line of GNs, Fig. 5.4(b), has a height of ~ 0.9 nm while the second step has a height of ~ 0.36 nm. This height of first step is approximately the same as the thicknesses (~1nm) of the single layers of substrate-supported graphene that were reported earlier [29,30]. An atom thick layer of graphene may exhibit a step height of ~1 nm when observed via AFM due to the following possible reasons: (i) attached molecules on the graphene surfaces; (ii) imperfect interface between the contacting surfaces; (iii) and different magnitudes of attractive forces between AFM probes and the silicon substrate [30,31]. The bi-layer GNs profiled in Fig. 5.4(a) has a double layer profile with the bottom layer protruding laterally. The surface of the top layer sits 0.36 nm above the bottom layer. This interlayer spacing agrees with the interplanar spacing of 0.341 nm that was measured in GNs samples via XRD. Furthermore, the lateral size of GNs measured from profile line (Fig. 5.4b) is about 250 nm; this value is consistent with the lateral sizes that we measured with TEM.

AFM image of OGNs flakes is shown in Fig. 5.5. The OGNs flakes have lateral size of about 240 nm measured along the profile 1 in Fig. 5.5(a) as seen in the plot, Fig 5.5(b). This size of OGNs is very close to the size predicted by TEM image of the same.

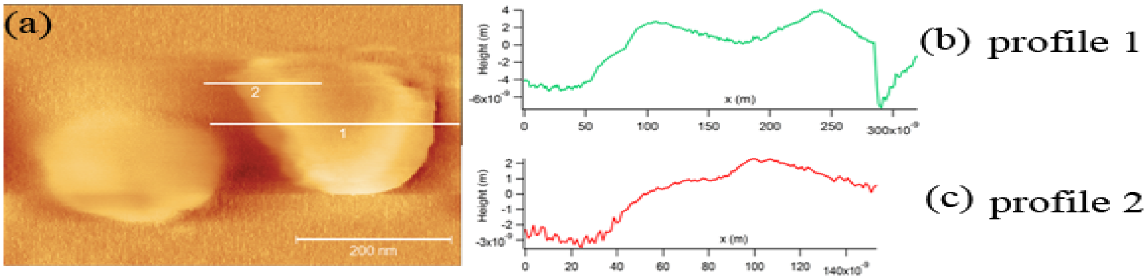

Figure 5.5 (a) AFM image of 0.6x0.4 µm OGNs flake (b) Profile line across the flake along line 1 in panel (a), and (c) Profile line across the edge of the flake along line 2 in panel (a). The approximated lateral length of the flake was around 240 nm, an initial step height was ~ 3.7 nm, the measured height difference between the initial step (short plateau) and second plateau was ~ 0.8 nm.

The initial step height of 3.7 nm in the profile line of OGNs (Fig. 5.5 b and c) is more than 1 nm, that for single layer GNs. This might be because of OGNs edge folded downward on the substrate. It might also be an un-exfoliated, multilayered clump of OGNs.

The profile line in Fig.5.5(b) shows humps and plateaus. Highly oxidized (C/O ~1/1, see Fig. 5.9) OGNs layers are not expected to remain flat and smooth. Rather, they are likely to exhibit significant folding because extent of folding increases with the degree of oxidation [28]. The humps on the profile line represent these intrinsic ripples and folds along OGNs surface. However, a careful look at profile 2 in Fig 5.5(a) (and plotted in Fig. 5.5c) shows very short plateaus. The spacing between neighboring plateaus is ~0.8 nm. This value is close to the interplanar spacing of ~ 0.879 nm obtained from the XRD of OGNs. In conclusion, the layer morphology, size and interplanar spacing of GNs and OGNs were also studied with AFM and the observed features are in reasonable agreement with the lateral sizes and interplanar spacing that have been observed independently via TEM and XRD.

The decomposition characteristics of GNs and OGNs under heat were evaluated by TGA as depicted in Fig 5.6.

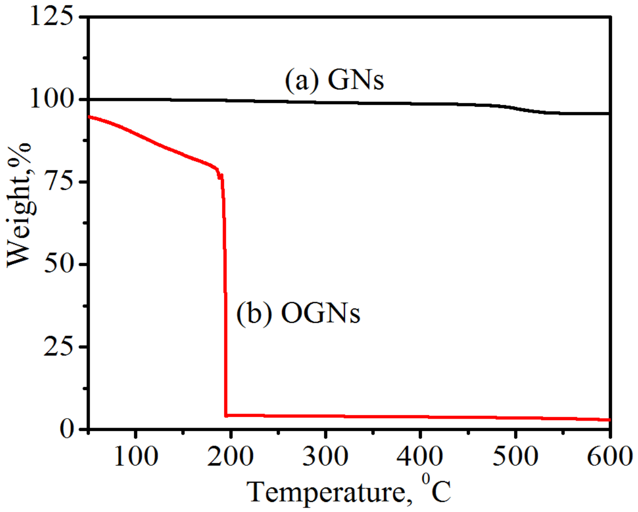

Figure 5.6 TGA of (a) GNs and (b) OGNs

The GNs were observed to be thermally stable with a loss of only ~ 4% weight while heated up to 600° C as shown in Fig. 5.6(a). However, OGNs (Fig. 5.6b) were thermally unstable with mass lost mainly in two steps: a small fraction, about 25%, of its weight lost continuously while heating up to 190° C, and a significant fraction, about 95%, of its weight lost rapidly at 197° C. The decreased thermal stability of OGNs is due to the labile oxygen functional groups that yield CO, CO_2 and steam under pyrolysis [20,32]. Thus, the TGA analysis shows that the GNs were oxidized, and this is consistent with the inference drawn from XRD of GNs and OGNs.

The oxidation of the GNs was further evaluated by Raman Spectroscopy. Figure 5.7 shows the Raman spectra of GNs and OGNs.

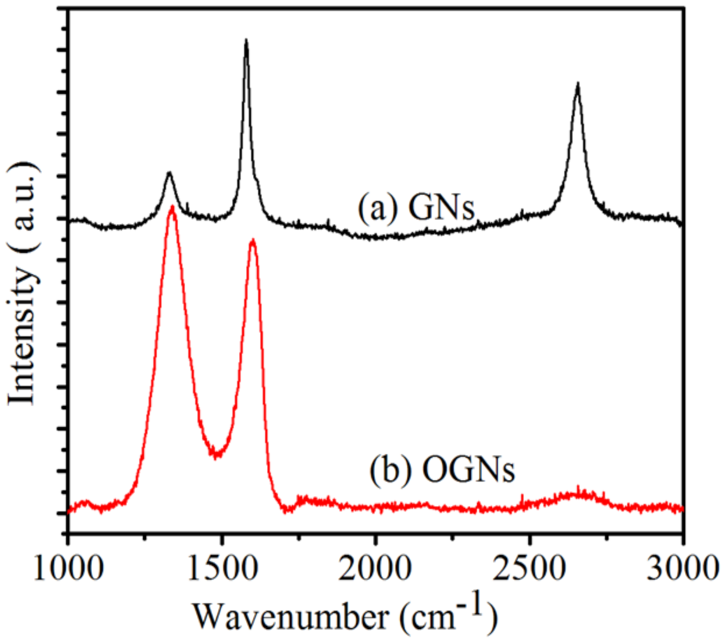

Figure 5.7 Raman spectra of (a) GNs prepared by detonation at O_2/C_2H_2 = 0.8 molar ratio [24] and (b) OGNs.

The three prominent peaks at 1328 cm^{-1}, 1580 cm^{-1} and 2650 cm^{-1} on the spectrum of GNs (Fig. 5.7a) correspond to D-, G- and 2D-bands, respectively. These observed bands are in good agreement with the earlier report [24]. The D-band evolves due to the defect or partially disordered structure of the sp^2 domains in GNs whereas the G-band is due to the optical E_{2g} phonon at the Brillouin zone center of all sp^2 hybridized carbons in GNs [24,33]. The 2D-band is the second order of the D-band, sometimes referred to as an overtone of the D-band. Since the 2D- band is the sum of two phonons with opposite momentum, it can be present even if the sample is defects-free [34,35].

The oxidation leads to shifts in the band positions of the D-band and G-band of OGNs (Fig 5.7b) by 8 and 20 cm^{-1}, respectively, towards the higher frequency relative to that of GNs. The ratio of the intensity of D-band to intensity of G-band ($I_D/I_G \sim 1.13$) in OGNs is enhanced four times than that in the GNs ($I_D/I_G \sim 0.28$). Furthermore, the broadening in FWHM of G-band in OGNs (~ 90 cm^{-1}) is increased by 1.9 times from that of GNs (~ 48 cm^{-1}). Moreover, a huge reduction in the I_{2D}/ I_G (~ 0.07) compared to that of GNs ($I_{2D}/ I_G \sim 0.77$) is observed. The blue shifted and broadened G-band, more intense D-band and less intense 2D- band in the spectra of OGNs are all consistent with the Raman spectra of graphite oxide reported in past [36]. Such behavior is due to the disorder induced reduction in the average size of sp^2 domains by the formation of hydroxyl or epoxies groups with carbon during oxidation of GNs [20,37,38] as confirmed by the Drifts-FTIR in Fig. 5.8.

Figure 5.8 displays the Drifts-FTIR spectra of GNs and OGNs.

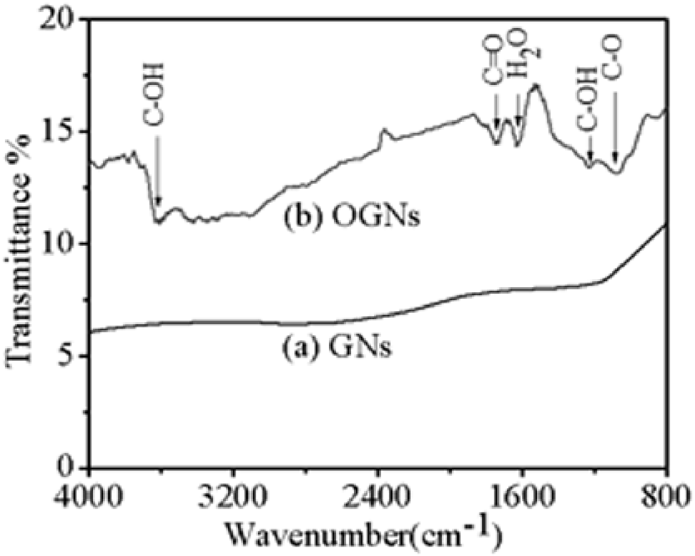

Figure 5.8 FTIR of (a) GNs prepared by detonation at O_2/C_2H_2 = 0.8 molar ratio [24] and (b) OGNs

The spectrum of GNs (Fig. 5.8a) is almost featureless and suggests that no functional groups are attached on the surface of GNs and hence they are pristine in nature [24]. However, the Drifts-FTIR spectrum of OGNs (Fig. 5.8b) has the adsorption bands centered at wavenumbers that resemble those mentioned in the previous works [39–43] with the band at ~ 1073 cm^{-1} attributed to C-O epoxy stretching vibrations, ~ 1224 cm^{-1} due to C-OH stretching vibrations, ~ 1623 cm^{-1} from deformation vibration of water molecules, ~ 1734 cm^{-1} from C=O carbonyl stretching and ~3613 cm^{-1} from stretching vibration of hydroxyl groups. Thus the GNs have been oxidized extensively, and the surface has been decorated with aforementioned carbonyl, epoxy and hydroxyl functional groups.

More precisely the surface functional groups present in GNs and OGNs were further explored by x-ray photoelectron spectroscopy (XPS) and the spectra observed are presented in Fig. 5.9.

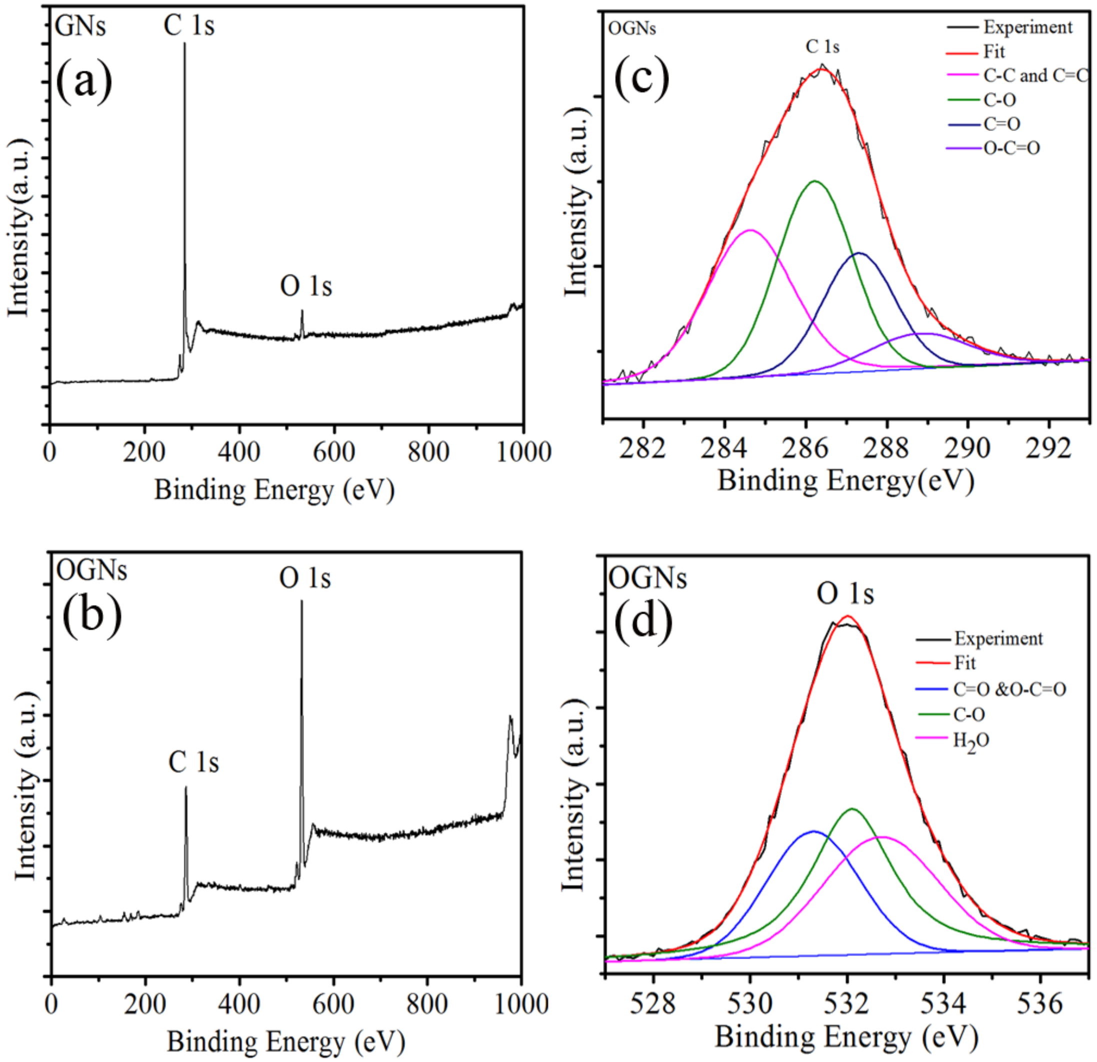

Figure 5.9 XPS spectra of (a) GNs prepared by detonation at O_2/C_2H_2 = 0.8 molar ratio, survey [24] (b) OGNs, survey (c) C 1s detail of OGNs and (d) O 1s detail of OGNs.

Two peaks corresponding to the O 1s and C 1s are observed in the survey spectrum of GNs shown in Fig. 5.9(a). The ratio of the carbon to oxygen is estimated to be C/O ≈ 49/1, indicating that GNs are very pure. The small peak of O 1s is probably due to the moisture adsorbed in the system [24]. The survey spectrum of OGNs in Fig. 5.9(b) shows a more prominent and intense O 1s peak relative to that in the survey spectrum of GNs. This indicates that an extensive oxidation of GNs has taken place to yield OGNs. The carbon to oxygen (C/O) ratio in OGNs is ≈1/1. The C 1s peak of OGNs was expanded and deconvoluted (Fig. 5.9c) in order to analyze the other forms of the carbon and oxygen groups. The deconvolution shows the four components of carbon and oxygen groups at around 284.8 eV, 286.4 eV, 287.5 eV and 288.9 eV which correspond to C=C or C-C, C-O, C=O and O-C=O groups, respectively, as mentioned in past works [6,30,44–46]. Out of the total area under C 1s peak, 34% belongs to unoxidized carbon (C=C or C-C), 36% belongs to carbon attached as epoxy or hydroxyl functional groups (C-O), 22% belongs to carbonyl (C=O) and the rest of 8% is the share of carbon attached to carboxylic functional group (O-C=O). The C/O ratio depends on the experimental conditions such as amount of oxidizers, time of reactions and size and morphology of the graphitic material to be oxidized. The C/O ratios that have been achieved so far in graphite oxide sheets after oxidation of graphite using conventional techniques is 2/1 to 4/1 [44,47]. These C/O ratios are higher than the C/O ≈ 1/1for OGNs prepared here from detonated GNs. Hence, it is worthwhile to highlight that the detonation produced GNs are unique in the sense that they can be oxidized to a product with the highest level of oxygenation compared to oxides of any other graphitic materials.

Now the question comes across why the detonation produced GNs gets oxidized so heavily. The topic of chemistry and heterogeneity of graphene oxide is still debated [48]. However, what is exciting about graphene is it can be functionalized on the both faces of a layer, at the edges and at the defects [49]. The surfaces of graphene, in contrast to less reactive graphite surfaces, are exceptionally reactive [50,51]. Moreover, the carbon atoms at the graphene edges are more reactive than those at the bulk surface faces [49]. The vacancies, adatoms and point and linear imperfections on the surface enhance the crystal defects in the graphene layers. These defects on the graphene surface are also considered as active sites for chemical reactions [52].

Graphite flakes, the conventional starting material to produce graphene oxide, are a few to several hundred micrometers in size. However, our GNs, the starting material used in this work, are significantly smaller (~ 250 nm) than the graphite flakes. Moreover, the specific surface area of GNs (~25 m^2/g) used here is at least 3 times more than that of natural graphite (< 8 m^2/g). Also, the Raman Spectrum of detonation produced GNs, Fig. 5.7 (a), has shown that the GNs have a considerable amount of defects. Thus, detonation produced GNs have more reactive sites contributed from the boundaries, surfaces and the defects relative to the natural graphite flakes and hence it will be oxidized the most. The type of functional groups and their share for the oxygen content in OGNs have been determined by deconvoluting its XPS O 1s peak as shown in figure 7 (d). The O 1s peak of OGNs shows the three components at around 531.7

eV, 532.5 eV and 533.1 eV which correspond to C=O & O-C=O, C-O and water (H_2O), respectively, as mentioned in past works [53–55]. The components corresponding to C=O & O-C=O, C-O and H_2O occupy about 30%, 40% and 30% area under O 1s peak, respectively. Despite significant vagueness regarding the exact location of a particular functional group, it has been reported in past that most of the carbonyl and carboxyl (C=O & O-C=O) functional groups usually exist at the edges and most of the hydroxyl and epoxy (C-O) groups lie above and below a graphene oxide layer [32,54,56]. Thus, we speculate here that out of all O- moieties in OGNs about 30% lie on the edges, 40% lie on the bulk surface of OGNs layer and the rest of 30% is due to intercalated or chemisorbed water molecules. The oxides attached in this fashion, along with the carbon-carbon chain (C=C or C-C in Fig. 5.9c) as backbone, still restore the layer morphology of OGNs as shown in TEM image (Fig. 2b).

5.4 Conclusion

The graphene nanosheets (GNs) produced from the hydrocarbon detonation route have been oxidized. The observed C/O ≈1:1 for the oxidized graphene nanosheets (OGNs) is the highest ever level of oxidation of graphitic materials. The OGNs sheets are highly dispersible in water and hence capable of further processing in order to use them for future applications.

5.5 References

1. K. S. Novoselov, A. K. Geim, S. V. Morozov, D. Jiang, Y. Zhang, S. V. Dubonos, I. V. Grigorieva, and A. A. Firsov, Science 306, 666 (2004).

2. G. Wang, J. Yang, J. Park, X. Gou, B. Wang, H. Liu, and J. Yao, J. Phys. Chem. C 112, 8192 (2008).

3. X. Li, X. Wang, L. Zhang, S. Lee, and H. Dai, Science 319, 1229 (2008).

4. P. Blake, P. D. Brimicombe, R. R. Nair, T. J. Booth, D. Jiang, F. Schedin, L. A. Ponomarenko, S. V. Morozov, H. F. Gleeson, E. W. Hill, A. K. Geim, and K. S. Novoselov, Nano Lett. 8, 1704 (2008).

5. G. Wang, X. Shen, B. Wang, J. Yao, and J. Park, Carbon 47, 1359 (2009).

6. D. R. Dreyer, S. Park, C. W. Bielawski, and R. S. Ruoff, Chem. Soc. Rev. 39, 228 (2009).

7. Y.-M. Lin, K. A. Jenkins, A. Valdes-Garcia, J. P. Small, D. B. Farmer, and P. Avouris, Nano Lett. 9, 422 (2009).

8. F. Schedin, A. K. Geim, S. V. Morozov, E. W. Hill, P. Blake, M. I. Katsnelson, and K. S. Novoselov, Nat. Mater. 6, 652 (2007).

9. N. Mohanty and V. Berry, Nano Lett. 8, 4469 (2008).

10. S. Stankovich, D. A. Dikin, G. H. B. Dommett, K. M. Kohlhaas, E. J. Zimney, E. A. Stach, R. D. Piner, S. T. Nguyen, and R. S. Ruoff, Nature 442, 282 (2006).

11. S. Watcharotone, D. A. Dikin, S. Stankovich, R. Piner, I. Jung, G. H. B. Dommett, G. Evmenenko, S.-E. Wu, S.-F. Chen, C.-P. Liu, S. T. Nguyen, and R. S. Ruoff, Nano Lett. 7, 1888 (2007).

12. T. Takamura, K. Endo, L. Fu, Y. Wu, K. J. Lee, and T. Matsumoto, Electrochimica Acta 53, 1055 (2007).

13. A. K. Geim and K. S. Novoselov, Nat. Mater. 6, 183 (2007).

14. D. Li, M. B. Müller, S. Gilje, R. B. Kaner, and G. G. Wallace, Nat. Nanotechnol. 3, 101 (2008).

15. C. Shan, H. Yang, D. Han, Q. Zhang, A. Ivaska, and L. Niu, Langmuir 25, 12030 (2009).

16. T. Kuila, S. Bose, A. K. Mishra, P. Khanra, N. H. Kim, and J. H. Lee, Prog. Mater. Sci. 57, 1061 (2012).

17. C. Gómez-Navarro, R. T. Weitz, A. M. Bittner, M. Scolari, A. Mews, M. Burghard, and K. Kern, Nano Lett. 7, 3499 (2007).

18. Y. Xu, H. Bai, G. Lu, C. Li, and G. Shi, J. Am. Chem. Soc. 130, 5856 (2008).

19. H. A. Becerril, J. Mao, Z. Liu, R. M. Stoltenberg, Z. Bao, and Y. Chen, ACS Nano 2, 463 (2008).

20. S. Stankovich, D. A. Dikin, R. D. Piner, K. A. Kohlhaas, A. Kleinhammes, Y. Jia, Y. Wu, S. T. Nguyen, and R. S. Ruoff, Carbon 45, 1558 (2007).

21. G. Eda and M. Chhowalla, Adv. Mater. 22, 2392 (2010).

22. X. Wang, L. Zhi, and K. Müllen, Nano Lett. 8, 323 (2008).

23. D. A. Dikin, S. Stankovich, E. J. Zimney, R. D. Piner, G. H. B. Dommett, G. Evmenenko, S. T. Nguyen, and R. S. Ruoff, Nature 448, 457 (2007).

24. A. Nepal, G. P. Singh, B. N. Flanders, and C. M. Sorensen, Nanotechnology 24, 245602 (2013).

25. G. Xie, Z. Wang, Z. Cui, and Y. Shi, Carbon 43, 3181 (2005).

26. D. C. Marcano, D. V. Kosynkin, J. M. Berlin, A. Sinitskii, Z. Sun, A. Slesarev, L. B. Alemany, W. Lu, and J. M. Tour, ACS Nano 4, 4806 (2010).

27. D. Nečas and P. Klapetek, Cent. Eur. J. Phys. 10, 181 (2012).

28. T. Szabó, O. Berkesi, P. Forgó, K. Josepovits, Y. Sanakis, D. Petridis, and I. Dékány, Chem. Mater. 18, 2740 (2006).

29. S. Wang, Y. Zhang, N. Abidi, and L. Cabrales, Langmuir 25, 11078 (2009).

30. J. I. Paredes, S. Villar-Rodil, A. Martínez-Alonso, and J. M. D. Tascón, Langmuir 24, 10560 (2008).

31. X. Li, X. Wang, L. Zhang, S. Lee, and H. Dai, Science 319, 1229 (2008).

32. A. Lerf, H. He, M. Forster, and J. Klinowski, J. Phys. Chem. B 102, 4477 (1998).

33. F. Tuinstra and J. L. Koenig, J. Chem. Phys. 53, 1126 (1970).

34. A. C. Ferrari, J. C. Meyer, V. Scardaci, C. Casiraghi, M. Lazzeri, F. Mauri, S. Piscanec, D. Jiang, K. S. Novoselov, S. Roth, and A. K. Geim, Phys. Rev. Lett. 97, 187401 (2006).

35. D. C. Elias, R. R. Nair, T. M. G. Mohiuddin, S. V. Morozov, P. Blake, M. P. Halsall, A. C. Ferrari, D. W. Boukhvalov, M. I. Katsnelson, A. K. Geim, and K. S. Novoselov, Science 323, 610 (2009).

36. K. N. Kudin, B. Ozbas, H. C. Schniepp, R. K. Prud'homme, I. A. Aksay, and R. Car, Nano Lett. 8, 36 (2008).

37. T. C. Chieu, M. S. Dresselhaus, and M. Endo, Phys. Rev. B 26, 5867 (1982).

38. A. A. Alhwaige, T. Agag, H. Ishida, and S. Qutubuddin, RSC Adv. 3, 16011 (2013).

39. S. Stankovich, R. D. Piner, S. T. Nguyen, and R. S. Ruoff, Carbon 44, 3342 (2006).

40. O. B. Tamás Szabó, Carbon 43, 3186 (2005).

41. G. I. Titelman, V. Gelman, S. Bron, R. L. Khalfin, Y. Cohen, and H. Bianco-Peled, Carbon 43, 641 (2005).

42. H. Zhang, D. Hines, and D. L. Akins, Dalton Trans. 43, 2670 (2014).

43. G. P. Singh, K. M. Shrestha, A. Nepal, K. J. Klabunde, and C. M. Sorensen, Nanotechnology 25, 265701 (2014).

44. G. Eda, G. Fanchini, and M. Chhowalla, Nat. Nanotechnol. 3, 270 (2008).

45. A. Kolmakov, D. A. Dikin, L. J. Cote, J. Huang, M. K. Abyaneh, M. Amati, L. Gregoratti, S. Günther, and M. Kiskinova, Nat. Nanotechnol. 6, 651 (2011).

46. J. Shang, L. Ma, J. Li, W. Ai, T. Yu, and G. G. Gurzadyan, Sci. Rep. 2, 792 (2012).

47. W. S. Hummers and R. E. Offeman, J. Am. Chem. Soc. 80, 1339 (1958).

48. V. Georgakilas, M. Otyepka, A. B. Bourlinos, V. Chandra, N. Kim, K. C. Kemp, P. Hobza, R. Zboril, and K. S. Kim, Chem. Rev. 112, 6156 (2012).

49. M. Quintana, J. I. Tapia, and M. Prato, Beilstein J. Nanotechnol. 5, 2328 (2014).

50. R. Sharma, J. H. Baik, C. J. Perera, and M. S. Strano, Nano Lett. 10, 398 (2010).

51. M. Quintana, K. Spyrou, M. Grzelczak, W. R. Browne, P. Rudolf, and M. Prato, ACS Nano 4, 3527 (2010).

52. F. Banhart, J. Kotakoski, and A. V. Krasheninnikov, ACS Nano 5, 26 (2011).

53. O. Akhavan, Carbon 48, 509 (2010).

54. A. Ganguly, S. Sharma, P. Papakonstantinou, and J. Hamilton, J. Phys. Chem. C 115, 17009 (2011).

55. K. Haubner, J. Murawski, P. Olk, L. M. Eng, C. Ziegler, B. Adolphi, and E. Jaehne, ChemPhysChem 11, 2131 (2010).

56. D. Hadži and A. Novak, Trans. Faraday Soc. 51, 1614 (1955).

Chapter 6 - Summary and Future Directions

The summary of hydrocarbon detonation experiments to produce graphene nanosheets and their oxides will be discussed in this chapter. Also, some of viable experiments that can be carried out to keep this project going on are proposed.

6.1 Summary of the research

We produced pristine graphene nanosheets (GNs) by detonating C_2H_2 with oxygen in a closed chamber [1]. A two-color pyrometer and a pressure probe were installed on the chamber to measure the detonation temperature and pressure. The average peak detonation temperature and pressure were about 4000 K and 13.5 atmospheres respectively for detonations at O2/C2H2= 0.4 ,0.5, 0.6, 0.7, and 0.8. We propose that this high *in situ* temperature during the detonation leads to a carbon vapor that forms graphene when it quickly cools after the detonation. Our process has several advantages such as simplicity, high productivity (~70% yield), economic viability, and short synthesis time (minute). This method does not need any external source of heat for high temperature; it is a catalyst-free method and does not generate any toxic by-products [1].

Detonation of C_2H_4 yields GNs as well. However, C_3H_8 produces amorphous carbon soot and CH_4 give no solid carbon products while detonated with O_2, We claim that the aliphatic hydrocarbons with $C/H \geq 0.5$ may produce graphene whereas hydrocarbons with $C/H \leq 0.375$ will produce either normal carbon soot or no solid carbon while detonated with oxygen.

In related work, we used improved Hummers method to oxidize detonation produced GNs to create highly oxidized graphene nanosheets (OGNs) with C: O ~ 1:1. This carbon to oxygen ratio in OGNs is the lowest ever ; the previous best was C:O~ 2:1 [2]. The dispersion of the OGNs so produced into water remains stable for several months. Thus the combination of the controlled detonation synthesis with the oxidation yields a promising material for applications that need processable graphene.

6.2 Future plans/interests

Our immediate future interest is to seek the answers to the following questions: (a) can we improve the quality and yield of detonation produced materials? (b) what are the applications of GNs? The following two schemes can be thought of as the answers to these questions.

6.2.1 Scaling up the detonation method for higher quality and yield of the product

Detonation produced GNs are basically in a hybrid system of single, few and multilayer graphene. If we will be able to outlet the GNs into a spacious closed container, almost simultaneously with their production, Fig. 6.1, we might avoid the quick aggregation and stacking of GNs into the detonation chamber. The GNs collected outside the detonation chamber might, thus, mostly be single to few layer ones with increased specific surface area (SSA). These GNs with higher SSA are better for many applications. We can then design and modify the chamber into an auto 'fill-detonate–clean" system. If many automated detonations are performed in multiple chambers, we will materialize our dream of a "graphene mill" for the bulk production of the graphene.

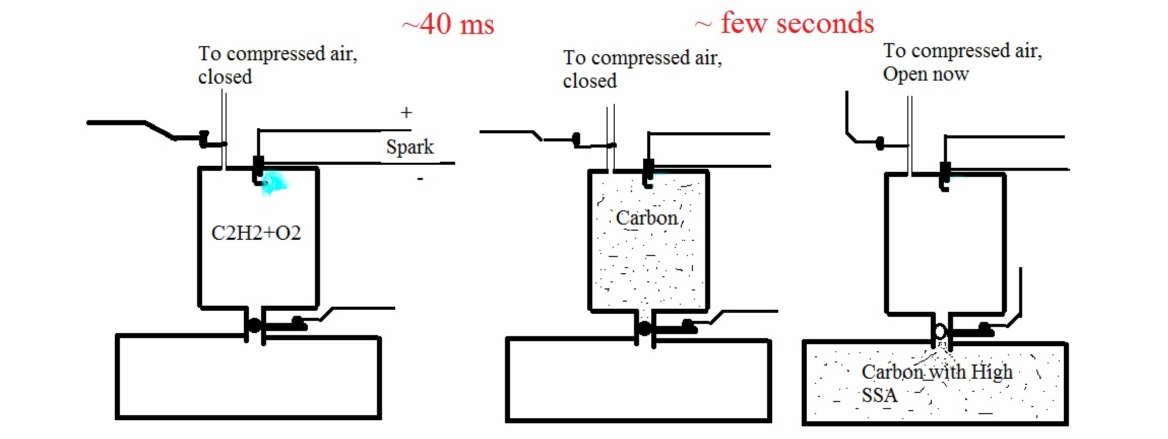

Figure 6.1 Scheme for the production of GNs with high SSA

Also, exploring the idea of spraying nanoparticles (metal, nonmetal), via a nebulizer, very immediately after a detonation into the graphene aerosol is good avenue to follow. This may produce some hetero-structure on the graphene surface. For example, we may prepare capsules of Si wrapped into the crumpled GNs that had already been applied in Li ion batteries as mentioned in section 6.2.2.

6.2.2 Exploring the applications of detonation products

The crumpled GNs and OGNs that we produce from our unique and novel method are to be intensively experimented to determine their best applications. To begin with, we will go with exploring the application in energy devices: graphene based ultracapacitors and Li ion batteries. Crumpled graphene, produced from other techniques, has already been proved good for scalability of graphene based ultracapacitors[3] and the crumpled graphene-encapsulated Si nanoparticles are being used for the improved efficiency of Li ion batteries [4]. Electronics and optoelectronics might be the other areas of application of the detonation produced GNs.

6.3 References

1. A. Nepal, G. P. Singh, B. N. Flanders, and C. M. Sorensen, Nanotechnology **24**, 245602 (2013).
2. A. Nepal, G. Chiu, J. Xie, G. P. Singh, N. Ploscariu, S. Klankowski, T. Sung, J. Li, B. N. Flanders, K. L. Hohn, and C. M. Sorensen, Appl. Phys. A **120**, 543 (2015).
3. J. Luo, H. D. Jang, and J. Huang, ACS Nano **7**, 1464 (2013).
4. J. Luo, X. Zhao, J. Wu, H. D. Jang, H. H. Kung, and J. Huang, J. Phys. Chem. Lett. **3**, 1824 (2012).